

POLITECNICO DI MILANO

School of Industrial and Information Engineering

Master of Science in Materials Engineering and Nanotechnology

Master of Science in Mechanical Engineering



**Active 3D-Printed Mechanisms for
Antennas in CubeSats**

Internal supervisor: Prof. Stefano Mariani

Host Supervisor: Prof. Kristina Shea

Master Thesis of:

Gaia Alberio

Mat. 858824

Academic Year 2017-2018

This thesis project was developed at
Eidgenössische Technische Hochschule Zürich
(Zurich, Switzerland)

Contents

1	Introduction	1
2	Theoretical background	3
2.1	Antennas in CubeSats	5
2.1.1	Monopole and dipole antenna	5
2.1.2	Microstrip antenna	6
2.1.3	Conical log-spiral antenna	7
2.1.4	Parabolic reflector	9
2.1.5	Single and multiple helical antenna	10
2.2	Materials for space antennas	14
2.2.1	Metals and Alloys	14
2.2.2	Polymers and composites	16
2.3	3D Printing	20
2.4	4D Printing	24
2.4.1	Printers and preliminary works	24
3	Materials' study	27
3.1	Space requirements	28
3.1.1	Vacuum	28
3.1.2	Atomic Oxygen	29
3.1.3	Ultraviolet Radiation	30
3.1.4	Thermal effects	31
3.1.5	Debris	33
3.1.6	Summary and discussion	34

3.2	Material comparison based on CES EduPack database	35
3.2.1	Polymers	37
3.2.2	Metals	39
3.3	Final choice	44
4	Antenna selection	47
4.1	Introduction	47
4.2	Antenna characteristics	48
4.2.1	Key specification: radiation pattern, coverage and gain	48
4.2.2	Antenna design for spacecrafts: polarization and directivity	51
4.3	Antenna for ETH CubeSat	52
4.3.1	Requirements and restrictions	52
4.3.2	Overview of possible designs	54
5	Antenna design and manufacturing	61
5.1	Modeling of helix antenna design	61
5.1.1	Equations	62
5.1.2	Dimensional analysis	62
5.2	Cube Modular Structure	67
5.2.1	First prototype - C1	69
5.2.2	Second prototype - C2	69
5.2.3	Third prototype - C3	71
5.3	Double Spring System	74
5.3.1	First prototype - H1	75
5.3.2	Second prototype - H2	78
5.3.3	Third prototype - H3	80
6	Testing and results	85
6.1	Programming and deployment testing	86
6.1.1	Determination of the folding angle	86
6.1.2	Folding and unfolding of the structure	87
6.2	Mechanical vibration testing	94

6.2.1	Comsol models	94
6.2.2	Experimental vibration test	105
6.2.3	Result comparison	113
6.3	Final remarks	114
7	Conclusions and outlook	115
7.1	Conclusions	115
7.2	Outlook	119

List of Figures

2.1	Dipole antenna [12]	5
2.2	Deployed antennas in PolySat satellite [13]	6
2.3	Top view of the microstrip antenna [14]	7
2.4	Antennas of Mars 3 [2]	8
2.5	CLSA z-deployment [18]	9
2.6	Folding mechanism: Miura-Ori [19]	9
2.7	6.5 m AstroMesh [21]	10
2.8	Gain pattern of a helical antenna in axial mode [2]	11
2.9	Undeployed and deployed QHE [19]	12
2.10	Simulated deployment [22]	12
2.11	Deployed antenna and unfolding sequence [23]	13
2.12	Microfluidics-based antenna [24]	13
2.13	SMA behaviour scheme [25]	15
2.14	55-Nitinol disk-on-rod antenna [26]	15
2.15	HCT quadrifilar helical antenna [27]	16
2.16	MWCNT acidic functionalization [28]	17
2.17	Molecular mechanism of the induced shape memory effect [29]	18
2.18	Thermodynamics of a SMP system [31]	19
2.19	Deployment mechanism of a truss structure [32]	20
2.20	Basics of FDM Printing [34]	21
2.21	Part with overhangs [35]	22
2.22	uPrint SE Plus 3D Printer by Stratasys [36]	22
2.23	Connex3 Object500 3D Printer by Stratasys [37]	23
2.24	FDM-Printed active parts [38]	25

3.1	Outgassing in vacuum - Test equipment [39]	29
3.2	Shuttle glow phenomenon [41]	29
3.3	Organic bonds wavelength [6]	31
3.4	Vacuum system block diagram [5]	32
3.5	Coatings' failure related to thermal cycling and AO erosion [4]	33
3.6	Crater created by a micrometeoroid [4]	34
3.7	Ashby chart - Young's modulus vs. Density	36
3.8	Polymers' T_{glass} vs. Young's modulus	37
3.9	Polymers' Resistance to solar radiation vs. Young's Modulus	38
3.10	Polymers' Maximum service temperature	38
3.11	Metals' Young's modulus vs. Density	39
3.12	Metals' Maximum service temperature	40
3.13	Metals' Radiation resistance vs. Density	40
3.14	Antenna requirements	44
4.1	Hertz first radio [46]	47
4.2	Radiation pattern [2]	49
4.3	Half-Power Beam Width (HPBW) [47]	50
4.4	Polarization of a wave [47]	51
4.5	CubeSat specifications [1]	53
5.1	Numerical evaluation of Equation 5.1	63
5.2	Numerical evaluation of design parameters for several frequencies	64
5.3	Representation of the pitch angle of the helix	65
5.4	Conductor coils	67
5.5	Deployment mechanics of a modular structure [51]	68
5.6	Rendering of the preliminary modular structures	68
5.7	Displacement of prototype C1	69
5.8	Geometry of a tape springs [52]	70
5.9	Rendering of prototype C2	71
5.10	Folded tape spring	72
5.11	Rendering of prototype C3	73

5.12	Prototype C3	73
5.13	Rendering of the preliminary single helix concept	74
5.14	Rendering of the preliminary double helix concept	75
5.15	Rendering of prototype H1	76
5.16	Base of prototype H1 as printed	77
5.17	Prototype H1	78
5.18	Rendering of prototype H2	79
5.19	Prototype H2	80
5.20	Rendering of Agilus and VeroWhite+ parts	81
5.21	Rendering of the assembled base	82
5.22	Rendering of prototype H3	82
6.1	Folding angle calculation	86
6.2	H3 - Counterclockwise prototype	87
6.3	H3 - Counterclockwise prototype inside warm bath	88
6.4	H3 - Counterclockwise prototype in the fixed height state	89
6.5	H3 - Counterclockwise prototype height comparison	89
6.6	H3 - Clockwise prototype inside warm bath	90
6.7	H3 - Clockwise prototype in fixed height state	90
6.8	H3 - Clockwise prototype comparison	91
6.9	H3 - Assembled prototype inside the water bath	92
6.10	H3 - Meta-stable prototype top view	92
6.11	H3 - Assembled prototype comparison	93
6.12	C3 - Mesh optimization	95
6.13	C3 - First mode - $f_1 = 187.94$	96
6.14	C3 - Second mode - $f_2 = 187.96$	96
6.15	H3 - Simplified model for simulations	97
6.16	H3 Clockwise - First mode - $f_1 = 15.39$	98
6.17	H3 Clockwise - Second mode - $f_2 = 15.39$	98
6.18	H3 Clockwise - First mode - $f_1 = 12.30$	99
6.19	H3 Clockwise - Second mode - $f_2 = 12.30$	100

6.20	H3 - First mode - $f_1 = 16.03$	101
6.21	H3 - Second mode - $f_2 = 16.04$	101
6.22	H3 Clockwise - Mesh optimization	103
6.23	H3 Counterclockwise - Mesh optimization	103
6.24	H3 - Mesh optimization	104
6.25	Vibration test setup	105
6.26	C3 - Constraint in vibration test setup	106
6.27	C3 - Prototype hit by hammer	106
6.28	H3 Clockwise - Constraint in vibration test setup	108
6.29	H3 Clockwise - Prototype hit by hammer	109
6.30	H3 Counterclockwise - Prototype hit by hammer	110
6.31	H3 - Prototype hit by hammer	112
7.1	HCT quadrifilar helical antenna [27]	116
7.2	Coatings' failure related to thermal cycling and AO erosion [4]	117
7.3	Rendering of prototype H3	118
7.4	H3 - Assembled prototype comparison	118

List of Tables

2.1	Types of satellites [2]	4
3.1	Materials' issues in space	35
3.2	Summary of different materials' classes	42
3.3	Properties of commercially available polymers for space applications	43
4.1	Antenna's project requirements	54
4.2	Folding mechanisms for different antennas [48]	55
4.3	Types of antennas	58
5.1	Parameters for theoretical calculations	62
5.2	Best design parameters for helix antenna	66
5.3	Connex3 materials	77
5.4	Dimensional comparison - H1 and H2	79
5.5	Dimensions of H3	83
6.1	Recovery ratio of H3	93
6.2	Comsol - Materials' properties for prototype C3	95
6.3	Summary of simulated eigenfrequencies	102
6.4	C3 - Experimental results of vibration testing	107
6.5	H3 Clockwise - Experimental results of vibration testing	110
6.6	H3 Counterclockwise - Experimental results of vibration testing	111
6.7	H3 - Experimental results of vibration testing	112
6.8	Simulated vs. experimental results of vibration testing	113
7.1	Folding mechanisms for different antennas [48]	117

Abstract

The CubeSat project is an innovative approach to design, manufacture and launch satellites into space, allowing small companies and universities to reach the Low Earth Orbit at a fraction of the cost and complexity of a normal satellite. One of the critical components of a CubeSat is the antenna, fundamental for bidirectional communication with the ground stations. This kind of space structure needs to be folded and deployed once it reaches the orbit, possibly without active actuation that would increase the total weight of the satellite. Moreover, space is a very complicated environment that pushes requirements on materials' performances to its outermost limits: high/low temperature cycles, high vacuum, solar radiation, debris and atomic oxygen are only a few of the challenges that need to be overcome in order for a space structure to survive for the expected service life of five years. In this thesis, the mechanical design of an antenna for this application is studied, focusing on passive deployment mechanisms obtained through 3- and 4-D printing. After trying multiple designs, the final choice is a quadrifilar helical antenna, manufactured with 4D printing and folded through a programming phase allowing for temperature change. In this way, once in orbit and upon heat application, the deployment can happen. Testing was performed to assess the mechanical properties of the design, and the main limitation to the feasibility of such a project is connected to manufacturing and materials palette. This first proof of concept explores the infinite possibilities of 4D Printing, which will lead to innovative approaches for design and manufacturing in the close future.

Sommario

Il progetto CubeSat ha permesso un approccio innovativo alla progettazione, produzione e lancio in orbita di satelliti prodotti da piccole imprese o università ad un prezzo molto ridotto rispetto a quelli di un satellite tradizionale. Uno dei componenti più importanti di un satellite è l'antenna, fondamentale nelle comunicazioni da/con la base a terra. Questo tipo di strutture spaziali deve poter essere riposto all'interno del satellite e aperto una volta raggiunta l'orbita, preferendo un'attuazione passiva per evitare di aggiungere ulteriore peso ed ingombro. Inoltre, l'ambiente spaziale è uno di quelli più difficili in cui un materiale possa trovarsi a causa di temperature estreme, detriti spaziali, alto vuoto, radiazione solare e altri fattori, che possono portare la vita di servizio a meno di cinque anni (durata media del programma). In questa tesi viene studiato la progettazione meccanica di un'antenna, concentrandosi su meccanismi di attivazione passivi ottenuti tramite stampa 3D e 4D. Dopo aver studiato numerosi design, la scelta finale ricade su di un'antenna ad elica quadrifilare, prodotta tramite stampa 4D e ripiegata attraverso un processo di programmazione grazie ad una variazione di temperatura. In questo modo, una volta che il satellite raggiunge l'orbita l'antenna può essere aperta grazie ad un aumento di temperatura. Per valutare le proprietà del progetto finale sono stati svolti dei test meccanici, anche se la limitazione di questo progetto è risultata essere principalmente legata al processo di produzione e alla scelta di materiali disponibili. Questo studio preliminare apre ad innumerevoli possibilità legate alla stampa 4D che può portare ad approcci innovativi per il design e la produzione nel prossimo futuro.

Estratto in lingua italiana

Introduzione Il progresso nei processi di produzione e nello studio dei materiali ha portato ad una miniaturizzazione generale di apparecchiature e strumentazioni. Questo vale a maggior ragione per applicazioni ad alta tecnologia ed alto costo quali quelle connesse all'esplorazione spaziale, come ad esempio i satelliti (Tabella 1). A partire dal 1999, il progetto CubeSat si occupa della standardizzazione di pico-satelliti (volume $10 \times 10 \times 10 \text{ cm}^3$) [1]; questa innovazione ha dato la possibilità a piccole aziende e università di portare in orbita piccoli carichi a prezzi contenuti, in un'ottica di avvicinamento di una più ampia platea all'utilizzo dello Spazio.

Tabella 1: Tipologie di satelliti [2]

Tipologia	Massa [kg]	Costo [US\$]	Tempo di sviluppo [anni]
Satelliti convenzionali	>1000	0.1 - 2 miliardi	>5
Satelliti medi	500-1000	50 - 100 milioni	4
Mini-satelliti	100-500	10 - 50 milioni	3
Micro-satelliti	10-100	2 - 10 milioni	1
Nano-satelliti	1-10	0.2 - 2 milioni	1
Pico-satelliti (CubeSats)	<1	20 000 - 200 000	<1
Femto-satelliti	<0.1	100 - 20 000	<1

Una delle componenti principali di un satellite è l'antenna, che permette le comunicazioni con il suolo: negli ultimi venti anni, una varietà di tipologie di antenne sono state usate nei CubeSat, permettendo di avere emissioni a diverse frequenze. Lo scopo di questa tesi è lo sviluppo di un'antenna con frequenza di emissione nel range delle UHF, tra 0.3 and 3 GHz, per favorire le telecomunicazioni in paesi in via di sviluppo. Le antenne più promettenti per questo tipo di applicazione sono quelle elicoidali e le cosiddette "a tromba".

Uno studio sulle proprietà dei materiali, basato sull'utilizzo di CES Edupack, è stato eseguito e introdotto nel Capitolo 3. Date le piccole dimensioni del CubeSat è infatti essenziale che la struttura dell'antenna possa essere ripiegata all'interno del corpo del satellite, in attesa di essere aperta una volta raggiunta la bassa orbita terrestre. Per questo motivo, i materiali a memoria di forma sembrano avere del potenziale in questo campo di applicazione. Per quanto riguarda la produzione, la metodologia da utilizzare è sicuramente la stampa 3D: in particolare, a partire dal 2014 Tibbits [3] ha definito la stampa 4D come un processo di stampa 3D che cambia nel tempo grazie all'applicazione di uno stimolo, generalmente una variazione di temperatura.

Nel Capitolo 4 l'antenna più adeguata al progetto viene selezionata, considerando sia i problemi di stoccaggio in fase di lancio che l'adeguato range di emissione. Il design e la produzione di diversi prototipi vengono studiati nel Capitolo 5, cercando di sfruttare al meglio i vantaggi della manifattura additiva e dei polimeri a memoria di forma; in particolare, nel prototipo a doppia elica è stata utilizzata una stampante 3D multimateriale che permette alla struttura di avere parti flessibili costruite in parallelo a parti strutturali, massimizzando la resistenza alle interfacce e permettendo un ripiegamento ottimale.

Infine, nel Capitolo 6 le due strutture più promettenti vengono analizzate e comparate. In primo luogo, uno studio sul dispiegamento è portato a termine sul prototipo interamente stampato in 4D, e in secondo luogo un'analisi sulle vibrazioni.

Per quanto riguarda le vibrazioni vengono comparati i risultati di un test sperimentale e quelli del corrispondente modello agli elementi finiti.

Analisi dei materiali Nel Capitolo 3, viene analizzato l'ambiente spaziale in cui sarà lanciato il satellite e di conseguenza tutti i rischi che vanno ad accorciare la vita di servizio dell'antenna stessa. Ancora oggi, il metodo più attendibile per lo studio del comportamento dei materiali è che vengano esposti direttamente all'atmosfera spaziale con esperimenti sulla stazione spaziale internazionale [4]; questo ambiente infatti è così aggressivo che risulta complicato ideare delle apparecchiature in grado di combinare tutti gli effetti degradanti simultaneamente.

Il primo problema riscontrato nell'orbita terrestre bassa è legato ai cicli termici, con una temperatura che varia da -125 a 125 °C e sono particolarmente dannosi per i polimeri poiché l'antenna ha bisogno di stabilità e le proprietà del materiale selezionato devono essere costanti in tutto l'intervallo delle temperature. I cicli termici e il vuoto sono i due effetti più studiati in modo combinato, come dimostra il lavoro di Torralba and Aranda [5] in cui una camera termica sottovuoto viene utilizzata. Il problema principale del vuoto è determinato dall'outgassing del materiale, ovvero dal rilascio di sostanze volatili quando sottoposto a basse pressioni/vuoto. Per mitigare l'infragilimento del materiale è possibile ricorrere a cicli di outgassing a livelli di pressione inferiori a quelli che si andranno ad incontrare nella bassa orbita terrestre (alto vuoto, fino a 10^{-3} Pa).

Un altro problema rilevante è causato dalla radiazione ultravioletta emessa dal Sole, che danneggia in modo grave i materiali (in particolare, è responsabile della rottura dei legami organici come C-C e C-O [6]).

Nella Tabella 2, è possibile vedere un riassunto dei problemi analizzati (da ++ migliore a +/- peggiore).

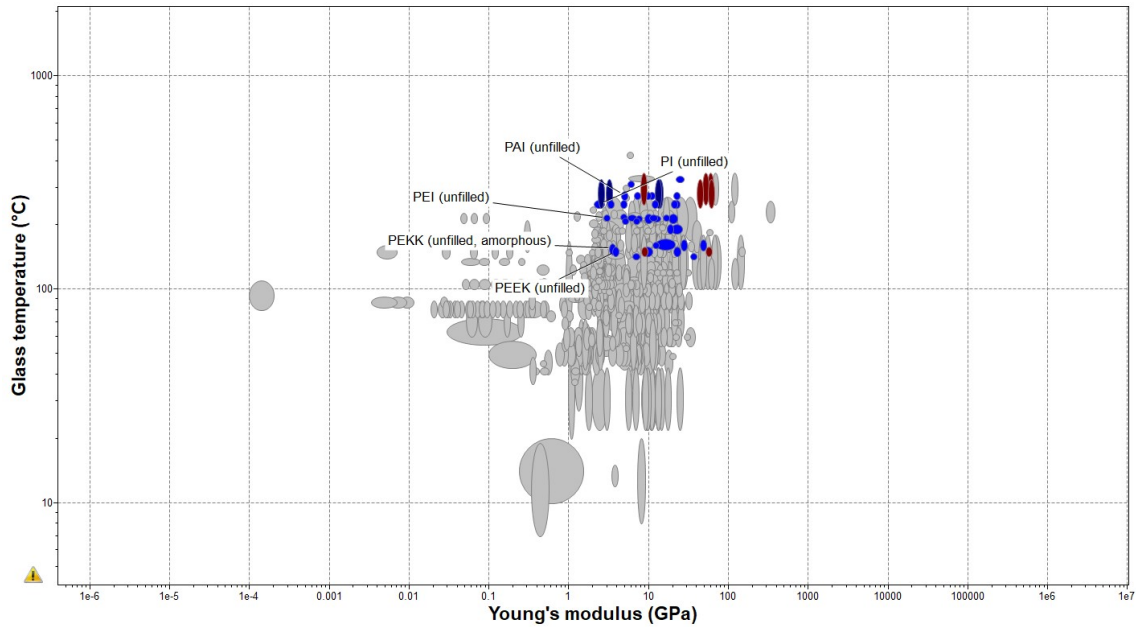
Tabella 2: Problemi dei materiali nell'orbita terrestre bassa

	Outgassing	UV	Cicli termici	Comportamento
Metalli	++	++	++	Stabile
Termoindurenti	+	+	+	Stabile
Termoplastici	+/-	+/-	+/-	Variabile

Alcuni di questi effetti sono stati inoltre analizzati con l'aiuto del software commerciale CES EduPack, in cui sono disponibili dati su oltre 3900 materiali; ovviamente, questo è uno studio preliminare e non può sostituire i test ideati caso per caso.

Questo software è in grado di paragonare le proprietà dei materiali di una determinata classe, e permette di selezionare limiti massimi o minimi sulla base dei requisiti di progetto. In questa tesi sono stati presi in considerazione metalli e polimeri: un limite minimo di 1 GPa è stato assegnato al modulo di Young, per permettere alla struttura dell'antenna di essere abbastanza rigida per questa applicazione. Per quanto riguarda i polimeri, sono state considerate la temperatura di transizione vetrosa, la resistenza alla radiazione UV e la massima temperatura di esercizio in funzione del modulo di Young (critico per i polimeri, essendo meno rigidi dei metalli). Per i metalli sono stati selezionati il modulo di Young, la massima temperatura di esercizio e la resistenza agli UV in funzione della densità (la grandezza critica per i metalli, visto il limite di peso del CubeSat).

I grafici sono disponibili nelle Sezione 3.2; in Figura 1 e' possibile vedere il grafico dei polimeri per quanto riguarda la temperatura di transizione vetrosa rispetto al modulo di Young. Un minimo di 150 °C è stato selezionato come limite minimo, per assicurare una continuità nelle proprietà della struttura in orbita. Le zone colorate rappresentano i polimeri che sono risultati idonei alla selezione.

Figura 1: Polimeri - T_{glass} vs. modulo di Young

Per una panoramica dei materiali analizzati si rimanda alla Tabella 3.2, dove sono raccolti i dati delle grandezze descritte in questo capitolo.

In Figura 2, è possibile vedere uno schema che racchiude tutte le proprietà che dovrebbe avere il materiale per essere considerato il perfetto candidato per questa applicazione.

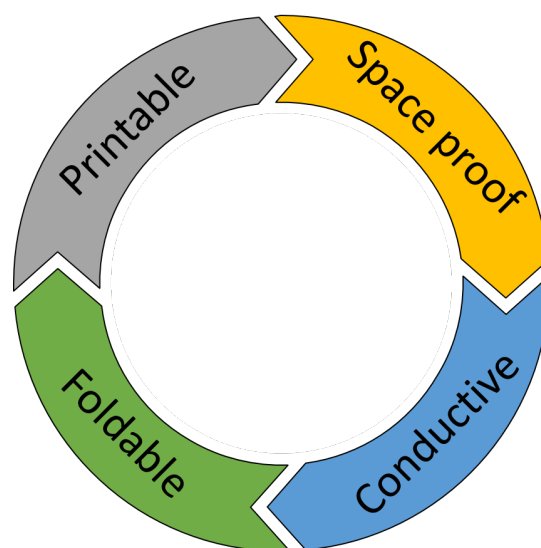


Figura 2: Requisiti per la progettazione dell'antenna

A questo punto i metalli vengono messi da parte, perché per quanto riguarda il 4D printing il processo non è ancora stato perfezionato. Ci sono infatti degli studi sulla stampa SLM di leghe di Nickel e Titanio (Nitinol, lega a memoria di forma), ma le parti finali risultano troppo porose e quindi la programmazione non è ottimale ([7, 8]). Inoltre, lo scopo di questa tesi è quello di produrre un prototipo, e le stampanti per la produzione di plastiche sono più diffuse e il processo meno costoso. Per questo motivo la scelta più intelligente per l'antenna che verrà prodotta in futuro ricade su polimeri testati e approvati da NASA o ESA come il Windform XT 2.0 [9]. Purtroppo, la disponibilità di materiali per la stampa 4D ad oggi è ancora molto limitata, ma trattasi di un campo molto innovativo e pertanto al centro dell'attenzione per quanto riguarda la comunità scientifica.

Selezione dell'antenna Vengono ora introdotte le caratteristiche fondamentali che un'antenna deve avere per emettere un'onda elettromagnetica dallo spazio, e in modo tale da effettuare una scelta ponderata sulla tipologia di antenna da progettare e produrre.

Le grandezze fondamentali per un'antenna montata su un satellite sono il guadagno, la polarizzazione e la direzionalità; per una spiegazione accurata si faccia riferimento alla sezione 4.1. Tenendo conto di queste grandezze elettromagnetiche e degli altri requisiti di peso e volume dettati dal concetto del CubeSat, i requisiti per l'antenna per questo progetto sono riportati in Tabella 3.

Tabella 3: Requisiti di progetto per l'antenna

Requisiti	
Compartimento di stoccaggio	95 x 95 x 95 mm ³
Massa	< 400 g
Frequenza di emissione	300 MHz - 3000 MHz
Minimo guadagno	> 10 dBi
Polarizzazione	Circolare
Rigidezza della struttura aperta	> 1 Hz
Temperatura di utilizzo	-120 °C +120 °C
Volume della camera di stampa	490 x 390 x 200 mm ³

La rigidezza è qui riportata in hertz perché si riferisce alla minima frequenza del più basso modo di vibrazione della struttura sviluppata, ovviamente nella configurazione aperta.

A questo punto è opportuno portare a termine uno studio che considera i parametri definiti e le tipologie di possibili antenne; per fare ciò, tutti i requisiti sono analizzati uno ad uno e le antenne che non soddisfano uno o più di essi vengono eliminate, come è possibile leggere nella sezione 4.3.1. Alla fine, sono rimaste solo le antenne elicoidale e a tromba, ma poiché l'antenna elicoidale è meno ingombrante e offre la possibilità di avere guadagni adeguati grazie alla sua conformazione quadrifilare, questa ultima verrà analizzata nel capitolo della progettazione.

Progettazione e produzione del prototipo In questo capitolo, due tipologie di design che permettono il ripiegamento e l'apertura di un'antenna ad elica quadrifilare sono analizzate. Prima di questo studio, è stato creato uno script su MatLab per trovare numericamente alcuni parametri dimensionali come il raggio e l'altezza, in

funzione della frequenza di utilizzo.

Il primo design utilizza una struttura modulare a cubi, che serve da rinforzo per garantire al conduttore metallico la giusta rigidezza, fondamentale per una trasmissione del segnale continua e senza interferenze; è possibile vedere l'idea di progettazione in Figura 3.

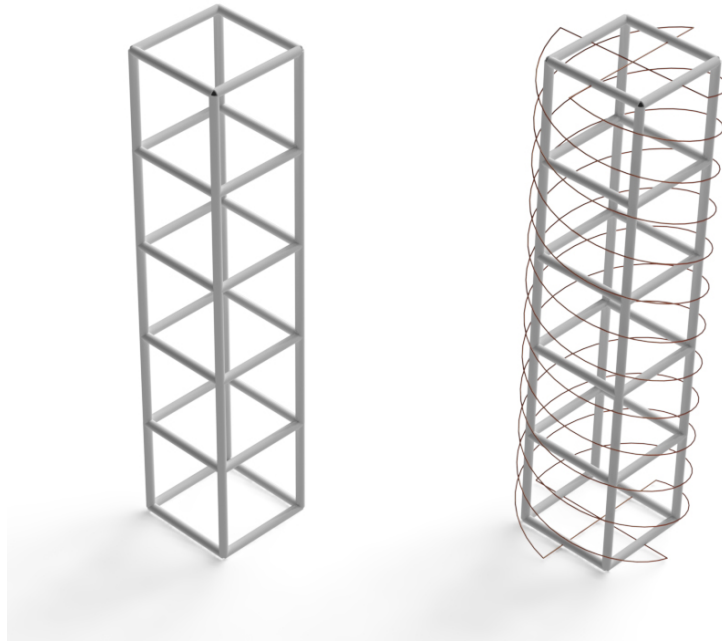


Figura 3: Rendering della struttura preliminare a cubi

Dopo alcuni tentativi di design, questo prototipo è stato prodotto stampando in 3D delle basi a sezione quadrata (parti bianche in Figura 4, stampate in ABS), e utilizzando un metro da cantiere tagliato per creare gli spigoli del cubo (parti gialle in Figura 4). Questo tipo di geometria ha infatti proprietà meccaniche molto interessanti, e una volta ripiegato riesce a tornare alla forma originale senza generare deformazioni permanenti (ha solo componente di deformazione elastica). Sfortunatamente, per questo tipo di struttura la stampa 4D è ancora impossibile, e si pertanto è ricorso all'assemblaggio.



Figura 4: Rendering of prototype C3

L'idea per la seconda famiglia di design deriva dalla considerazione che la struttura ad elica quadrifilare sia già abbastanza rigida da sostenere il proprio peso. Questa struttura è stata progettata per essere stampata in 4D, ovvero utilizzando una stampante 3D e procedendo con il processo di programmazione. In questo caso è stato utilizzata una stampante 3D multimateriale (Stratasys Connex3), che ha permesso di ottenere una struttura con la proprietà di poter diminuire l'angolo alla base al minimo durante il ripiegamento grazie all'utilizzo di un materiale elastomerico nei pressi della giunzione tra i bracci elicoidali e la base, come è possibile vedere in Figura 5.



Figura 5: Rendering del prototipo H3

Nella rappresentazione è mostrato il prototipo finale, composto da una struttura elicoidale sviluppata in senso orario e di una in senso antiorario, per dare rigidezza e garantire un buon comportamento.

Test e risultati I due prototipi appena descritti sono quelli analizzati nel Capitolo 6. Per prima cosa, il prototipo a doppia elica è stato programmato usando una successione di procedure di riscaldamento e raffreddamento, che ha permesso di ottenere un rapporto di recupero della forma (da stivata ad estesa) di circa il 90%. Successivamente, un modello agli elementi finiti è stato sviluppato per simulare le frequenze naturali di vibrazione, che sono state poi confermate sperimentalmente mediante valutazioni video ad alta velocità. Ciò ha permesso di confermare la correttezza del design per quanto riguarda i requisiti imposti dalla NASA sulla rigidezza, e considerando gli altri numerosi vantaggi dati dalla stampa 4D si può dire che questa tesi introduca dei metodi innovativi nello sviluppo di soluzioni a basso costo e peso per la realizzazione di strutture spaziali a memoria di forma.

Chapter 1

Introduction

Telecommunications in third-world countries are nowadays still a big challenge: huge distances, lack of political stability and low budget available are only some of the problems connected to the implementation of an efficient network infrastructure, which would require high initial investments and maintenance costs. An answer to this problem has been possibly found in the development of a low-cost satellite, entirely designed at the Engineering Design and Computing laboratory (EDAC) of the Swiss Federal Institute of Technology in Zurich and the Swiss company Orbitare.

Satellites developed following the CubeSat guidelines are small, characterized by simple design and lower launching costs compared to conventional ones, but also offering a limited payload. For this reason, most of the mechanisms that are needed for operations need to be folded during launch and unfolded only when the satellite reaches its orbit.

The development of the CubeSat is thus divided into three subprojects:

- Deployment of solar array for power;
- Mechanical opening of the lid;
- Deployment of the antenna for telecommunications.

The first two subprojects were developed in other master thesis, and scope of this work is to target the last one. In particular, by harnessing the peculiarities of 3D

printing applied to self-actuating structures, the concept of 4D printing is explored for space applications.

After a brief introduction on the state of the art of commercial and scientific literature about space antennas and satellites, the materials' requirements for such an application are studied in Chapter 3. Afterwards, different types of antenna are presented and the parameters for the project are defined in Chapter 4. The final choice on the design can thus be made, and the first prototypes build using a 3D printer in Chapter 5. In particular, a study on the design of the prototypes is performed: a MatLab script is used to establish the best dimensions' combination as a function of the antenna frequency. Finally, in Chapter 6 "programming" and mechanical testing of the produced antenna structures are performed: in fact, stiffness requirement are particularly critical for reaching the expected service life of the antenna, and thus a vibration analysis, both simulated and experimental, is essential for the design phase.

Chapter 2

Theoretical background

In this chapter, an overview of the available literature is explored; at the beginning the focus will be on the satellites, in particular on CubeSats. Afterwards, the most common antennas used for this satellite are considered to better understand the state of the art of the topic. At the end, manufacturing techniques and materials related to 3D and 4D Printing will be analyzed.

At the beginning of space exploration, satellites were small. During years, since the functions became more complex, they increased in weight and size. Small satellites are a new generation of satellites which are smaller, cheaper and very reliable. These could develop thanks to technological advancements such as miniaturization, integrated circuits, solid state memories and advanced manufacturing processes [2].

The small satellites era began in 1981 with the launch of UoSAT-1, built by university students and radio amateurs; it was the first satellite to have an on-board computer and it weighted around 50 kg. The remarkable feature about these satellites is that anyone with a basic engineering knowledge can build one using off-the-shelf devices rather than space-qualified components [10].

In Table 2.1, several types of satellites are presented. In recent years there has been a general migration towards small devices, which remarks the technology general improvement. A smaller device means also lower costs and faster manufacturing time [10, 11].

Table 2.1: Types of satellites [2]

Type	Mass [kg]	Cost [US\$]	Development time [years]
Conventional Large satellite	>1000	0.1 - 2 billion	>5
Medium satellite	500-1000	50 - 100 million	4
Minisatellite	100-500	10 - 50 million	3
Microsatellite	10-100	2 - 10 million	1
Nanosatellite	1-10	0.2 - 2 million	1
Picosatellite (CubeSat)	<1	20 000 - 200 000	<1
Femtosatellite	<0.1	100 - 20 000	<1

The possibility to build satellites was warmly welcomed by unconventional institutions, and one of the first CubeSat was developed by the California Polytechnic State University and Stanford University in 1999. Then, the CubeSat program developed a picosatellite standard still used nowadays, starting from the satellites developed for Stanford's Opal mission; this project involved a multidisciplinary team of engineering undergraduate students. In particular, CubeSats can serve as facilities for in-space experimentation, as well as a means of space-qualifying future small-satellite hardware [11].

To sum up, a CubeSat is a simplified satellite in which one unit has a $10 \times 10 \times 10 \text{ cm}^3$ volume. The main drawback is that these apparatuses are power limited, because the energy available only comes from arrays of solar cells which in general have a low efficiency. Therefore, they can only be sent into Low Earth Orbit (LEO - 200 to 1000 km from the Earth surface).

2.1 Antennas in CubeSats

The combination of small volumes and simple antenna designs makes difficult to optimize the signal, especially when trying to reduce the project's price at minimum. In the next section, some of the most common antennas adapted for CubeSats are presented to give an idea of the available options.

2.1.1 Monopole and dipole antenna

Monopole and dipole antennas are widely spread for wireless communication thanks to their simple geometry. They are wire radiators which consist of a linear wire fed at one extremity or at the centre (monopole or dipole), as in Figure 2.1 [12].



Figure 2.1: Dipole antenna [12]

These antennas have been widely used in space exploration for low-gain Telemetry, Tracking and Command (TT&C); they have been the only antennas in the first generation of low Earth orbit satellites due to their omni-directional radiation pattern, which made control from the ground easier [2].

Both OPAL satellite and PolySat missions used dipole antennas in the late 90's. The engineers decided to use it because the antenna could be built with spring tape available at any hardware shop. The CubeSat had four independent dipole antennas folded on one face of the box; the design of the branches is flexible and it holds in shape during the deployment. To open the antennas, it is enough to make a current flow through the nichrome wire, which will heat and release the branches (Figure 2.2) [13].



Figure 2.2: Deployed antennas in PolySat satellite [13]

2.1.2 Microstrip antenna

Nowadays, these antennas are widely available on the market. They are made of a metallic patch element printed on a thin insulating layer above a ground plane; usually the patch has a rectangular or circular geometry. The research on this topic has been prosperous in the last decade, and it provides many fast improvements and new applications. Microstrip technology is very flexible, it is thus possible to adapt the shape to different geometry and materials; moreover, these antennas can be low-cost. The main limitation is in the narrow bandwidth, and so the overall efficiency (gain) is much lower than the one of other antennas [2].

In 2015, Islam et al. [14] developed a circularly polarized microstrip antenna to be mounted on the 3-modules CubeSat HORYU-IV. The antenna was mounted on the external surface of the satellite, thus it did not need any deployment mechanism. In Figure 2.3, it is possible to see the prototype mounted on the aluminum chassis of the CubeSat (antenna highlighted in the red circle).

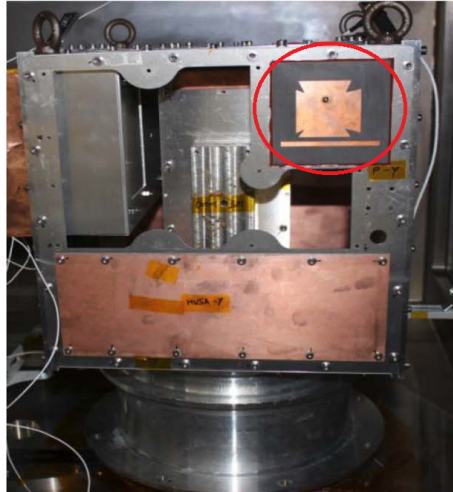


Figure 2.3: Top view of the microstrip antenna [14]

In 2011, Nascetti et al. [15] also developed a patch antenna which was circularly polarized. This polarization is needed in CubeSats to alleviate orientation-related issues of the receiving base antennas. In both works, the maximum gain achieved was 7.3 dBi.

In the two works just cited, it is possible to notice that the S-band is a common frequency range for CubeSats, as it is one of the international amateur satellite frequency ranges. It ranges from 2 to 4 GHz [16].

2.1.3 Conical log-spiral antenna

These antennas were common in early spacecrafts, for example in the first Russian Venus probes Venera, designed to study Venus surface between 1961 and 1983. Later, in the mission Mars 3, a couple of these antennas were used for TT&C (Telemetry, Tracking and Command) purposes combined with a big parabolic reflector for the transmission of data (Figure 2.4) [2].

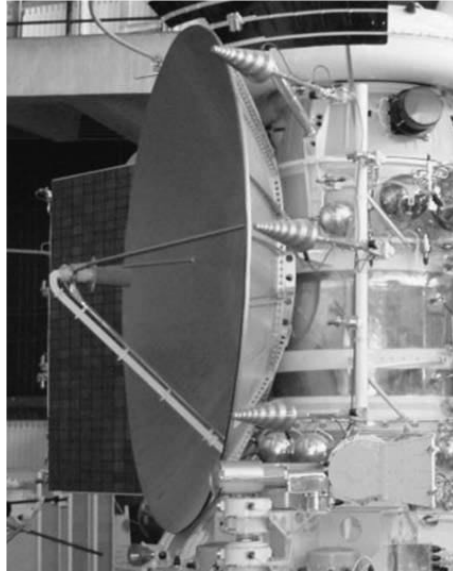


Figure 2.4: Antennas of Mars 3 [2]

In 2016, Olson et al. [17] did a study on different deployable helical antennas for CubeSats. The conical log-spiral antenna (CLSA) appeared to be a good choice for a wideband antenna operating in the Ultra High Frequency range (UHF, between 0.3 and 3 GHz [16]).

Regarding the manufacturing of this type of antenna, Sakovsky et al. [18] combined the dual matrix composites to the deployable booms, in which the hinges allow the boom flattening and folding. The deployment scheme proposed to make the antenna fit the small volume was based on the z-deployment (Figure 2.5). This kind of folding is constrained by the elastic limit of the structure itself; the simplest example of storable tubular extendable member (STEM) was used in space since 1988.

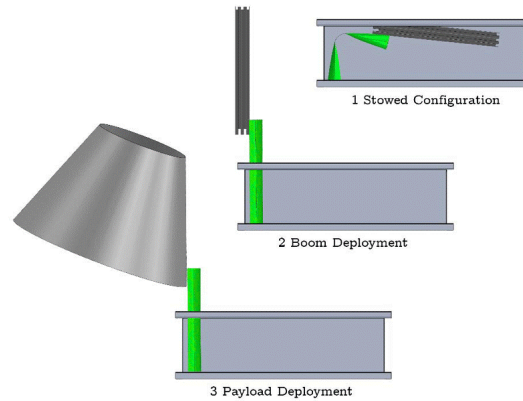


Figure 2.5: CLSA z-deployment [18]

Another example of folding mechanism for this antenna was proposed by the same research group and is based on the origami scheme. The shell is flattened with two creases and then the triangular shape obtained is folded following the Miura-Ori pattern; this pattern uses fold lines to couple lateral and transverse reduction, thus it is possible to open the structure by just pulling two diagonally opposed corners. To clarify the concept, the scheme is presented in Figure 2.6 [19].

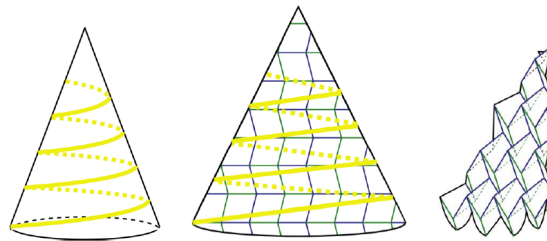


Figure 2.6: Folding mechanism: Miura-Ori [19]

2.1.4 Parabolic reflector

These antennas are the most employed in missions since the beginning of space exploration; they can reach very high gains and directivity. During years, these antennas evolved in shape and number of feeds, and nowadays they can be used in most of the frequency ranges.

One of the first satellite with this antenna was the NASA ATS-6, launched in 1974; the diameter of the reflector was 9.12 m, it had 48 ribs and it weighed 60 kg [2].

From 1999, Northrop Grumman Corporation is developing the so called AstroMesh, which is a mesh reflector for large aperture space antennas. Compared to the previous bulky systems, these reflectors are low weight, cheap and can be stored in a small volume. This corporation developed for twelve years seven generations of reflectors from 2.5 to 12.25 m with over 350 tested ground deployments without any failure. The AstroMesh reflectors are still available on market and sold to the public (Figure 2.7) [20, 21].

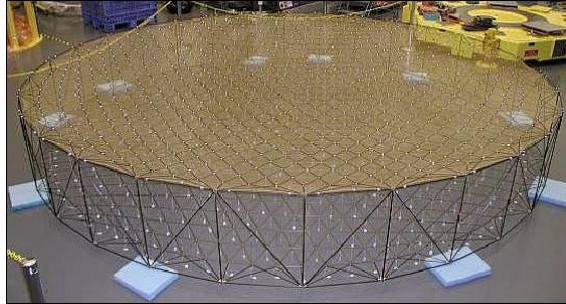


Figure 2.7: 6.5 m AstroMesh [21]

2.1.5 Single and multiple helical antenna

Helical antennas are circular polarized and can emit in wide-band. The simplest form possible is the single helix one, in which a conducting wire is wound around a central axis. This antenna has different modes of radiation, the normal mode (broadside) and the axial mode. In normal mode its behaviour is similar to a short dipole one, radiating normal to its axis, while in the axial mode (end-fire) the result is a main lobe directed along its axis as in Figure 2.8. To operate in the latter mode, both the helix diameter and the pitch need to be large fractions of the wavelength. Usually, it is common to have a ground plane, but in the absence of it the antenna will have the main lobe in the backfire direction (towards 180°).

If the dimensions or the number of wires are changed, it is possible to control the radiation characteristic; this is why bifilar and quadrifilar helical antenna, respectively with two and four wires, are widely used in TT&C nowadays [2].

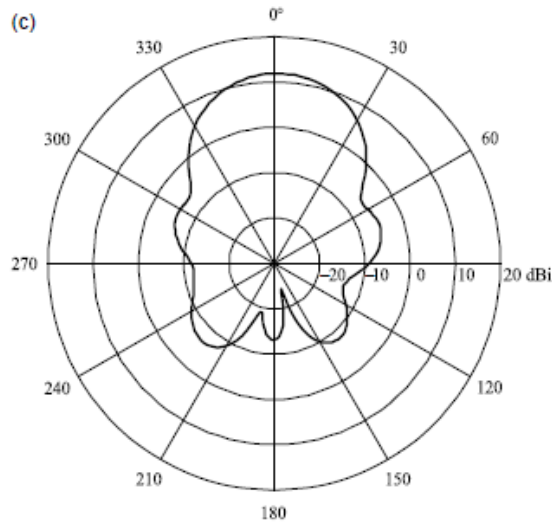


Figure 2.8: Gain pattern of a helical antenna in axial mode [2]

Since the dimensions of this kind of antenna are quite large with respect to the limited space available in a CubeSat, there is a lot of ongoing research regarding efficient deployment solutions. The research group lead by Sergio Pellegrino at the California Institute of Technology explored many ways to deploy helical antennas both axially and radially. In 2012, they did a study about the geometry and hindrance of different antenna types at the undeployed state, to understand which antennas were feasible to emit in the UHF range. Regarding quadrifilar helical antenna (QHA), the first concept analyzed for a deployment in both radial and axial direction was the one of an expanding circular pantograph. The main problems with this design are the complicated mechanical structures with many connections and the limited capacity to self-deploy [19].

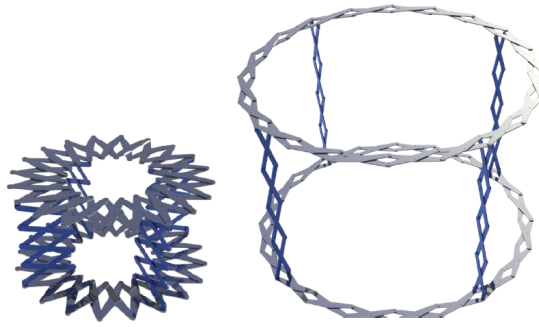


Figure 2.9: Undeployed and deployed QHE [19]

In 2013, the German Aerospace Centre developed a self-deployable helical antenna. The helical design is interesting as it can be combined with the mechanical properties of a spring, which on the other hand is difficult to fold. The project intended to deploy a spring compressed in 10 cm up to a 4 m length, so it focused on the axial unfolding. The structure was manufactured using a carbon fibre core coated with a conductive membrane and it was tested at zero G during a parabolic flight. To ensure an acceptable linear unfolding, some stabilizing cords were added, as in Figure 2.10 [22].

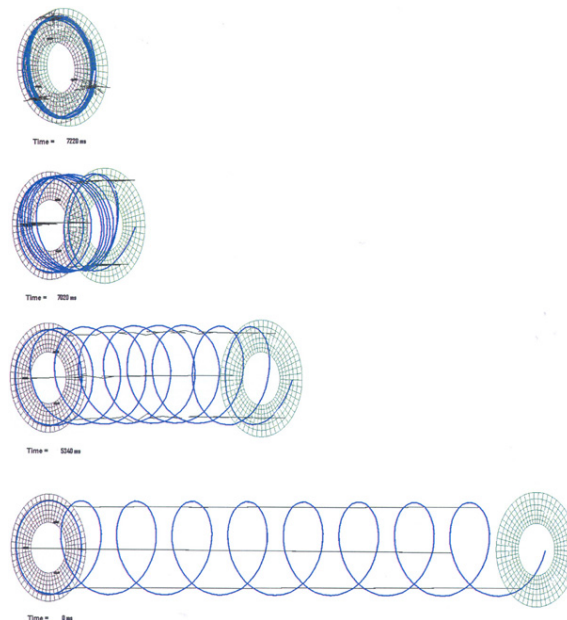


Figure 2.10: Simulated deployment [22]

In 2015, a creative way to fold an antenna along both radial and axial directions

was developed at the Northrop Grumman Aerospace Systems. As it can be seen in Figure 2.11, the structure is flexible and can be folded and rolled [23].

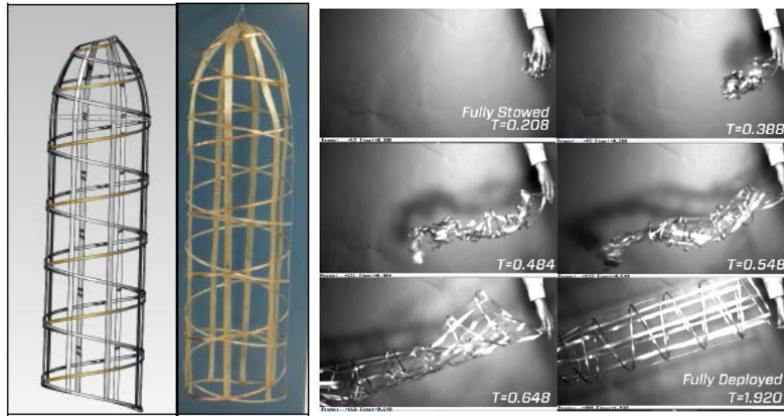


Figure 2.11: Deployed antenna and unfolding sequence [23]

A totally different approach was introduced at the Georgia Institute of Technology, exploiting the high conductivity of some liquid metal alloys and micro-fluidics (Figure 2.12). Thanks to the new advancements in the 3D printing of soft materials, a “tree” capable of integrating different types of antennas was built, and reconfiguration of frequency, radiation pattern and polarization was possible thanks to the filling/unfilling of the liquid metal alloy that can fold/unfold the origami scaffolding structure in which the antennas are embedded. As an example, a helical and a zigzag antenna were built in the scaffold and they were studied, obtaining good results in the S band [24].

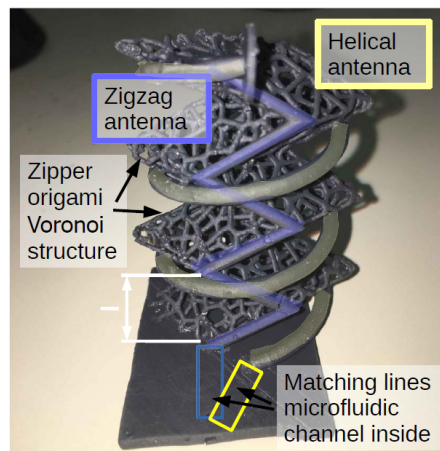


Figure 2.12: Microfluidics-based antenna [24]

2.2 Materials for space antennas

Space is a very harsh environment, therefore the selection of materials is always challenging. Moreover, antennas are always in direct contact with the space atmosphere being external appendages, and the choice in this situation is even more difficult. Sun radiation, debris, temperature effects and thermal cycling are only some of the environmental threats that the spacecraft would face. For this reasons, each mission sets its own variables such as mission length, orbital parameters and solar events to ensure the best performance.

Nowadays, the most important categories of materials for deployable antennas are metal alloys, in particular the Shape Memory Alloys (SMAs), and shape memory polymer composites (SMPCs). On the latter there is a lot of ongoing research, because it ensures lower costs, lower weight and a wider range of possibilities; in fact, SMAs have been discovered in 1930s while the shape memory behaviour of polymers is a relatively new thread, and it has been exploited in some recent manufacturing technologies.

2.2.1 Metals and Alloys

As introduced earlier, the shape memory behaviour of alloys is exploited to create antennas that can deploy upon a stimulus, and therefore being stored in small compartments (i.e. CubeSats); this behaviour was first reported in the 1930s with an Au-Cd alloy.

Shape memory alloys undergo a phase transformation from austenite to martensite due to a change in temperature and/or a mechanical load; the functionality of these alloys depends on both the transformation temperatures (function of the material) and the operational temperature. Figure 2.13 shows a schematic of the phenomenon; austenite has only one possible lattice orientation, while martensite has multiple ones. Upon heating, the phase structures of the martensite must revert to the unique austenite orientation (memory effect) and the material recovers its original shape [25].

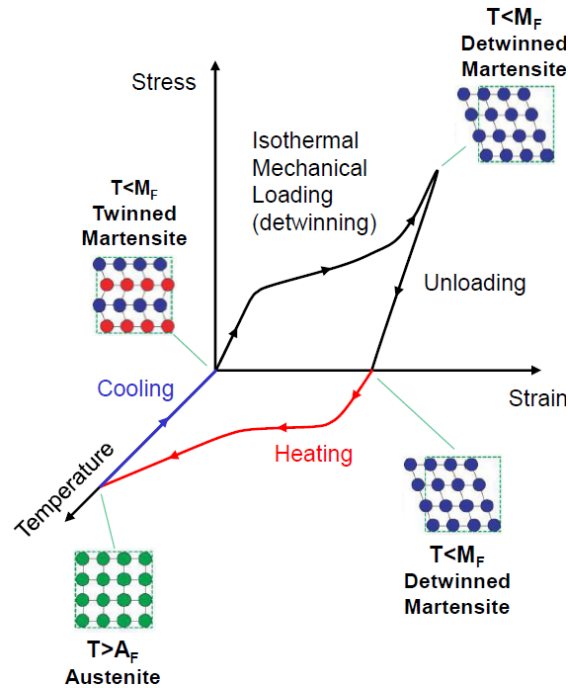


Figure 2.13: SMA behaviour scheme [25]

In 1968, the research on Ti-Ni alloys (e.g. Nitinol) was already at a good point [26]. In a study on the 55-Nitinol (55% w/t Ni), an example of a self-deploying disc-on-rod antenna was described; by beating up the structure above the transition temperature ($150\text{ }^\circ\text{C}$), the structure recovered its original unfolded shape (Figure 2.14).

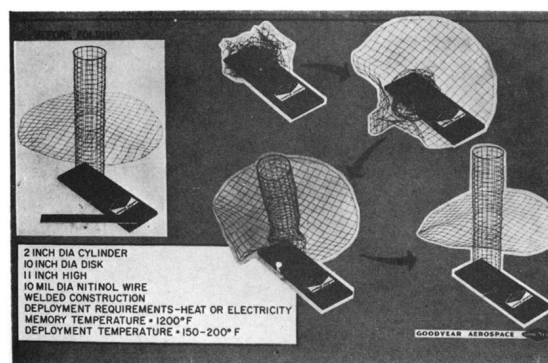


Figure 2.14: 55-Nitinol disk-on-rod antenna [26]

More recently, the company Helical Communication Technologies (HCT) developed a deployable QHA for a CubeSat. To achieve the small size, Nitinol properties were again exploited; wire filars were manufactured with this material and a small

circuit was attached to heat them after the launch and make them recover their original shape. The mechanism is highlighted in Figure 2.15. These antennas are nowadays available on the market for more than 10 000 \$ [27].



Figure 2.15: HCT quadrifilar helical antenna [27]

2.2.2 Polymers and composites

Nowadays, the polymer matrix composites are the most used category of materials for the space antenna manufacturing. They show an excellent stiffness-to-mass ratio and they can be tailored for every application, which is of big relevance for antennas due to polarization and interference issues. To perform well in the space environment, polymers have to face some challenges such as the thermal stability, which is taken for granted in the case of metallic materials. Among the space-certified polymers, we can quote PE (Polyethylene, commercial Mylar), PI (Polyimide, commercial Kapton). As composites, we usually have matrices as epoxy and cyanate ester resins combined with unidirectional laminae or charges [2].

As a research example, the composite material studied by a group at Amrita university is reported. Polyetherimide (PEI, commercial Ultem) is a thermoplastic polymer with excellent thermal properties ($T_{glass} = 217\text{ }^{\circ}\text{C}$) and low coefficient of thermal expansion, and it is widely employed for aerospace applications. Moreover, it shows excellent fluidity characteristics that makes it a good candidate for injection

moulding, extrusion and foaming, and once dried-powdered it can be combined with functionalized multi-walled carbon nanotubes (MWCNT), as it is possible to see in the schematics in Figure 2.16. Thanks to these functionalization, the experimental behavior in presence of atomic oxygen improves significantly and the resistance to gamma radiation increases thanks to the delocalized π -electrons in the chemical structure [28].

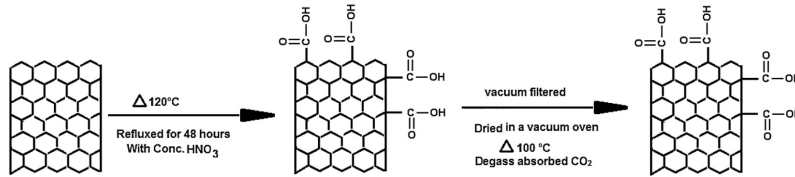


Figure 2.16: MWCNT acidic functionalization [28]

As for metals, also polymers can show some memory effect even if the two concepts are totally different. In the last two decades, shape memory polymers have been widely studied in many different fields such as the biomedical one for drug release, or aerospace technology. Polymers do not show shape-memory effect intrinsically, but this is a result of a combination between their morphology and the processing with which they are functionalized. For example, if a polymer is processed with extruding or injection moulding, it gets to its permanent shape B (Figure 2.17). After processing, there is a programming step during which our part is deformed and fixed in a temporary shape A, and upon application of a stimulus it can recover the B shape (Figure 2.17). The cycle can also be repeated several times, giving different temporary shapes. With respect to SMAs, the cycle of programming and recovery is faster, and polymers allow a higher deformation between the two shapes. Anyways, in both cases the reverse transformation during heating is entropy driven [29].

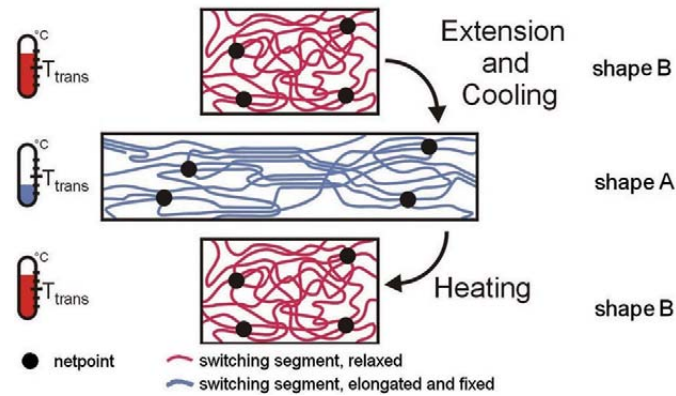


Figure 2.17: Molecular mechanism of the induced shape memory effect [29]

Shape Memory Polymers (SMPs) can be either thermosets or thermoplastics, but they both have some common features such as chemical (covalent bonds) or physical (inter-molecular interactions) cross-linking and stimuli-sensitive switching segments. In general, thermoset polymers are chemically cross-linked, while thermoplastic ones are physically cross-linked and therefore easier to reshape. It is possible to explain the memory effect of SMPs by considering the thermodynamics of the polymer chains. Thermoplastic SMPs are usually block copolymers (at least two segregated domains) in which the dispersed hard phase acts as cross-linking point due to its strongly coiled conformation, and it is related to the highest thermal transition temperature (T_{Perm}). The other domains act as switches, therefore they are called switching segments and are related to the second highest transition temperature (T_{Trans}). When the copolymer is heated at a temperature greater than the glass one for switching domains, they behave as entropic elastomers and can be greatly stretched. After achieving the desired shape, the temperature may be lowered and the chains will stabilize in the new configuration, as in Figure 2.17 [29, 30].

In Figure 2.18, three complete programming cycles of a SMP are shown in different colors, therefore it is possible to see the evolution of strain, stress and temperature during the thermomechanical cyclings and the repeatability of this process [31].

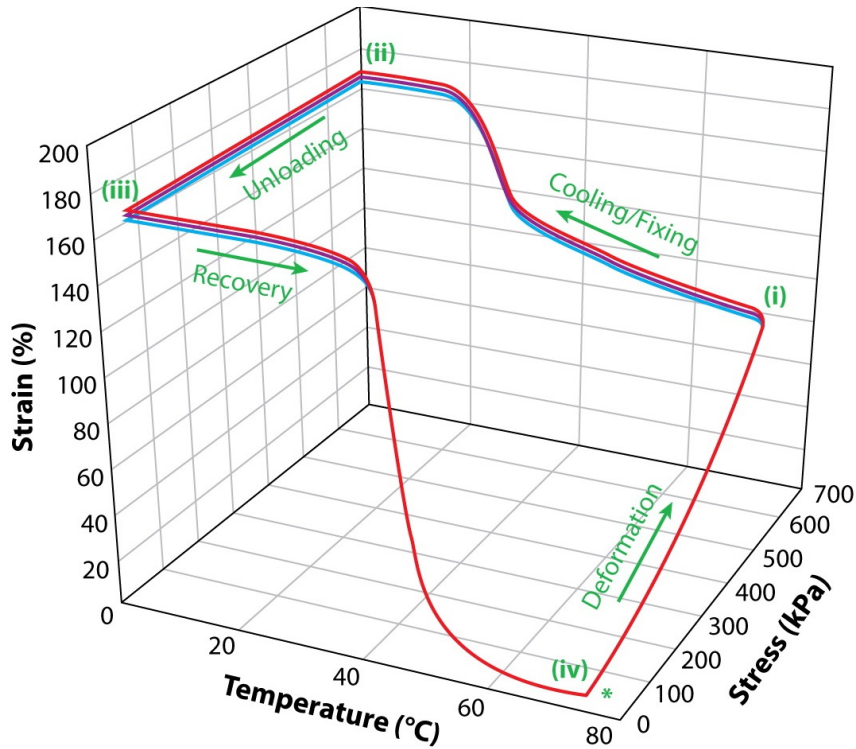


Figure 2.18: Thermodynamics of a SMP system [31]

The two properties that can define the capability of a shape memory polymer to be used in reality are the shape fixing (or fixity) and the shape recovery. The shape fixing is the capability of the polymer to keep a temporary state and store energy while being kept below the transformation temperature. From a thermodynamic point of view, the fixity is the result of a transition between two states, the first one dominated by conformational entropy and the second one by limited mobility of the chains. This quantity can be defined by:

$$R_f = \frac{\epsilon_u}{\epsilon_m}, \quad (2.1)$$

where ϵ_u refers to the strain after unloading and ϵ_m to the temporary strain after the deformation. R_f is dependent on the number of loading cycles and on the way the constituent chains of the polymer has been designed (e.g. when they vitrify or crystallize at a given temperature).

On the other hand, the shape recovery is the evolution of stress and strain over time and temperature. Free recovery is recovery without the application of a me-

chanical load, and it is widely used to characterize the usability of a shape memory polymer. The most common expression of the shape recovery is defined in:

$$R_r = \frac{\epsilon_u - \epsilon_p}{\epsilon_m - \epsilon_p}, \quad (2.2)$$

where ϵ_u , ϵ_p and ϵ_m are respectively the strains after unloading, heat-induced recovery and temporary after deformation.

In 2008, NASA developed a composite truss structure that could be folded exceeding a 11:1 ratio. The material used is a shape memory composite made of a charged thermoset resin; at room temperature the composite has traditional properties and can support itself and potential loads, but above T_g the matrix becomes flexible as an elastomer and the structure can be compressed axially. In figure 2.19 the activation sequence is shown, and it takes approximately a minute to full deploy; the truss structure goes from a minimum of 6 cm to more than 72 cm in the deployed configuration. This concept has been tested on several prototypes and it has been demonstrated to be repeatable [32].



Figure 2.19: Deployment mechanism of a truss structure [32]

2.3 3D Printing

Additive Manufacturing is a widespread technique that was born in the 1980s and developed rapidly in the last decade; by definition, it is the “process of joining materials to make parts from 3D model data, usually layer upon layer, as opposed to subtractive manufacturing and formative manufacturing methodologies” (ISO/ASTM

52900:2015 [33]). Among the different techniques in this family there are Fused Deposition Modelling (FDM) and Material Jetting (MJ), which are of relevant importance for this thesis.

In the late 1980s, the company Stratasys started to develop Fused Deposition Modelling, a process that involves a polymeric fused filament to be deposited on a substrate or platform, by means of a moving head. The working mechanism is very easy, and it consists in using the solid polymer filament as a piston inside the hot-end (the element in the machine that allows melting) in order to push the melted polymer down the nozzle and towards the substrate. This process is schematised in Figure 2.20.

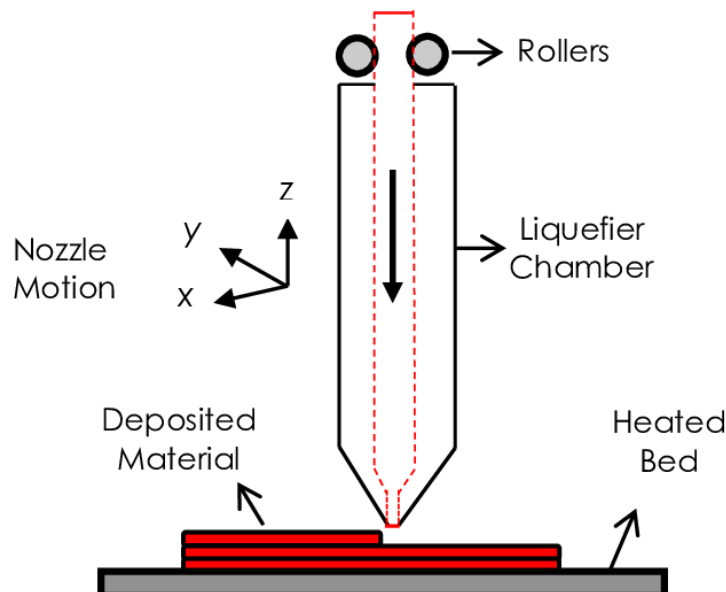


Figure 2.20: Basics of FDM Printing [34]

The fast cooling after deposition allows building multiple layers one upon each other; the most common configuration consists of moving extruder in the XY plane while the substrate moves along Z. To limit shrinking, it is possible to have a heated substrate in order to slow the cooling down and not to have residual stresses in the printed parts. Nowadays there are cheap printers on the market which produce very precise parts without need for post-processing operations (such as surface smoothing).

Starting from 1988, FDM technology developed, and nowadays it is possible to have multi-material printers exploiting the same working mechanism. In this way, it is possible to have parts made with different colours or to print with the help of a support material which can be easily removed by means of a solution; in this case, the limitations related to the overhangs of some objects can be overcome, as shown in Figure 2.21.



Figure 2.21: Part with overhangs [35]

This is the case of the uPrint commercial 3D printer developed by Stratasys (Figure 2.22), which was used in this work to print some of the prototypes; the support material used in this printer is called F123 QSR (commercial name) and directly conveyed by Stratasys.



Figure 2.22: uPrint SE Plus 3D Printer by Stratasys [36]

Another printer used for manufacturing was the Connex3 by Stratasys; this printer exploits the principle of multi-jetting common for normal inkjet paper printers, but in this case layers of liquid photopolymer are jetted on the build tray and polymerize instantly thanks to UV light.

The printer is very precise (resolution down to 16 μm in High Quality mode), and the printed parts are exceptionally smooth in comparison with traditional FDM printers; to print parts with overhangs it uses a support material (SUP705 or SUP706) that can be removed with rinsing using an appropriate solvent followed by waterjet blasting using the postprocessing station provided by the machine producer. Another important feature is the range of materials offered, from structural polymers to rubber-like ones and to bio-compatible options. The printer is said to be multi-material since it has four nozzles and can extrude up to three different materials or colours, along with the support material chosen. In Figure 2.23, it is possible to see how the printer looks like.



Figure 2.23: Connex3 Object500 3D Printer by Stratasys [37]

The last printer used was an Ultimaker 2, a FDM low-cost commercial printer by Ultimaker equipped with a single nozzle. With respect to the other two printers described, the surface finish is clearly lower, but the prints are fast and this is the ideal solution for fast prototyping when no support structures are needed.

2.4 4D Printing

In 2013, a collaboration between MIT and Stratasys Ltd gave birth to 4D Printing. Skylar Tibbit, head of the Self-Assembly Lab at the Massachusetts Institute of Technology is considered as the father of this new technique; by using the printing ability of 3D printers by Stratasys, he developed structures that could be actuated and changing their shape in time. For this reason, the equation defining this new additive manufacturing technique will be:

$$4D \text{ Printing} = 3D \text{ Printing} + \text{time} \quad (2.3)$$

meaning that a printed part can transform over time after a stimulus is applied, emphasizing that printed structures are not anymore static objects. In fact, they become programmable and active and can transform independently. Smart structures are then created without need for post-processing, allowing to save time, money and extra components; this technique could be the first step into evolvable structure able to adapt to needs or to the environment [3].

2.4.1 Printers and preliminary works

To achieve 4D printed parts, there is the need to employ shape memory polymers in 3D printers and design proper structures to be programmed after the print. Many 3D printing technologies are available for the print of SMPs, such as Fused Deposition Modelling (FDM), Stereolithography (SLA) and Material Jetting (MJ).

Regarding FDM, some experiment for the feasibility of the process are described and achieved good results. During FDM printing, the material extruded is heated above T_g and subsequently deposited on the platform or on adjacent layers; by moving, the extrusion head partially stretches the extruded material. At the end, the printed layer bonds with existing layers and it cools down and gets solid again. This process is similar to the SMP thermomechanical programming described in Paragraph 2.2.2, therefore this concept is exploited to print pre-strained 2D structures that would transform into 3D complex structures by strain recovery heating. To

prove the concept, Hu et al. [38] used a polyurethane-based filament in a FlashForge New Creator Pro 3D printer, and several samples of each geometry were printed to prove the repeatability. In Figure 2.24 it is possible to see the printed samples in comparison with their FE modelling.

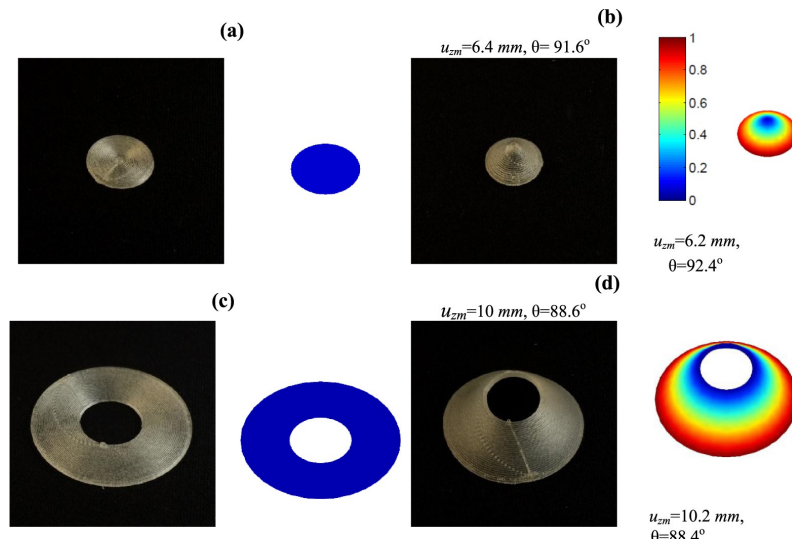


Figure 2.24: FDM-Printed active parts [38]

Chapter 3

Materials' study

One of the main concern in space applications is represented by the harsh environment the component will have to face. Since the early 1970s, a variety of tests and studies has been conducted both on Earth and subsequently in the real space environment in many different missions, such as the ones conducted on the International Space Station (ISS), which is the ideal platform for long-term experiments.

The main treats the materials are exposed to include solar ultraviolet radiation, vacuum, aggressive reactants, thermal cycling and extreme temperatures, impact with debris and many other phenomena. Therefore, many parameters have to be considered to assure that the mission will not fail; these include orbital parameters, the solar cycle and some possible solar event.

In this chapter, the material requirements for facing the space environmental effects are analyzed using the database embedded in the commercial software CES EduPack. This is done in order to carry out a preliminary survey for selecting possible candidates for the antenna.

3.1 Space requirements

3.1.1 Vacuum

The main problem related with vacuum is the outgassing of materials, i.e. the release of volatiles. In space, vacuum pressure is between 1×10^{-3} Pa to 1×10^{-6} Pa. Outgassing is particularly dangerous because not only it can deteriorate the material, but the outgassed particles can also affect sensible parts of the vehicle such as optical and reflecting parts (solar panels, sensors). To solve this problem, in NASA SPP 30426 there are all the limits for molecular deposition, densities and release of particulates. NASA also has a database with all the results from the Standard Test Method for Total Mass Loss and Collected Volatile Condensable Materials from Outgassing in a Vacuum Environment [39]. If a material is known to outgas, it can be treated with thermal vacuum baking for a minimum of 24 hours at a temperature greater than the one it will encounter in space (typically 150 °C) [4].

Different materials have different reactions to vacuum; regarding polymers, thermoset and reinforced ones do not have remarkable issues with outgassing, since they are relatively stable, and their properties are not significantly affected. The things are different for elastomers and thermoplastic polymers, because outgassing first affects volatile additives and therefore the properties that were stabilized by those can degrade (increase in rigidity when plasticisers are lost). Generally, metals do not show particular problems in vacuum [40].

In the standard ASTM E595 there is a description of the test to perform on the material chosen, and on the requirements to fulfill. Two different parameters are measured, the Total Mass Lost (TML) and the Collected Volatile Condensable Materials (CVCM); the test consists in the evaluation of these quantities after the samples are kept for 24 hours at a temperature of 30 °C higher than the expected operating temperature and at a pressure below 7×10^{-3} Pa. A drawing of the test equipment is shown in Figure 3.1 [39].

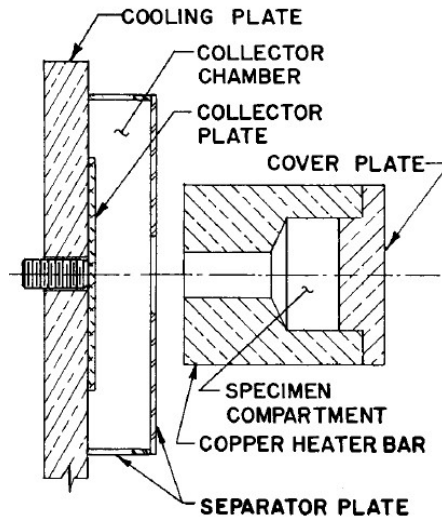


Figure 3.1: Outgassing in vacuum - Test equipment [39]

3.1.2 Atomic Oxygen

In the low Earth orbit (LEO) environment, atomic oxygen (AO) is the most significant component for materials degradation; in fact, at this altitude the solar radiation is able to break the diatomic oxygen bond. This specie reacts strongly with materials, and an evidence was found in the Space Shuttle mission during the glow phenomenon, as seen in Figure 3.2 [41].

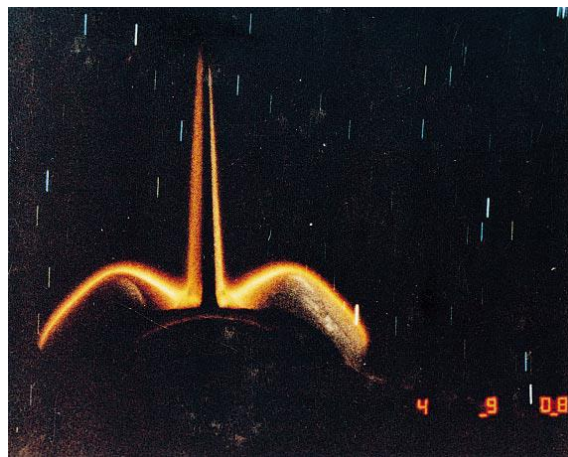


Figure 3.2: Shuttle glow phenomenon [41]

To determine the AO reactivity of materials, it is possible to test them with an experiment known as erosion yield, which implies a long exposure time for the

erosion to occur. Nowadays, also some software for simulation have been developed to determine whether the sample thickness is enough for the particular experiment, such as the Mass Spectrometer Incoherent Scatter model (MSIS). A drawback of the erosion yield test is that to create AO, laser detonation or microwave sources need to be used; if the polymers tested contain fluorine, they will be more sensitive to the UV generated with AO and the test will result in a higher reactivity with respect to the one in orbit. For this reason, laboratory results are compared with flight results of known materials, such as polyimide, polyethylene and polypropylene. The Standard Practices for Ground Laboratory Atomic Oxygen Interaction Evaluation of Materials for Space Applications [42] can therefore produce variable results [4, 43].

Polymers are generally affected by atomic oxygen; thermoset plastics are eroded, therefore some fragment of material are released in the environment and can cause secondary damages. Thermoplastics are mainly used in films and their damage could be severe due to their low thickness. Short fibres composites are also affected by AO, since resin usually etches quicker than fibres and fragments of these can be easily released. To overcome the polymer durability issue different strategies can be applied; one consists in the use of coatings made of silicon oxides (SiO_x) or indium tin oxide (ITO), even though sometimes there are undercut problems and the layer can be easily detached. Another possibility is the implantation of inert metal particles on the polymer surface to reduce the reactance and to make them more durable [2, 40].

Atomic oxygen reacts also with many metals, such as silver, copper or osmium. To prevent problems, their use is not considered in spacecraft parts which operates in direct contact with the LEO atmosphere [40].

3.1.3 Ultraviolet Radiation

Ultraviolet (UV) radiation is defined by ISO 21348 as the portion of radiation spectrum between 10 and 400 nm [16]. This radiation has enough energy to break organic bonds, such as C-C and C-O, as seen in Figure 3.3 [6].

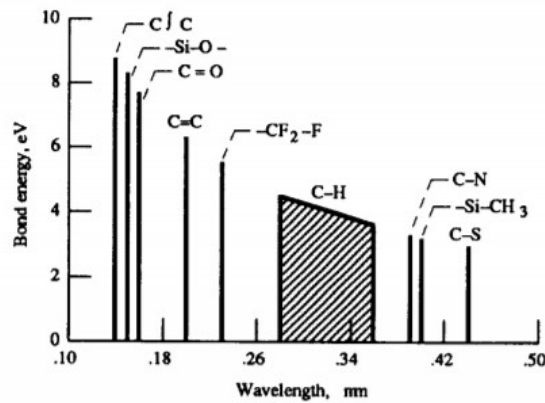


Figure 3.3: Organic bonds wavelength [6]

The UV testing for space applications can be done by using a proper lamp and by keeping the samples exposed long enough in vacuum atmosphere; the comparison of ground testing with flight results is affected by the type of lamp used and therefore some considerations are needed from time to time. Accelerated UV testing are not advisable, since the samples warm up because of the radiation, and the final accuracy could be affected [4].

As already said, this radiation is particularly dangerous for polymers, because it can harden them by cross-linking or weaken them by chain scission. In particular, both elastomers and thermoplastics are heavily damaged; the latter are usually more sensible if fluorinated and shall not be used in full exposure. Anyway, since UV damage is limited to surface layers, it can be disregarded if the device does not have optical importance. For this reason, thin thermoplastic polymeric layers are prone to discoloration, embrittlement and deformation and shall not be used [40].

On the other hand, thermoset polymers and metals are not significantly affected by UV radiation in LEO environment [40].

3.1.4 Thermal effects

Temperature is another important parameter to take into account for a structure in the LEO environment; in fact, the object in orbit will be subjected to continuous

thermal cycling that depends on its view of the sun and Earth, on the time in sunlight and shadow and on its thermo-optical properties, such as solar absorbance and thermal emittance. Therefore, it is important that the material selected can withstand the whole range of temperatures and that the structure can keep its mechanical properties at all times; usually, as a rule of thumb, a cyclic temperature between -125 and 125 °C is considered with about 16 revolution periods per day. Further information about this procedure can be found in the appropriate standard (ECSS-Q-ST-70-04C [44]).

To assure a preliminary screening of materials, a thermal vacuum testing (TVAC) is generally performed, to demonstrate that the components will be able to survive in the space environment, both in vacuum and at extreme temperatures; physical and mechanical properties are examined both before after the cycling and eventually compared and analyzed. To perform this test, several approaches have resulted in the development of cheap and custom chambers, such as the one built by Torralba and Aranda [5]. They designed a cubic chamber able to reach and keep high vacuum conditions (down to 10^{-3} Pa) and low temperatures (down to -180 °C). The scheme to obtain high vacuum is shown in Figure 3.4; as it is possible to see, two different pumps in series are necessary to reach this level.

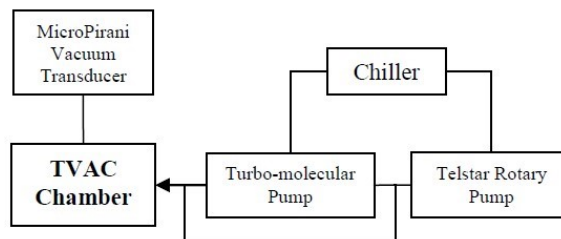


Figure 3.4: Vacuum system block diagram [5]

With respect to thermal events, every material class shows a peculiar behavior with respect to the magnitude and effect of contraction/expansion cycles. Thermoset polymers are quite stable in LEO but temperature variation represents the highest risk since thermal cycling can lead to crack formations and, in the long term, overall loss of properties. Same thing is also valid for reinforced thermoset composites,

with a higher insurgence of cracks due to the different expansions along different directions (anisotropy). Thermoplastics used in films soften with high temperatures and this can lead to degradation, and also at low temperatures their performance is bad since they become brittle below their T_{glass} .

To try to protect polymeric materials from the severe temperatures, various coatings were studied on the ISS, but the severe cycling (16 per day) leads to cracking and peeling which allows the atomic oxygen to act on the substrate, as seen in Figure 3.5 [4].



Figure 3.5: Coatings' failure related to thermal cycling and AO erosion [4]

For metals, problems with temperature control are similar to the ones encountered in other technologies, but in space the difficulties are linked to the opportunity to achieve a good thermal contact in the absence of air and thus convective cooling.

3.1.5 Debris

Micrometeoroids can travel up to 60 km/s and space debris up to 10 km/s, therefore materials might be severely damaged by the high-speed impacts. As the sun activity increases, the drag of debris in orbit increases accordingly; most of the impacts studied with experiments on the ISS were small, producing craters with a diameter smaller than 0.5 mm, as reported by Finckenor and de Groh [4]. In Figure 3.6, a crater created by a micrometeoroid is shown; the coating has been detached by the impact, but luckily it affected only a small portion of the sample.

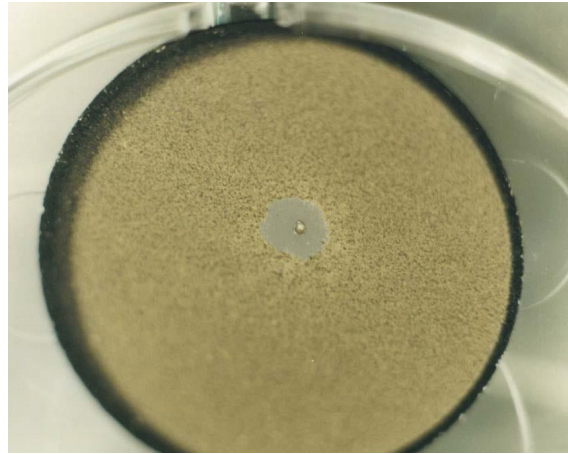


Figure 3.6: Crater created by a micrometeoroid [4]

The problem of debris is increasing in time, since many satellites and spacecraft can fragmentate or even collide in LEO; for example, in 2009 the collision between Iridium 33 and Cosmos 2251 satellite increased by 60 % the number of trackable debris and the untraceable one increased by more than 200 000 as reported by Finckenor and de Groh [4].

Every material is affected by this issue, metals can undergo plastic deformation and composite delamination phenomena. High energy impacts of large masses can cause catastrophic failures and erosion; the effects of impacts are unpredictable and shall be reviewed case by case [40].

3.1.6 Summary and discussion

As discussed, the low Earth orbit environment is harsh, and to some extent represents a problem for every category of materials. Experiments on the ground are still far away from simulating all the issues of the LEO environment all together, therefore data from NASA and ESA experiments on the ISS or on other missions are strongly advisable; for this purpose, a complete database on tested material (Materials And Processes Technical Information System - MAPTIS) is available online [45].

In Table 3.1, a preliminary summary of all the issues analyzed is shown, with marks given from ++ (best) to - (worst).

Table 3.1: Materials' issues in space

	Outgassing	AO	UV	Thermal	Debris	Overall
Metals	++	++	++	++	-	Stable
Thermoset	+	+	+	+	-	Stable
Thermoplastics	+/-	+/-	+/-	+/-	-	Depends

3.2 Material comparison based on CES EduPack database

Besides the NASA database, there is a commercially available software able to give a first screening on materials for specific applications. Of course, more detailed information needs to be obtained on a case-by-case basis using data sheet or specifically-designed test, focusing on the most promising materials. Clearly, this goes beyond the scope of the current thesis work, which focuses on the antenna design with the available materials for 4D printing.

The software used is CES EduPack by Granta Design, and it is based on the pioneering work of Professor Mike Ashby, father of the homonymous diagrams (Figure 3.7).

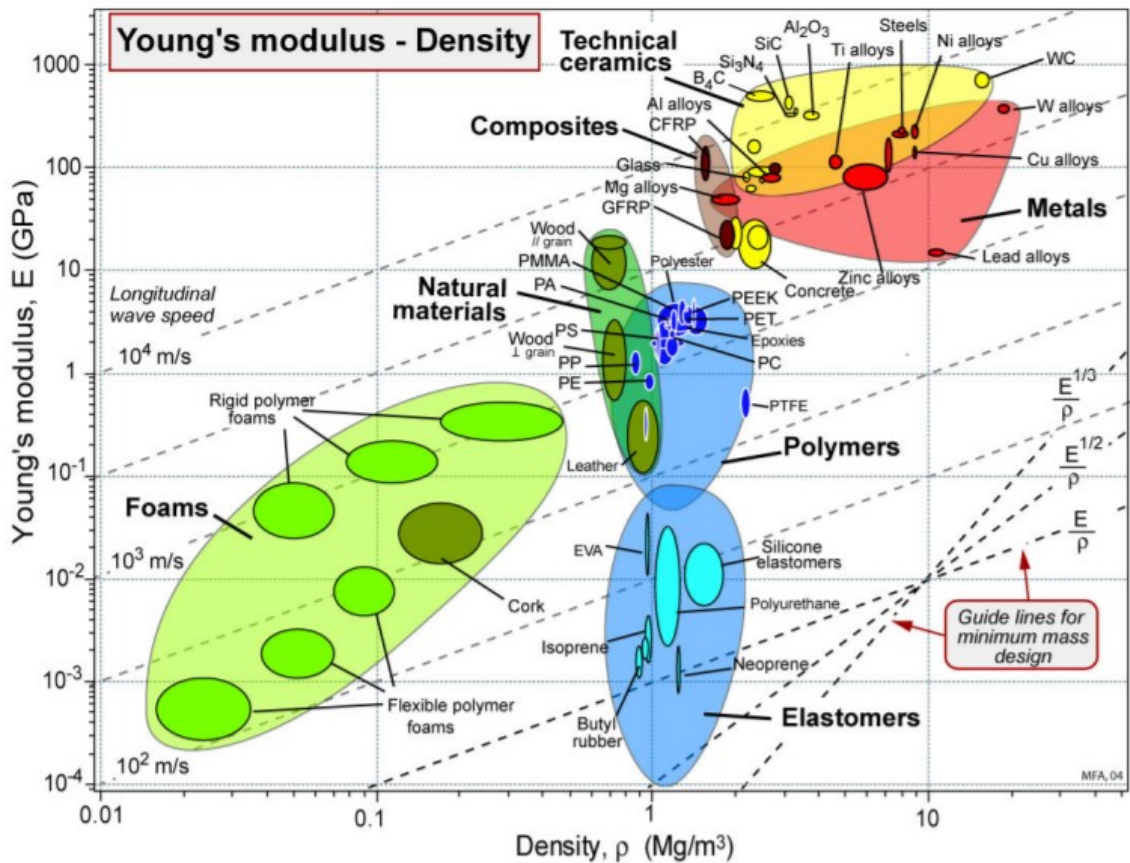


Figure 3.7: Ashby chart - Young's modulus vs. Density

Ashby charts can display a variety of properties on the axis, and it is possible to select different subset of materials with a property within a specified range. Right now, the number of materials available for comparison exceeds 3900, with a wide range of mechanical, physical and economic properties.

In the following subsections, a study on different properties is shown. Since the antenna will need to sustain itself and have a certain structural stiffness, the graphs consider the Young's modulus as discriminant in the selection process. The minimum threshold chosen for this thesis was 1 GPa, in order to ensure a stiff and lightweight structure.

3.2.1 Polymers

Since the goal of this project is to 3D print the final version of the antenna, only pure polymeric material classes are taken into account in this analysis for comparison. The first parameter to be considered is the Glass Temperature with respect to the Young's modulus. At this stage, all the materials with a T_{glass} over 150°C and Young's modulus greater than 1 GPa were selected to assure continuity in the properties during space thermal cycling (Figure 3.8).

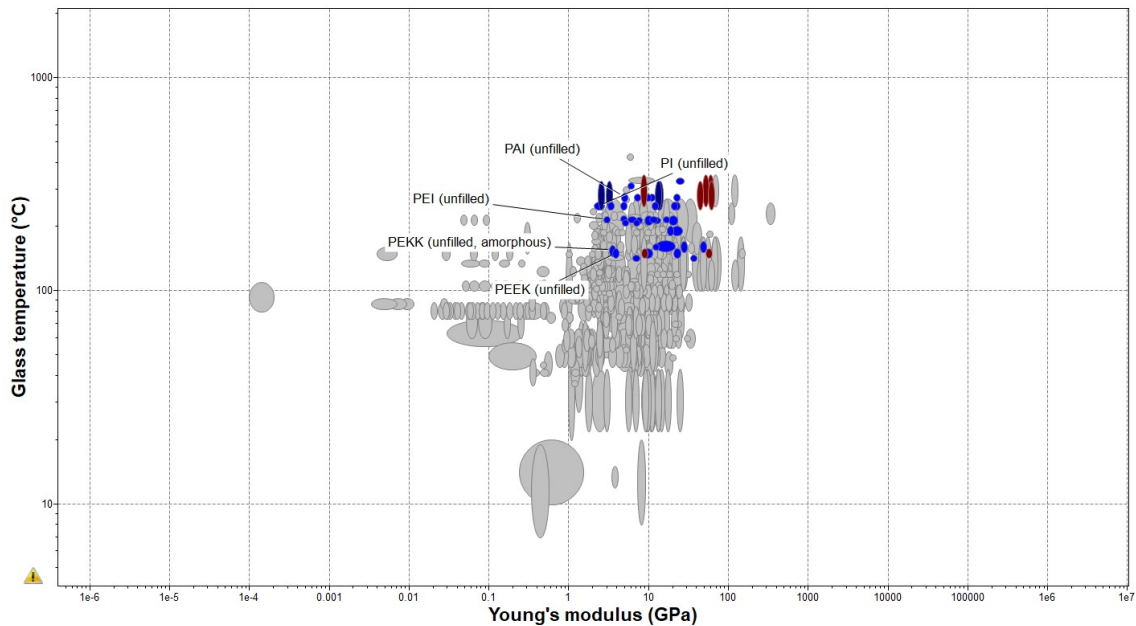


Figure 3.8: Polymers' T_{glass} vs. Young's modulus

The second Figure (Figure 3.9) represents the resistance to UV solar radiation; again, this is measured on ground for application in the Earth's atmosphere, but it is reasonable to suppose that if a polymer is already performing bad on Earth, it would perform even worse in the LEO environment. For this reason, the UV radiation threshold was set at "excellent" while the Young's modulus again greater than 1 GPa.

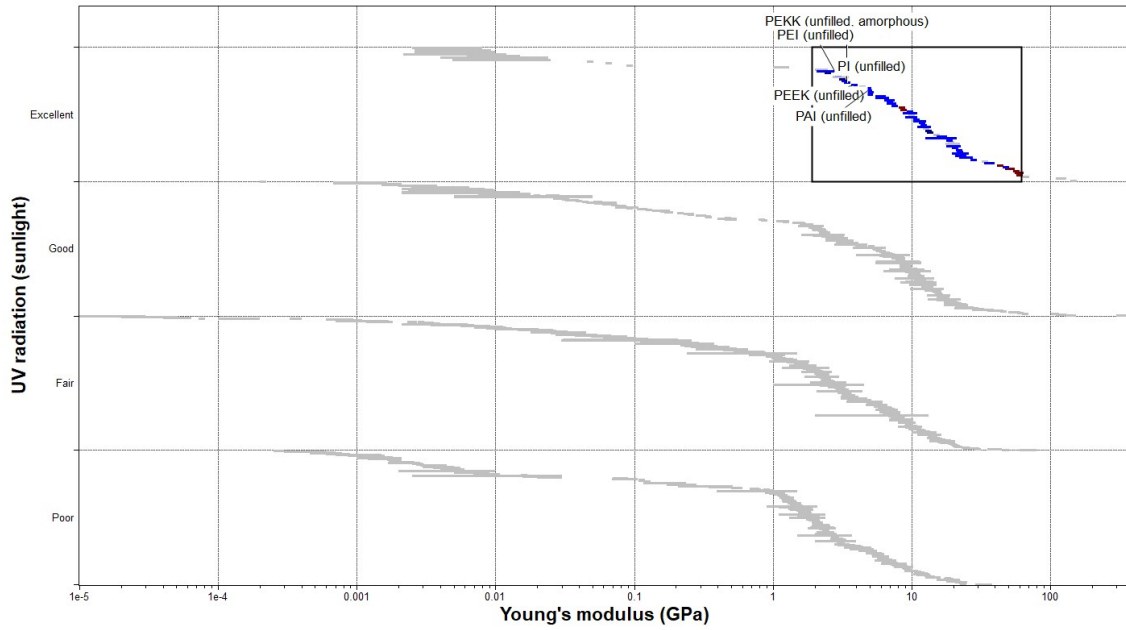


Figure 3.9: Polymers' Resistance to solar radiation vs. Young's Modulus

Regarding temperatures, it was worth to see the maximum service temperature for the different material classes, and again a minimum limit of 150 °C was set to play safe (Figure 3.10).



Figure 3.10: Polymers' Maximum service temperature

The material classes which are highlighted in the graphs above are the ones

that successfully got through all of the limits in the three runs. As we can see, the families which are there are PEEK (Polyether ether ketone), PEKK (Polyether ketone ketone), PI (Polyimide), PAI (Polyamide imide) and PEI (Polyethylenimine).

3.2.2 Metals

For metals the discussion is different, because many of them have good mechanical properties and can withstand thermal cycling and harsh temperatures if compared with polymers. It is interesting to create a plot with the Young's modulus in function of the density, since the density of metals is greater than the one of polymers. The Ashby chart representing this characteristic is therefore shown in Figure 3.11. The different colors in the plot simply represent different metal alloys (e.g. black for Ni-Ti alloys). In this case also, the minimum value of 1 GPa was set as reference.

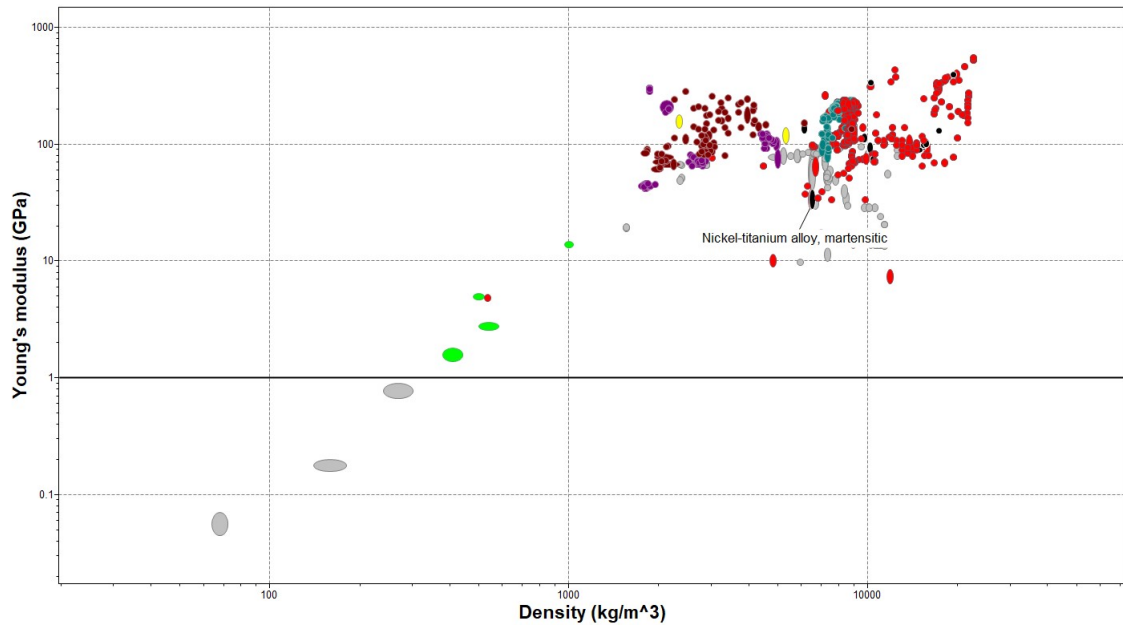


Figure 3.11: Metals' Young's modulus vs. Density

Moreover, a graph with the maximum service temperature is also created, setting as a low limit the minimum temperature of 150 °C, as for polymers; the graph is shown in Figure 3.12.

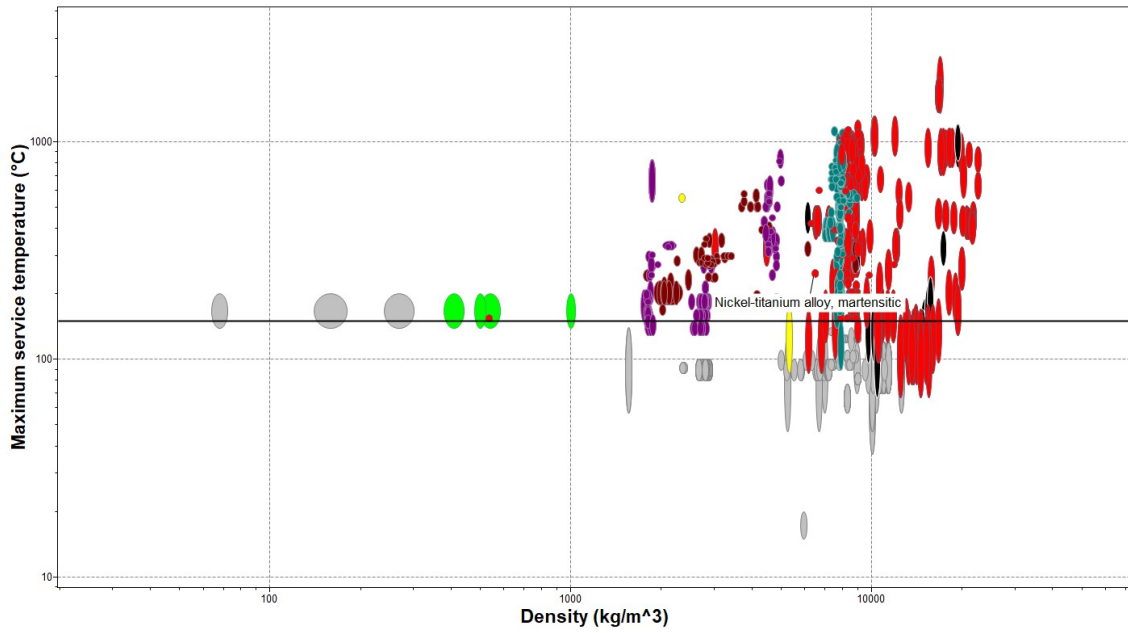


Figure 3.12: Metals' Maximum service temperature

At this point, a graph representing the resistance to UV solar radiation on Earth is shown in Figure 3.13; as it is possible to see, any metal in the database shows an excellent behaviour, therefore this cannot be used as a discriminant in the decision process.

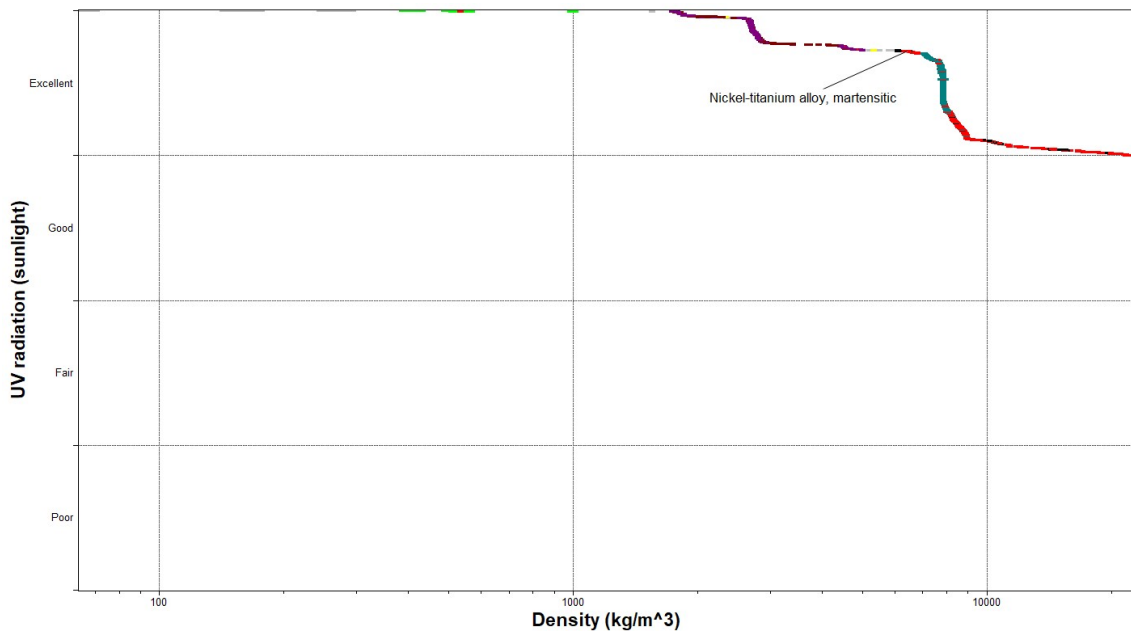


Figure 3.13: Metals' Radiation resistance vs. Density

With respect to polymers, it is extremely difficult to understand which metal to consider, because more than 1500 out of 1800 passed the three stages analyzed on CES EduPack; unluckily, the software still does not have a library with Shape Memory Alloys, therefore in the graphs a Ni-Ti alloy was highlighted for reference.

A table to summarize all the properties is shown in the next page.

Table 3.2: Summary of different materials' classes

	General		Testing										Requirements	
	Material family	E [GPa]	UTS [MPa]	Density [g cm ⁻³]	Temperature range [°C]	Space Thermal Cycling [-150 to +150 °C]	HDT @1.8MPa [°C]	Vacuum Outgassing TML [%]	AO	Radiation resistance	Moisture absorption 24h [%]	Space tested	3D printable	SME
Standard(s)	ASTM D638 ASTM E111	ASTM D638 ASTM E111	ASTM D792											
Thermoplastics	PEEK	3.8	87-95	1.31	-60 +250		139-182	low	etch	excellent	0.1-0.14	N	FDM/SLS	VESTAKEEP@ L4000G (P9)
	PEK	3.8	112-124	1.3	-37 +200		175-247	low	etch	good	0.09-0.11	N	FDM/SLS	
	PEKK	4.4	98-108	1.27	Tg 149		166-184	low	etch	excellent	0.27-0.33	Y	FDM/SLS	
	PAI	5.8	38-42	1.43	-180 +211		250-307	low	etch	excellent	0.31-0.36	N	-	
	PEI	3	73-81	1.27	-30 +170		197-200	low	etch	excellent	0.23-0.28	N	FDM	
Thermoset	PI	2.4	86-89	1.37	-250 +260	Y	274-330	low	etch	excellent		Y	DIW	[P6]
Metals	Mg alloys	45	150-180	1.8-2	-270 +170			high	etch	excellent			Only coated	
	Ni-Ti								etch	excellent		Y		

Table 3.3: Properties of commercially available polymers for space applications

	General			Testing						Requirements	
	Commercial name	Material producer	E [GPa]	UTS [MPa]	Density [g cm ⁻³]	Temperature range [°C]	Space Thermal Cycling [-150 to +150 °C]	HDT @1.8MPa [°C]	Vacuum Outgassing TML [%]		Moisture absorption 24h [%]
Standard(s)			ASTM D638 ASTM E111	ASTM D638 ASTM E111	ASTM D792			ASTM D648	ASTM E595	ASTM D5229	3D printable
Used in space	Windform XT2.0	CRP Technology	8.9	84	1.097	Tg at 80	ok	173	-	-	SLS
	Antero	Stratasys	3.1	93	1.27	Tg at 149	ok	147	0.27	-	FDM
	Kapton HIN	Dupont	2.5	231	1.42	-270 to +400	ok	-	-	2%	DIW
	Accura Bluestone	3D-Systems	7.7-12	68	1.78	Tg at 78	ok	66	-	-	SLA

3.3 Final choice

The characteristics that the perfect material should have are schematized in Figure 3.14; unluckily, it is very difficult to select an available material which has all of these, since they are very specific and at some point also in contrast with each other.

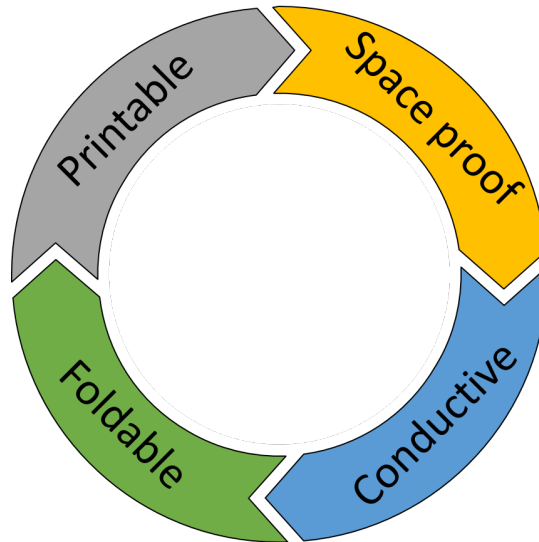


Figure 3.14: Antenna requirements

The final target of this thesis is to produce a prototype which can be the precursor of a functioning antenna; for this reason, since the cheapest and most common printers are developed for polymers, metals will be disregarded. Probably in the future these latter are going to play a big role, but unfortunately the 4D printing process for them is not yet developed. As seen in the Chapter 2, one of the most promising shape memory alloys for aerospace application is the Nitinol (Nickel - Tin intermetallic); as stated by Wang et al. [7], Khoo et al. [8], the Selective Laser Melting (SLM) process would be the best one to 4D print Nitinol and exploit its shape memory behaviour. Unluckily, the authors recognize that this process needs still time to develop to optimize the printer parameters, since at the moment the final properties' of the part are different from the bulk material (e.g. process-induced porosity, austenitic crystals orientation etc.), leading to inhomogeneous. However, this topic has been widely studied in the last few years, therefore there is a good

chance that the process will be soon developed.

Regarding polymers, the conductive characteristic is disregarded, since it is already very difficult to satisfy the other three criteria selected. Taking into consideration both the different classes of polymers (Table 3.2) and the commercially available ones (Table 3.3), the best choice would be to pick a material already certified from NASA or ESA.

Being powder bed fusion of polymers available since many year, it has now reached a state of maturity that allows semi-industrial production of high-temperature plastics such as polyetherarylketones (PEK is the most common) or engineering polymers such as polyamides (PA12 is the most common). For example, Selective Laser Sintering offers commercially available materials such as Windform XT 2.0 [9], already certified by NASA for space applications.

Nevertheless, 4D printing of polymers is still nowadays limited to a handful of polymers, mainly acrylic resins. This makes the development of new materials capable of withstanding the space harsh conditions and being at the same time 4D printable paramount. It is clear that the scope of this thesis is focused on the development of a deployable structure and not on materials development, and for this reason the final choice for the current work is VeroWhite+ and Agilus (description follows in Section 5.3), two materials available for the Polyjet process from Stratasys.

Clearly, parts produced with these materials are not satisfying the requirements for space introduced in the previous paragraphs, but a PEEK powder coating applied with spraying could probably provide enough protection to allow survivability of the part even in space.

Chapter 4

Antenna selection

At the beginning of this chapter, an overview of the antenna physical characteristics and parameters relevant for the project's follow up are explored. Afterwards, the criteria for the selection of the antenna for the ETH CubeSat are selected and analysed. Thanks to this defined parameters, finally it will be possible to choose the optimal type of antenna for this project.

4.1 Introduction

In 1886, the professor Heinrich Hertz started to study electromagnetic forces relation with dielectric polarization and built an apparatus that we would define as a complete radio system, with a dipole antenna as emitter and a resonant square loop antenna as receiver, as seen in Figure 4.1. This invention was kept in Hertz' laboratory up to the day in which Guglielmo Marconi repeated his experiments and added tuning and ground systems to Hertz' radio.

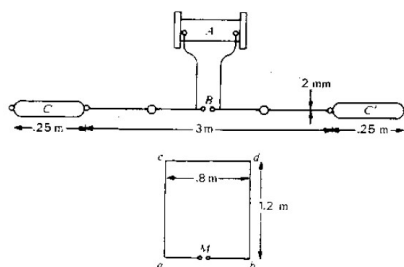


Figure 4.1: Hertz first radio [46]

At the end of 1901, Marconi announced that he had received signals from across the Atlantic ocean, but the scientific establishment did not believe him since radio waves should travel in straight lines as light does. However, Marconi was believed by the Cable Company which had the monopoly in transatlantic communications, and therefore was asked to desist. He persisted, and a couple of months after the first transmission, he gave proof of the functioning of the experiment by recording several Morse signals coming from England on a tape on the SS Philadelphia (traveling from Cherbourg to New York). From that moment on, a lot of experiments and improvements on the antenna started, together with the advent of telecommunication industry [46].

An antenna is the relation between electric currents flowing in conductors and radio waves propagating in space; it can be used both in transmission or reception, depending on whether the antenna radiates energy from a current as electromagnetic waves or the other way around. Therefore, an antenna is built as an array of conducting elements connected to the transmitting or the receiving element.

If the antenna is used in receiving mode, an analogy with the human eye can be made, since they both collect electromagnetic photons and translate them into electric currents.

4.2 Antenna characteristics

In this section, the parameters needed to describe an antenna are explained.

4.2.1 Key specification: radiation pattern, coverage and gain

The radiation pattern is a graphical representation of the antenna radiation properties as a function of space coordinates; a typical example can be seen in Figure 4.2.

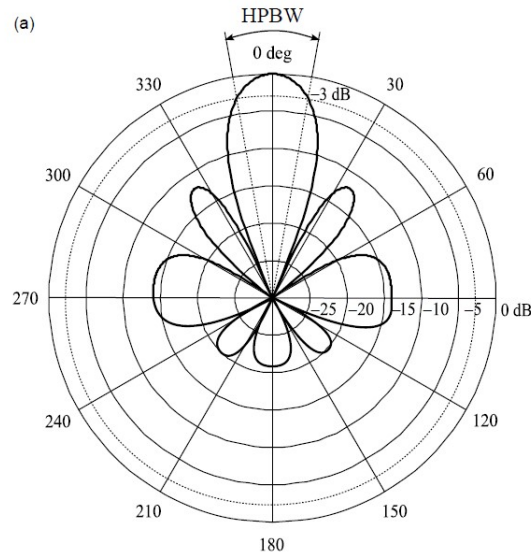


Figure 4.2: Radiation pattern [2]

Usually, this pattern is determined in the far-field region because the angular field distribution becomes independent of the distance from a point in the antenna region, according to:

$$|d| > \frac{2D^2}{\lambda} \quad (4.1)$$

where d is the distance from the antenna, λ the free-space wavelength of the antenna and D the maximum overall dimension of the antenna.

This pattern is defined as the radiated electric field $\mathbf{E}(r)$ at a great distance and it is equal to the product of the pattern function (depending on direction) $\mathbf{P}(\mathbf{a}_r)$ and an exponential term which depends on the length of the position vector d , originating in the antenna coordinate systems:

$$\lim_{x \rightarrow \infty} \mathbf{E}(r) = \mathbf{P}(\mathbf{a}_r) \frac{e^{-jkr}}{d} \quad (4.2)$$

In Figure 4.2, it is possible to see how the lobe directed towards the 0-degree direction results bigger than the others; this lobe takes the name of Main Lobe and it is relevant for directional antennas, since it represents the maximum of the radiation intensity. Therefore, in these antennas it is important to enhance this lobe in order

to have a stronger signal along the main direction. Another parameter called Half-Power Beam Width (HPBW) is shown in Figure 4.3, which magnifies the main lobe of the radiation pattern. HPBW is defined as the angle between the two directions in which the radiation intensity is half of its maximum value. Another important parameter is the coverage, i.e. range of transmission or reception directions over which some antenna parameters (gain, directivity) meet certain specifications.

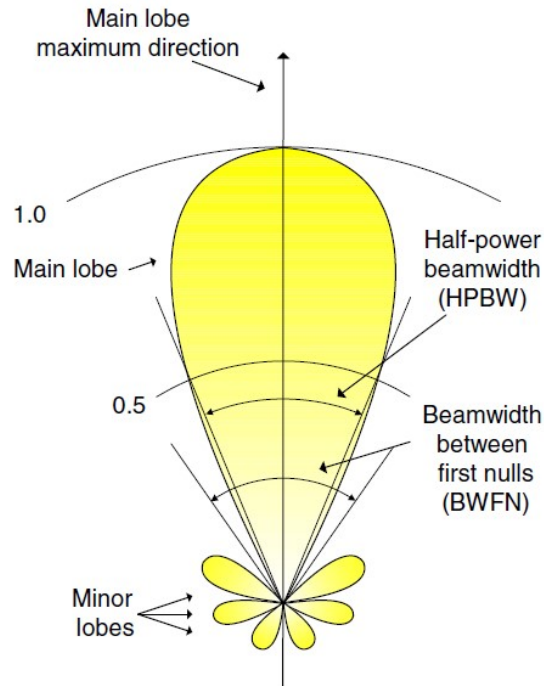


Figure 4.3: Half-Power Beam Width (HPBW) [47]

The gain in a given direction is described by Equation 4.3:

$$g \equiv \frac{U}{\frac{P_{acc}}{4\pi}} = \frac{2\pi|\mathbf{P}|^2}{\eta_0 P_{acc}} \quad (4.3)$$

where P_{acc} is the accepted power in input and \mathbf{P} the pattern function. Therefore, the gain is the ratio between the radiation intensity on the average radiation intensity over the radiation sphere, with the assumption that all the power is radiated isotropically (in contrast with the radiation pattern shown in Figure 4.2).

For an antenna which radiates all the power accepted, the gain will be maximum, and it will be equal to the directivity (described in the next paragraph).

$$e_{cd} \equiv \frac{G}{D} \quad (4.4)$$

4.2.2 Antenna design for spacecrafts: polarization and directivity

In antennas for satellites, it is very important to define the polarization and the directivity of the signal, since these quantities assure the correct functioning and monitoring from the Earth. This is particularly critical for CubeSats, in which the transmitting power is not very high and thus the antenna design plays a critical role in the quality of the signal that goes back to Earth. This topic will be further explored in Section 4.3.2.

In fact, the antenna polarization gives the polarization of the plane wave transmitted or received by the far field for a given direction, as shown in Figure 4.4. It can be linear (Figure 4.4(a)), if the electric field is directed along a line; this is the ideal case, because all antennas generate electromagnetic waves with both co- and cross-polarization fields, in which the oscillation direction of the electric field vector describes an ellipsoid in 3 dimensions (Figure 4.4(c)). In case of a circular polarization, the ellipse axes are equal (Figure 4.4(b)); this polarization is common for antennas used on satellites and missiles, since their orientation cannot be controlled from time to time (alignment issues).

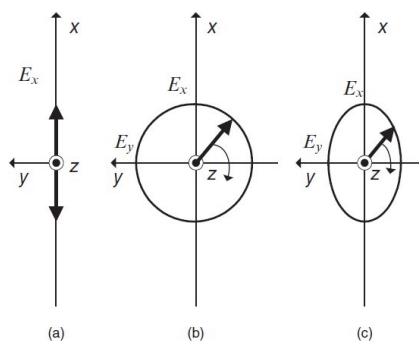


Figure 4.4: Polarization of a wave [47]

Polarization can be described through the polarization-phase vector, which rep-

resents both the polarization and the phase of the radiated field:

$$\mathbf{p} \equiv \frac{\mathbf{P}}{|\mathbf{P}|} \text{ with } |\mathbf{P}| = \sqrt{\mathbf{P} \cdot \mathbf{P}^*} \quad (4.5)$$

with \mathbf{p} polarization vector and \mathbf{P} pattern function. Instead, the directivity indicates how well the radiated power is concentrated into a solid angle, and therefore it is a function of the ratio of the far field radiation intensity in a given direction to the average radiation intensity (radiated power per solid angle), as shown in Equation 4.6:

$$D \equiv \frac{4\pi U}{P_{rad}} = \frac{2\pi |\mathbf{P}|^2}{\eta_0 \cdot P_{rad}} = \frac{4\pi |\mathbf{P}|^2}{\int_{4\pi} |\mathbf{P}|^2 d\Omega} \quad (4.6)$$

Since the directivity is proportional to polarization, it is important to notice that also in this case it can be defined a co- and cross- directivity, depending on the type of polarization it is used in the formula.

4.3 Antenna for ETH CubeSat

Nowadays, the CubeSat project involves over a hundred universities, high schools and private companies developing satellites for many purposes (scientific, private, government); the sharing of information is at the basis of the project, and the community is growing fast.

4.3.1 Requirements and restrictions

At the beginning of this thesis project, some parameters were defined to explore all the different antenna types and make the right decision in terms of functionality. Moreover, since the antenna will be inserted in a CubeSat and will have to emit in the Ultra High Frequency range (UHF), limitations in dimensions exist.

The critical parameters for the antenna type selection are the volume of the stowing compartment, the mass and the operating frequency. The operational temperature has already been analysed in Chapter 3 and the deployed stiffness will have a relevant importance during the design phase in Chapter 5.

Regarding dimensional requirements, on the CubeSat official website it is possible to find all the specifications and a check list to verify the compliance of the satellite before sending it in orbit; in Figure 4.5, there is an extract from the original CubeSat specification file [1].

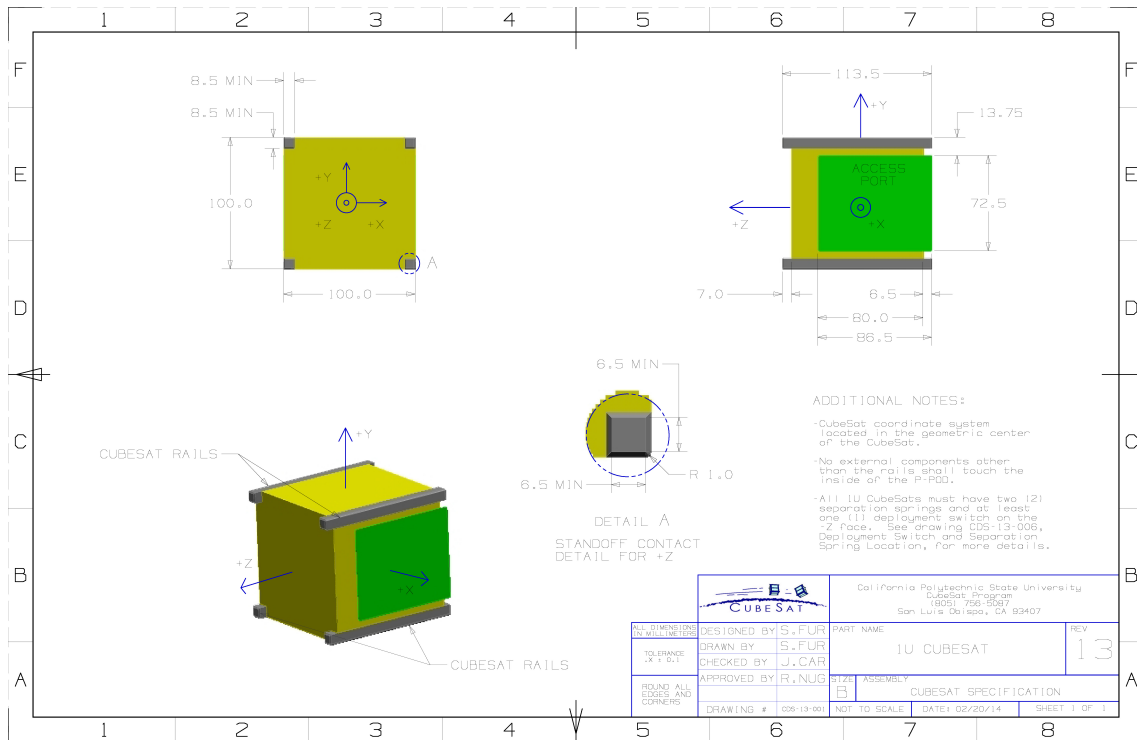


Figure 4.5: CubeSat specifications [1]

Since the purpose of this thesis is to develop an innovative active mechanism for the deployment of an antenna from a CubeSat, an initial antenna dimension of $95 \times 95 \times 95 \text{ mm}^3$ was set. The requirements for the project were discussed within the research group to assure a correct functioning of the antenna and the fit in the stowed compartment of the CubeSat, and a summary is highlighted in Table 4.1.

Table 4.1: Antenna's project requirements

Requirements	
Stowing compartment	95 x 95 x 95 mm ³
Mass	< 400 g
Operating frequency	300 MHz to 3000 MHz
Minimum antenna gain	> 10 dBi
Polarization	Circular
Deployed stiffness	> 1 Hz
Operational temperature	-120 °C to 120 °C
Manufacturing chamber volume	490 x 390 x 200 mm ³

with dBi the forward gain of an antenna compared with an isotropic one, assuming linear polarization of the EM field. Moreover, the stiffness is given in Hz as reported in private document shared with the partner company of this thesis project. Finally, the manufacturing chamber volume is the total internal size of the 3D printer.

All these parameters were analyzed to understand which antenna type could best satisfy dimensional, functional and deployment requirements. Since the challenge of the project is to use 4D printing to manufacture the prototype and in future the real functioning antenna, another requirement is the ability to be printed.

4.3.2 Overview of possible designs

The antennas that were considered in this thesis work were the dipole, the microstrip (patch), the conical log-spiral (CLS), the helix with single and multiple branches, the parabolic reflector and the horn ones.

Regarding the dimensional and foldability requirements, in 2017 a study was performed at California Institute of Technology on different antennas by Sakovsky et al. [48]. All the antenna types analysed are foldable with different wrapping schemes, as seen in Table 4.2.

Table 4.2: Folding mechanisms for different antennas [48]

	Hinge	Tape spring	Helical pantograph	Z-folded shells	Miura-Ori shells	Coilable conductors	Hinged ribs	Wrapped mesh
Dipole	X	X						
Helix			X	X	X	X		
CLS				X	X			
Horn				X	X			
Patch								
Reflector							X	X

In Table 4.2, many different mechanisms are reported. The hinge folding system refers to the simple folding through hinges of a dipole antenna along the edges of the CubeSat; for these antennas also the tape spring configuration is available.

Regarding helical antennas, a pantograph-type folding is available, and it is developed by means of a cylindrical supporting lattice structure kept together by scissor joints, as already seen in Figure 2.9. Another way to fold the helical branches would be to apply a momentum and a force and to coil them down in the CubeSat, and therefore exploiting the mechanical properties of spring elements during the unfolding stage.

Both the Z-folded and Miura-Ori shells involve the use of origami patterns applied to a composite foil, in which the areas along folds (hinges) are made of an elastomeric material in order not to damage the conductive stiffer parts. The Z-folded implies a folding along one direction only, instead the Miura-Ori scheme allows folding in two directions.

Parabolic reflector antennas are composed by a curved main dish, therefore it is possible to design some structural ribs which could be folded thanks to hinges; alternatively, the ribs can be designed as elastic and wrapped along the central hub with an origami scheme.

As stated by Le et al. [49], patch antennas are generally small and do not require folding; the maximum was found by these authors at a diameter of 60 mm, which would fit in the CubeSat.

After considering foldability, that was not helpful as a discriminant, the antenna polarization was taken into account; as already said, for satellite antennas it is important to have a circular polarization, since they are emitting from space and there is the need of receiving a clean signal from different relative positions of the satellite and Earth. Therefore, at this point it was possible to exclude from the list the dipole antenna, since it can only have a linear polarization.

Now, gain is taken into account; in fact, a minimum of 10 dBi gain is prescribed for the antenna to be manufactured in this project. As studied from Le et al. [49], for microstrip antenna a circular polarization might be possible, but the gain would be still too low in the UHF range to be considered as a relevant option. For the other antenna types this requirement can be achieved, therefore there is the necessity to analyze the other prescribed parameters.

At this point, dimensioning is considered; in particular, the dimensions of an antenna are strictly related to the working frequency range. If we consider parabolic reflectors, it is easy to notice that they can be very powerful (as seen in Section 2.1.4); usually, they are employed for emitting at lower frequency since it is easy to design them in big dimensions and to fold them. Unfortunately, for applications in a CubeSat where the space is very limited they do not represent the best choice.

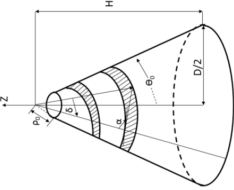
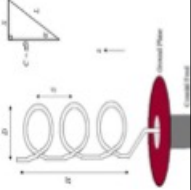
Regarding the CLS antenna, Olson et al. [17] reports that is very difficult to prescribe the dimensions according to the desired frequency range, and that the

process is fully experimental and iterative and thus takes a long time. Moreover, these antennas often work with a ground plane to ensure a good value of gain, and this would occupy a larger space in the CubeSat small volume. Since there are other easier options, this type of antenna is also disregarded.

An overview of the antenna types described in Section 4.3.2 is summarized in the following Table 4.3.

At this point, it is clear that only the helix and the horn antenna are left from the initial list. Although both of them satisfy the requirements studied up to now, the helix antenna seems to provide the best compromise among flexibility, hindrance and operating frequency required for this application. In particular, a quadrifilar helix antenna will be designed in Chapter 5 and (mechanically) evaluated in Chapter 6.

Table 4.3: Types of antennas

Antenna type	Properties							
	Polarization	Ground plane	Gain	Directivity	Frequency peak	Foldability	Dimensions	Mass
Half-Wavelength Dipole 	Linear	No	3 dB to 5 dBi	-	Single frequency peak	Yes	$h = \frac{\lambda}{2}$	*Linear polarization, not good for this application
Patch 	Linear	Yes	6 dB to 7 dBi	Can be achieved	Broadband	Yes	$\{0.003\lambda < t < 0.05\lambda\}$ \cap $\{\frac{\lambda}{3} < h < \frac{\lambda}{2}\}$	*Linear polarization, not good for this application
Conical Log Spiral 	Circular	Can have it (bottom fed configuration)	up to 10 dBi	High	Broadband (UHF band ok)	Yes	The dimensions are interpolated from experimental data (no design equations available) [J. D. Dyson]	Experimental work needed
Monofilar Helix 	Circular	Yes	10 dB to 17 dBi (dependent on ground plane size)	High	Single frequency peak	Yes	$H = N * S$ $L = \sqrt{S^2 + (2\pi R)^2}$	Depending on ground plane

Antenna type	Properties							
	Polarization	Ground plane	Gain	Directivity	Frequency peak	Foldability	Dimensions	Mass
Quadrifilar Helix 	Circular	Can have it	10 dB to 17 dBi	High	Single frequency peak	Yes	The dimensions are interpolated from experimental data (no design equations available)	300 g
Parabolic Reflector 	Various	No	up to 20 dB to 30 dBi	High	Broadband	Yes	$\{0.65 < \epsilon_{sp} < 0.80\}$ \cap $\{2\lambda < D < 50\lambda\}$	High dimension high mass
Conical Horn 	Linear / Circular	Can have it	10 dB to 20 dBi	Medium	Broadband	Yes	$\{2^\circ < 2\theta < 45^\circ\}$ \cap $\{45^\circ < \alpha < 90^\circ\}$	
	Strongly dependent on frequency and dimensions							
	Notes:							

Chapter 5

Antenna design and manufacturing

In the previous chapter, a choice on the antenna type was made; the quadrifilar helix design has a circular base, therefore it is necessary to find a shape capable of sustaining the conductive coil.

In this chapter, after the dimensions of the helical antenna with respect to the emitting frequency range are studied, two designs are considered due to their structural potential and compatibility with the antenna coil geometry, one made by a modular cubic structure that can be repeated along one direction to obtain a long-enough support, the other by a series of counter-facing helix' branches. In the next chapter, the two best prototypes (one for each design family) will be analysed.

5.1 Modeling of helix antenna design

In the design of a helical antenna there are some geometrical parameters to consider: they will be analyzed in the following sections, that includes a MATLAB script for predicting the dimensions as a function of the desired receiving frequencies.

5.1.1 Equations

These parameters, such as the number of revolutions (N), the radius of the base around which the branches are revolved (r) and the height (h), are related to the frequency (f) emitted by the antenna [50].

$$f = \frac{c}{\sqrt{\frac{h^2}{N^2} + (2\pi r)^2}} \quad (5.1)$$

where c is the speed of light.

5.1.2 Dimensional analysis

A script was created to numerically compute different sets of parameters (N, r, h, f) in order to quantitatively ascertain the best combination for the preliminary antenna design as a function of the requirements introduced in Section 4.3. In particular, the script allows the user to obtain all the sets of values which are suitable for having emission at that given wavelength $\lambda = \frac{c}{f}$ for different N values. The results for the set of parameters introduced in Table 5.1 are reported in Figure 5.1:

Table 5.1: Parameters for theoretical calculations

Parameter	Value
Height h	0 mm to 1000 mm
Radius r	25 mm to 50 mm
Number of turns N	3 to 25

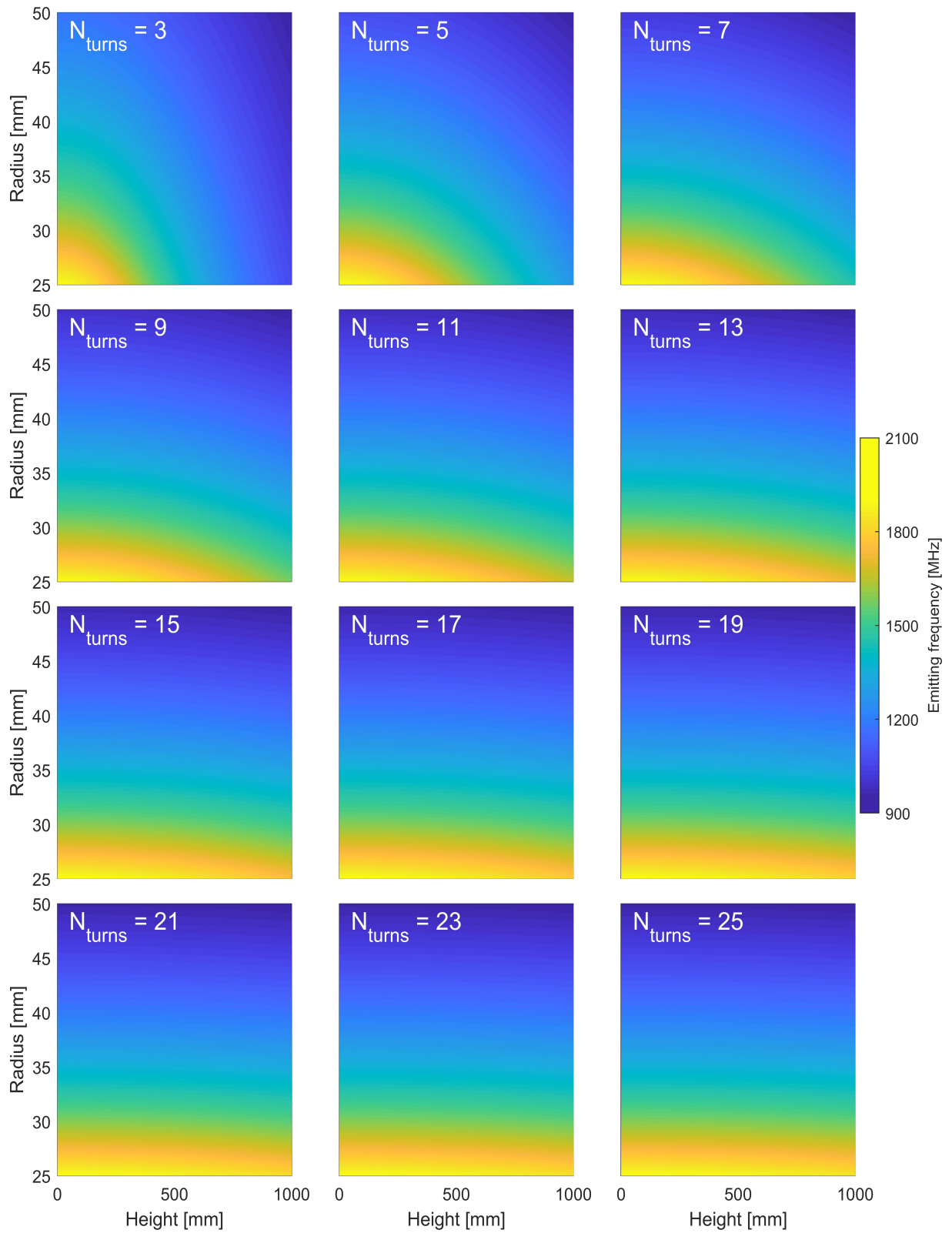


Figure 5.1: Numerical evaluation of Equation 5.1

As it is possible to notice, all the frequencies presented in Figure 5.1 lie within the UHF range (300 MHz to 3000 MHz).

A further analysis has been carried out by selecting 4 frequencies (1000, 1200, 1500, 1900 MHz) inside the UHF band, and plotting the combination of r , h and N that allowed to obtain those receiving frequencies. The results are shown in Figure 5.2:

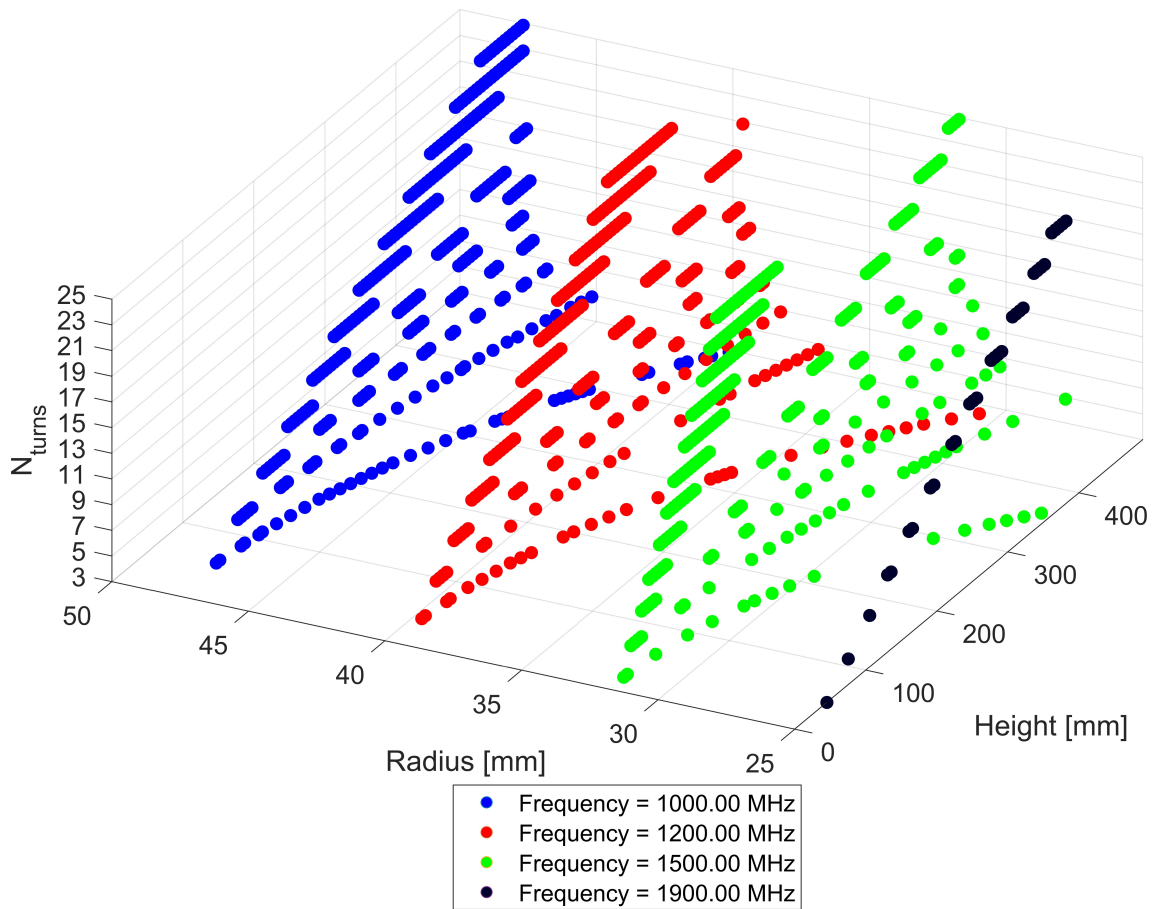


Figure 5.2: Numerical evaluation of design parameters for several frequencies

The selection rules for the three design parameters can be then introduced:

- N should be as low as possible, in order to maximize the sectional diameter of the “wire” that constitutes the antenna (manufacturing limitation) and to reduce the total weight (the lowest number of turns also means the lowest volume occupied in the same height);
- When N is fixed, priority needs to be given to the maximum possible r allowed by the “Stowing compartment” defined in Table 4.1, in order to ensure a stable basis and simplify the manufacturing phase (small r are more difficult to print);
- The ratio between r and h is controlled by the pitch angle of the helix α , shown in Figure 5.3: it is clear that very high angles will lead to an unstable structure, while low angles will lead to bigger undeployed heights. This will lead again to manufacturing problems and violation of the requirement regarding the “Stowing compartment” of the CubeSat.

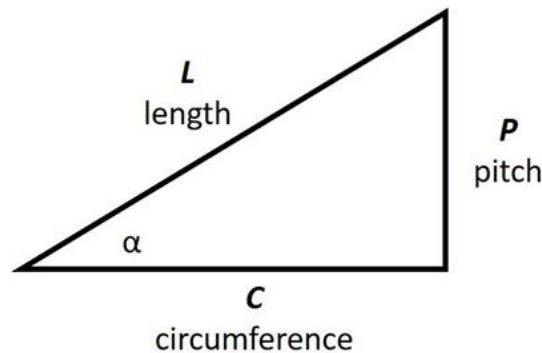


Figure 5.3: Representation of the pitch angle of the helix

with $h = N \cdot P$

Based on these rules, the following ideal combination of the design parameters coming from the numerical solution of Equation 5.1 has been selected, with the best compromise between r and h for $N = 3$, as reported in Table 5.2.

Table 5.2: Best design parameters for helix antenna

Parameters		
Frequency	Height	Radius
MHz	mm	mm
1000	331.66	44.35
1200	311.55	36.19
1500	296.48	27.64
1900	45.22	25

5.2 Cube Modular Structure

Modular structures are very flexible and adaptable to different situations. Since the dimension of the antenna is strictly related to its emitting frequency, it is important to have a structure whose size can be changed at occurrence, for example if the emitting frequency will change in future. In Figure 5.4, it is possible to see an idea of the conductor coils.

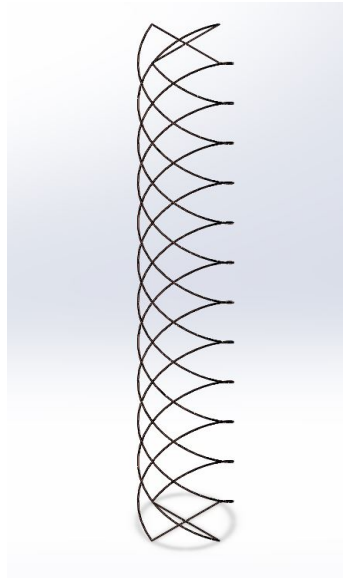


Figure 5.4: Conductor coils

Since there is a need for stiffness, a modular cubic structure is designed; this came from the fact that the coil has a circular section and it is possible to inscribe a square to create a 3D series of modular cubes that can be repeated at occurrence. Therefore, the structure will be inside the coils and these will be fixed to the structure itself through some rings in order to keep the conductive filament in the correct position at all times.

The idea was originated from a similar structure developed in 2018 from Angeletti et al. [51], which used the modular concept for other space applications. This concept is based on Iterative Learning Control applied to repetitive geometry in space, therefore each module has the same deployment trajectory and it is easy to understand the overall final trajectory of the structure.

In Figure 5.5 it is possible to see how the structure is supposed to deploy once in position, thanks to the activation of some joints.

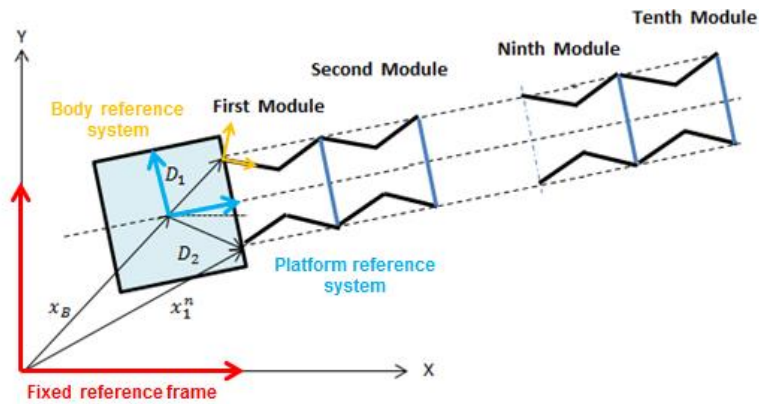


Figure 5.5: Deployment mechanics of a modular structure [51]

Therefore, the final deployed structure should look like Figure 5.6 right, and the one with the conductor like Figure 5.6 left.

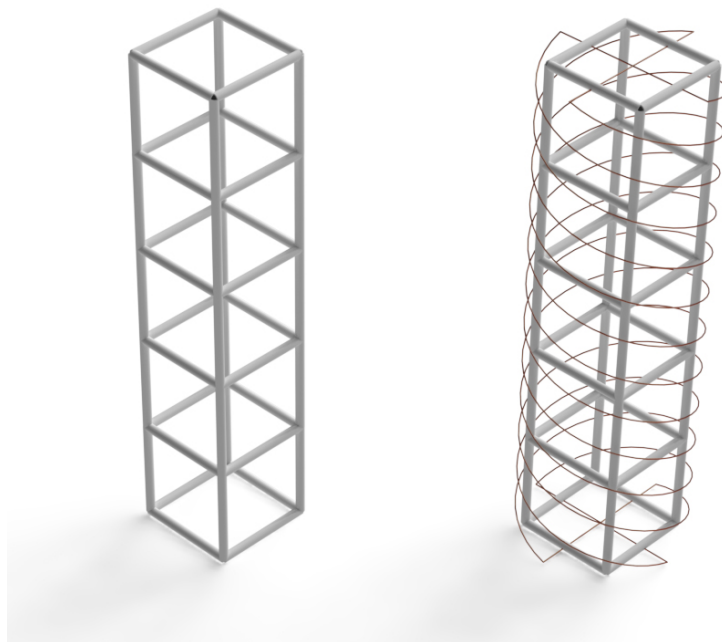


Figure 5.6: Rendering of the preliminary modular structures

5.2.1 First prototype - C1

Since the inspiration came from this idea reported in Figure 5.5, the first studied prototype uses a similar concept. The structure needs to be lightweight in order to pass the weight requirements and needs to be folded in the smallest volume possible. For the latter reason, a series of fixed frames will have to contain the bent branches that will be responsible for the deployment. At this early stage, the opening mechanism is not yet taken into account.

A single-module assembly is composed by 8 half-edges and 2 frames plus connections; the edges can perfectly fit into the frame in order to save space. The final multiple-module folded and deployed structure is shown in Figure 5.7.

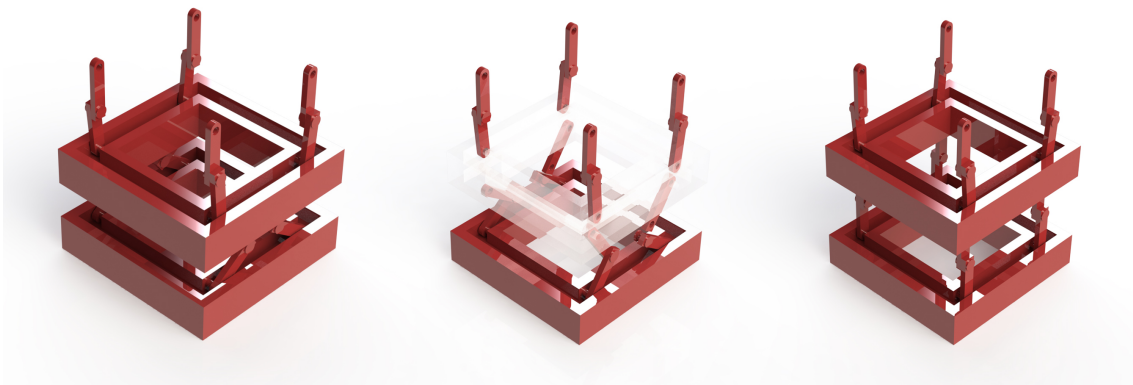


Figure 5.7: Displacement of prototype C1

5.2.2 Second prototype - C2

Since in the previous prototype there was a fundamental problem of deployment caused by the small volume available near the hinges for insertion of active actuation mechanism (e.g. motor), a second prototype was taken into consideration. This time, the idea came from tape springs; in fact, this tape is widely studied thanks to its particular mechanical properties. Tape springs are straight and have a curved cross-section with a thin wall, as seen in Figure 5.8. They can both be folded around a cylinder or in a zig-zag pattern and they show an elastic deformation that can be easily restored [52].



Figure 5.8: Geometry of a tape springs [52]

The problem of tape springs is that their behaviour can be governed by predictive numerical models: Dewalque et al. [53] proved that the mechanical behaviour is mainly governed by the geometry of the tapes. In fact, thanks to the sudden release of energy there is no need of an external impulse to activate the deployment; this could be a problem since the deployment should be controlled, but the idea is to improve one characteristic at the time in order to better focus on the design.

A new prototype was designed in order to apply this deployment approach: the single-unit assembly is composed by a frame (blue component in 5.9), 4 edges (green components in 5.9, glued on the frame) and 4 pieces of measuring tape (not shown, each of them glued onto an edge). The single unit can be repeated up to the desired total height of the antenna while the folding idea is linked to the relative rotation of 90 degrees of the upper over the lower frames.

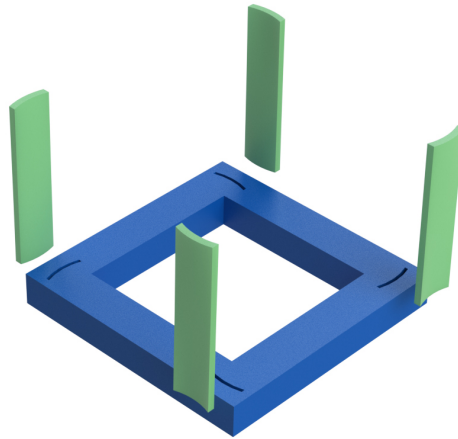


Figure 5.9: Rendering of prototype C2

The first problem in this design came from the difficulty in finding the right curvature to create the holes in the frame, therefore the process was iterative; this is one of the main advantages of using a 3D printer, because it is possible to do a trial and error in a very short time and at low costs.

Regarding manufacturing, the Ultimaker printer described in section 2.3 was used. The parts were manufactured with an ABS filament and the overall dimensions were correct.

Unfortunately, the idea of using small parts of tape spring as hinges was not really working. In fact, the tape spring was too tough to be bent of 90° ; also removing the printed edges and trying to use the tape as edge itself did not solve the problem. Because of this issue, the folding mechanism was redesigned from the beginning in the next prototype.

5.2.3 Third prototype - C3

This is the final design studied for the cube modular idea; since in the last design there was a fundamental problem of buckling because the tape spring had to bend of 90° and it resulted very stiff and difficult to manipulate, the idea was to remove the printed edges and use an available measuring tape itself as the cube edge. Clearly,

in a future multi-material design it would be possible to print together the plastic frame with the metal tape spring.

In the proposed design, the tape spring has been buckled in the way shown in Figure 5.10, in order to only bend the tape once in the ‘tough’ side (red circle in 5.10) and simplify the buckling process, keeping in mind that in a future application there will be more cubes one over the other. Therefore, the “tough” folding happens once for each branch and twice in the “soft” side (green circles in 5.10). When the force keeping the structure folded is released, the structure opens and gains its stiffness back.

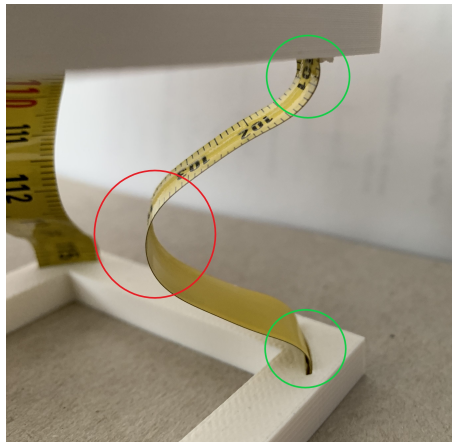


Figure 5.10: Folded tape spring

This prototype was particularly promising, therefore both a single unit and a three-unit modular structure were manufactured, and the final SolidWorks assembly is shown in Figure 5.11.



Figure 5.11: Rendering of prototype C3

As prototype C2, this was also printed with the Ultimaker 2 in ABS; the edge were simply cut from a spring tape and glued to the structure. This solution might not be optimal, but it is very promising since it requires no external forces to be activated.

In Figure 5.12, it is possible to see the final assembled prototype in the deployed state.



Figure 5.12: Prototype C3

5.3 Double Spring System

This second design group was based on the fact that the quadrifilar helix structure is already self-standing if designed with the right parameters, and therefore this same geometry is exploited to give rigidity to the antenna coil. Moreover, the metallic coil could need some protection from the space environment, and it is required to stay in the right position at all time to ensure a good signal stability.

Initially, only one set of quadrifilar helix was considered to allow the protection of the cables and the SolidWorks Part is shown in Figure 5.13, and no possibility of folding was considered. This preliminary idea was manufactured to study the structural stability and to make an approximate estimation of the real stiffness.

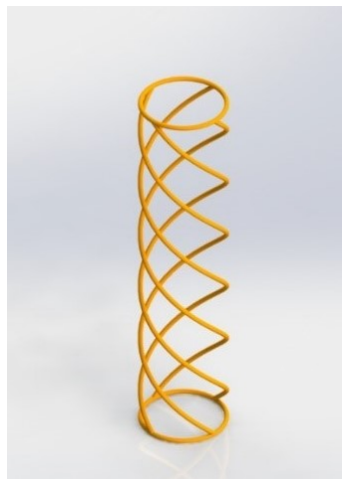


Figure 5.13: Rendering of the preliminary single helix concept

After a first estimation, it was noticed that the structure did not have enough stiffness, therefore the inner counter-clockwise quadrifilar helicoidal structure was designed and printed. In this way, the rigidity was improved, and the structure of the design explored in this section was chosen, see Figure 5.14.



Figure 5.14: Rendering of the preliminary double helix concept

5.3.1 First prototype - H1

The just mentioned idea for enhancing the stiffness is temporarily put on a side to study the structure folding. In fact, this prototype has been designed keeping in mind a future manufacturing technique, such as multi-materials 3D Printing. These printers are capable of printing with stiff and rubber-like polymers to give different properties to the different part of a structure, according to the user needs. At this stage, the structure is designed as an assembly of part that will be manufactured with different machines and put together at the end of the process.

The dimensions of the prototype were defined according to the MATLAB script developed in Section 5.1, by setting an angle of 15° and a number of turn of 2 for simplicity; the rendering of the design is shown in Figure 5.15.



Figure 5.15: Rendering of prototype H1

In this first approach to multi-material printing, only the ‘bases’ of the structure are printed with this printer, to reduce the manufacturing costs and to enhance the speed of the process; therefore, the branches of the helix which did not require any specific gradient in the material properties, were printed in a UPrint Printer from Stratasys, in which they were made by ABS and supported by the F123 QSR support material that was easily removed with the procedure explained in section 2.3. At first, only the clockwise structure has been printed to better understand the result of this initial try.

Regarding the two bases, they were printed with the Connex3; this printer allows to print any geometry, since the parts are totally encapsulated in a support material. In Figure 5.16, it is possible to see the part as it is when it is removed from the printer’s plate; at this point, the support material is mechanically removed with the help of some spatula and wires. The operation can lead to rupture of the black soft material used as connection between the white base ring and the helix branches.



Figure 5.16: Base of prototype H1 as printed

The white material shown in Figure 5.16 is VeroWhite+ (VW+) (rigid behavior) and the black material is Agilus (rubber-like behavior). The former is used to provide stiffness to the structure, while the latter is employed due to its elastomeric (high elongation at break) properties: in fact, the reduction of the pitch angle from the deployed to the undeployed state requires high deformation in that particular region. Their mechanical properties from the official datasheet are shown in Table 5.3.

Table 5.3: Connex3 materials

Mechanical Properties	Agilus ASTM D-412	VeroWhite+ ASTM D-638
Tensile strength	2.4 MPa to 3.1 MPa	50 MPa to 65 MPa
Elongation at break	220 % to 270 %	10 % to 25 %
Young's modulus	-	2 GPa to 3 GPa

The final assembly is shown in Figure 5.17; as it is possible to notice, the structure is not perfectly aligned, and this is due to the fact that there were difficulties in removing the support material from the inside of the black hollow parts. For this reason, the orange branches could not perfectly enter and fit in the designed position; a consequence of the excess of support material is also in the fact that the Agilus broke in several points after some days, making the structure unstable.



Figure 5.17: Prototype H1

Another problem linked to the base is that the interface between VeroWhite+ and Agilus was weak and it partially detached at some points. At this point, it was not clear if the issue was related to the dimensions (there were just few millimetres of material keeping together the two materials) or to the accumulation of support material pushed at the end by the inserted branches, therefore a new prototype was designed.

Given the issues encountered, the counterclockwise structure was no longer manufactured.

5.3.2 Second prototype - H2

The overall dimensions of H1 were increased in order to solve the previous prototype's problem, and to also study the stability of the higher structure. For this purpose, the Table 5.4 with comparison of the dimensions of both H1 and H2 prototypes is shown. As it is possible to see, the connection's outer diameter has been

increased as well in order to make it stronger.

Table 5.4: Dimensional comparison - H1 and H2

Parameter	H1 Measure	H2 Measure
Helix angle	15°	20°
Structure height	101.01 mm	260.26 mm
Structure diameter	60 mm	100 mm
Branch swept diameter	3 mm	3 mm
Base swept diameter	5 mm	6 mm
Connection outer diameter	5 mm	6 mm
Connection inner diameter	3.5 mm	3.5 mm

The final rendering of prototype H2 is shown in Figure 5.18.



Figure 5.18: Rendering of prototype H2

The final manufactured part is shown in Figure 5.19; unfortunately, the detachment problems were not overcome during the manufacturing phase.



Figure 5.19: Prototype H2

In fact, even with larger parts the prototype is very difficult to clean with both mechanical means and chemical dissolution. The conclusion is that the problem encountered in the manufacturing of both H1 and H2 prototypes was due to the final assembly of the parts, since the multi-material printing is accomplished by using a shell of material around every manufactured part (in this case the bases of the structure, as seen previously in Figure 5.16). Another reason could be the design of the interface between the two materials; therefore, both these aspects are explored in the next prototype design.

5.3.3 Third prototype - H3

In this final prototype, the detachment solution is tackled with a redesign of the connections and of the base in general; the target was to have a strong connection between the two materials to eventually avoid detachment. Moreover, this prototype will be manufactured as an entire part in the Connex 3D printer, to finally eliminate the support material problem encountered in H1 and H2 prototypes.

The problem of the old design was in the detachment at the interface, because that is the point which is bending during folding and which is subjected to the higher stresses; for this reason, the base circle was modified in section to add more Agilus material, which has higher elongation at break and thus is expected to minimize this problem. Doing this, the folding will only affect the Agilus material and an additional advantage would be that the interface will not be stressed excessively. The new SolidWorks models are shown in Figure 5.20.



Figure 5.20: Rendering of Agilus and VeroWhite+ parts

Regarding the base circle, the angles are not chamfered because there are no forces applied in this part of the structure and VeroWhite is printed at the same time with Agilus, therefore they have a strong interface in absence of loads. The idea is to expand the rubber-like Agilus to the stiff VeroWhite to avoid detachment; in this way, the stiffness of the structure is not particularly affected. By removing the core of VeroWhite, the circle might bend on itself during the deployment, affecting the stability and functionality of the antenna. In Figure 5.21 the final assembly of the whole base is shown; the two materials are in contact in the red highlighted parts, and this is needed during the production. This time, the prototype is printed as a whole and it is completely encapsulated in the support material, which makes possible the manufacturing of a hollow structure like a helix.



Figure 5.21: Rendering of the assembled base

Figure 5.22 shows the final rendering of the assembly; the counterclockwise structure was the first manufactured, and it has some holes to allow the removal of material and therefore reducing the overall bases weight. This idea came from the fact that the prototype H2 was unbalanced because of heavy bases, even if in this prototype the dimension were reduced again for manufacturing limitations, because the printer volume has a dimension of $490 \times 390 \times 200 \text{ mm}^3$.



Figure 5.22: Rendering of prototype H3

Anyways, the idea of making a hollow structure encountered some problems; removing the material was challenging, and the hole diameter is so small that it is

impossible to clean without the risk of breaking the structure. After this result, a deeper research resulted in some information about the impossibility of using the Connex printer for hollow parts, because of the support material being printed everywhere.

After the failure of the hollow parts idea on the counterclockwise structure, the clockwise one has been printed with a 100% infill. The rest of the design is comparable, with the only differences in the sense of rotation (opposite) and in the dimensions (smaller). In Table 5.5, the design dimensions are presented.

Table 5.5: Dimensions of H3

Parameter	Counterclockwise H3	Clockwise H3
Helix angle	15°	15°
Base diameter	60 mm	49.4 mm
Height	101.01 mm	101.01 mm
Number of turns	2	2
Branch swept diameter	3 mm	3 mm
Base swept diameter	5 mm	5 mm
Connection outer diameter	5 mm	5 mm
Connection inner diameter	3 mm	3 mm

As it is possible to see in Table 5.5, the two structures have been designed with a gap of about 0.5 mm; in a future design, this gap could be reduced or the ground bases could even be printed together, in order to have a perfect alignment and axial symmetry. This cannot be done for the upper bases, since the folding requires a relative rotation of the helical structures, one clockwise and the other in counterclockwise direction.

As already said in the design part, the impossibility of printing hollow parts is a big limitation of the current technology, especially considering the weight saving associated with it. On the other hand, the support material is strongly relevant as a construction mean, otherwise the structure would collapse on itself. In a real device, the best strategy would probably be to obtain a hollow structure and then let a copper cable inside it, in order also to protect it from the space environment and have thus a fully embedded antenna.

Clearly, since the focus of the present thesis work is on the manufacturing and mechanical aspects of the antenna design, in the next chapter some testing will be carried out in order to ascertain the observance of the CubeSat requirements introduced in Table 4.1.

Chapter 6

Testing and results

In this chapter, the testing methodologies for the deployment mechanism of prototypes C3 and H3 are presented, along with the corresponding results. Unfortunately, the materials' palette for 4D printing is not wide enough to produce the prototype C3: nevertheless, it was still assembled and tested.

Tests were carried out on the prototypes for assessing the modes of vibration, since the stiffness of the structure needs to be ascertained once deployed. This is particularly critical, considering that the shape and the geometric dimensions of the antenna are fundamental for ensuring the best emission.

To complete this work, an assessment of the antenna efficiency would be needed: unfortunately, due to the high complexity of the modelling, this topic is currently addressed in the research group by a telecommunication engineer.

6.1 Programming and deployment testing

4D printing is 3D printing with structures that change in time. Of course, to reach this goal a “programming” step is required as introduced in Section 2.2.2. In this thesis, programming occurs thanks to temperature variation, and the activation of the deployment will be again triggered by application of heat. In the following Section 6.1.1, an insight on the programming step will be given, including some theoretical calculations.

6.1.1 Determination of the folding angle

The relative angle β to apply for the folding of the manufactured structure was calculated. As an example, here the calculations are done for prototype H1; the simple test consists in drawing the lower base on a piece of paper and marking the position of one of the upper connection. Consequently, the upper base is rotated and pushed towards the lower base in order to fold the structure; at the end of this operation, the branches are all folded and none of them is surpassing the bases if seen from the top. A second point is marked in correspondence of the final position of the upper connection considered earlier, as seen in Figure 6.1.

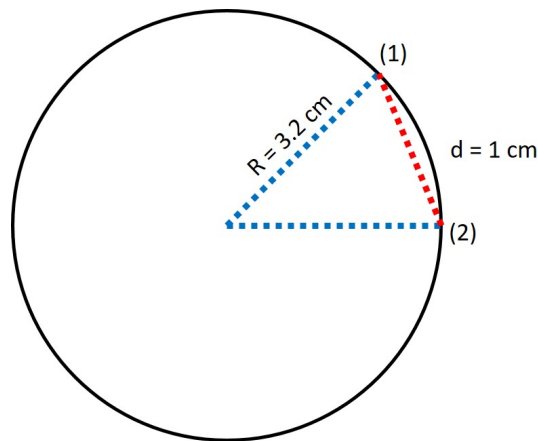


Figure 6.1: Folding angle calculation

From the two marked points (1) and (2) and the radius R of the base it is possible to calculate the rotation angle α it was used to fold the helix. To do so, the linear distance d between the two marked points was measured, and the isosceles triangle

was made in half in order to apply the Pythagoras' theorem and find the unknown rotation angle β .

$$\frac{d}{2} = R \sin \frac{\beta}{2} \quad (6.1)$$

6.1.2 Folding and unfolding of the structure

As already said, this section will take into account the programming step of the 4D Printing process. With 4D Printing the prototype is manufactured with a 3D Printer and a specific shape memory polymer capable of changing its shape when subjected to a stimulus, in this case a temperature change (see Section 2.4).

The two helical structures composing the prototype were first programmed and tested separately; this was done to understand if there was a significant change in the recovery rate of the structures.

In fact, prototype H3 is made of one counterclockwise and one clockwise structure, as seen in Section 5.3.3. In Figure 6.2, it is possible to see the counterclockwise (outer) structure.



Figure 6.2: H3 - Counterclockwise prototype

The programming stage consists of several steps:

- Temperature homogenization at 25 °C for 24 hours;
- Heating up to 70 °C in a water bath;
- Temperature homogenization at 70 °C for 1 minute (Figure 6.3);
- Compression in the axial direction and rotation of β is then applied while wearing high-temperature gloves for 1 minute;
- While keeping normal force and torque roughly constant, the prototype is moved into a cold water bath (20 °C) and kept there for 1 minute;



Figure 6.3: H3 - Counterclockwise prototype inside warm bath

It is very important that both the temporary height before unloading and the fixed height (Figure 6.4 after unloading) are measured correctly, in order to calculate the recovery ratio once the structure will be deployed again.



Figure 6.4: H3 - Counterclockwise prototype in the fixed height state

In order to initiate the re-deployment of the structure, the prototype is immersed in the warm bath again. In Figure 6.5, a comparison between the programmed prototype and the as-manufactured one is shown.

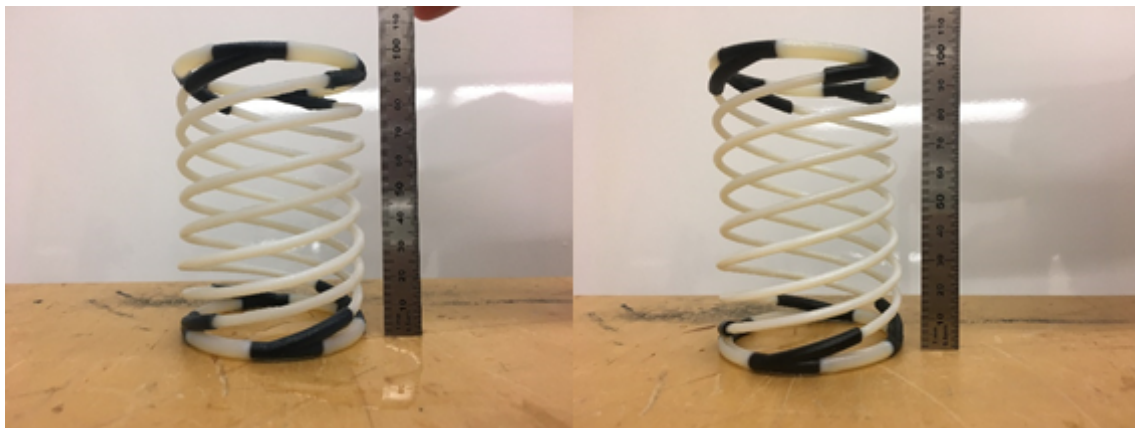


Figure 6.5: H3 - Counterclockwise prototype height comparison

As it is noticed, the programmed prototype (Figure 6.5(left)) did not go back perfectly to its original dimensions, and it is possible to calculate its recovery ratio with Equation 2.2 and reads 90 %.

Now, the entire described procedure used with the counterclockwise structure is repeated with the clockwise part of the prototype (Figure 6.6).



Figure 6.6: H3 - Clockwise prototype inside warm bath

After the cooling in the water bath at 20 °C, the prototype is in its fixed height configuration and it is measured (Figure 6.7).



Figure 6.7: H3 - Clockwise prototype in fixed height state

Now, the prototype is put back in the warm bath and left there for a minute; during this time, the structure gradually stretches and goes back to the original shape. In Figure 6.8, it is possible to see the programmed prototype back to initial state; in this case, the structure recovered unevenly due to some defects in the structure. In fact, the prototype has been printed with the radial symmetry axis perpendicular to the Z axis of the machine: due to a lack of feedstock, the printer

autonomously switched from the “transparent” to the “white” material for finishing about half of the helix.



Figure 6.8: H3 - Clockwise prototype comparison

To calculate the recovery ratio, the medium value between the highest and the lowest point of the upper base was accounted for. This was done because it is reasonable to say that another prototype correctly manufactured with the same material would have a uniform recovery as happened for the prototype folded in counterclockwise direction. The recovery ratio reads in this case 91 %.

Even though it is known that the recovery ratio decreases with increased programming number [30], a last experiment was done with the two parts of the prototype H3. This time, the prototype was programmed as a whole to see if it could recover by sliding together with the other half structure. To do so, the programming procedure was performed once again; the structure was therefore immersed in the warm water bath, as seen in Figure 6.9.

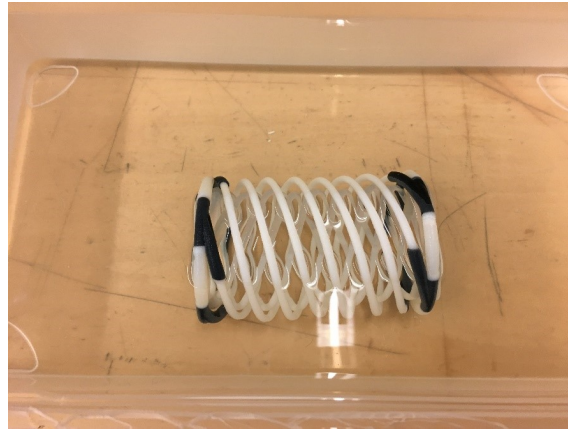


Figure 6.9: H3 - Assembled prototype inside the water bath

Afterwards, the structure was programmed and cooled down in the cold water bath, so as to keep again the new intermediate state. As it is possible to notice in Figure 6.10, the folding of the prototype is perfect, since no branches are seen from the top view. Moreover, in Figure 6.11 it is possible to see the folded and deployed prototype.



Figure 6.10: H3 - Meta-stable prototype top view



Figure 6.11: H3 - Assembled prototype comparison

The recovery ratio results for the three programming experiments are shown in Table 6.1.

Table 6.1: Recovery ratio of H3

	Counterclockwise H3	Clockwise H3	Combined H3
As-manufactured height	10.0 cm	10.0 cm	9.7 cm
Recovered height	9.5 cm	9.9 cm	8.4 cm
Temporary height before unloading	4.5 cm	4.0 cm	4.0 cm
Fixed height after unloading	5.0 cm	4.4 cm	4.5 cm
Shape recovery ratio	90 %	91 %	90 %

Even though the shape recovery ratio is known to decrease with increasing folding/unfolding cycles, the recovery ratio was about 90% in all cases. This is more than enough to ensure a successful deployment of the antenna, which in the real case will need to be unfolded only once, when the CubeSat will reach the orbit.

6.2 Mechanical vibration testing

In this section, a vibration analysis on the unfolded (deployed) C3 and H3 prototypes is performed. First, some simulations on Comsol are run in order to have a first idea of the natural frequency of the prototypes. A known concept of basic mechanics relates natural frequency of an object with its stiffness and mass: requirements from NASA define the minimum natural frequency of 1 Hz. This means that the deployed structure must be stiff enough not to show natural frequencies lower than 1 Hz.

Afterwards, a vibration test is performed on the manufactured prototypes and a final comparison of the results with the simulations is performed. The vibration mode taken into account in the experimental test is the bending one, since it is the most problematic one for a structure with a relatively high aspect ratio.

6.2.1 Comsol models

For the simulation, Comsol V5.3a was used to perform a vibration analysis and find the natural frequencies of the structures accounted for. In this section, an analysis of both the C3 and H3 prototype is performed; moreover, the prototype H3 is also modelled as two parts, the counterclockwise and clockwise helices. This is done as a mean of comparison with the experimental tests on bending frequency and to better understand if the double structure is structurally needed, given the stiffness and weight requirements.

The structures were analyzed, and a study on mesh sensitivity was performed by applying a different number of elements to check if the results were reliable.

The first prototype analyzed was the C3; the bases were modelled as ABS and fixed with an encastre while the spring tape was defined as carbon steel. In Table 6.2, it is possible to see the material parameters that were used; since the vibration analysis takes into account elastic movements around the equilibrium position, only the elastic properties and the density are defined.

Table 6.2: Comsol - Materials' properties for prototype C3

Property class	Property	ABS	Carbon Steel
Density	Mass density	$1.2 \times 10^{-9} \text{ kg mm}^{-3}$	$7.85 \times 10^{-9} \text{ kg mm}^{-3}$
Elastic	Young's modulus	2.5 GPa	210 GPa
Elastic	Poisson's ratio	0.3	0.3

Mesh optimization on C3 design

To ensure the correct meshing of the structure, a mesh optimization was performed, as seen in Figure 6.12; the simulation was therefore repeated multiple times and the goal was to obtain a plateau in the minimum mesh element size vs. (eigen)frequency. In fact, a good final elements simulation is obtained when it is possible to reach a good result with the lowest number of elements.

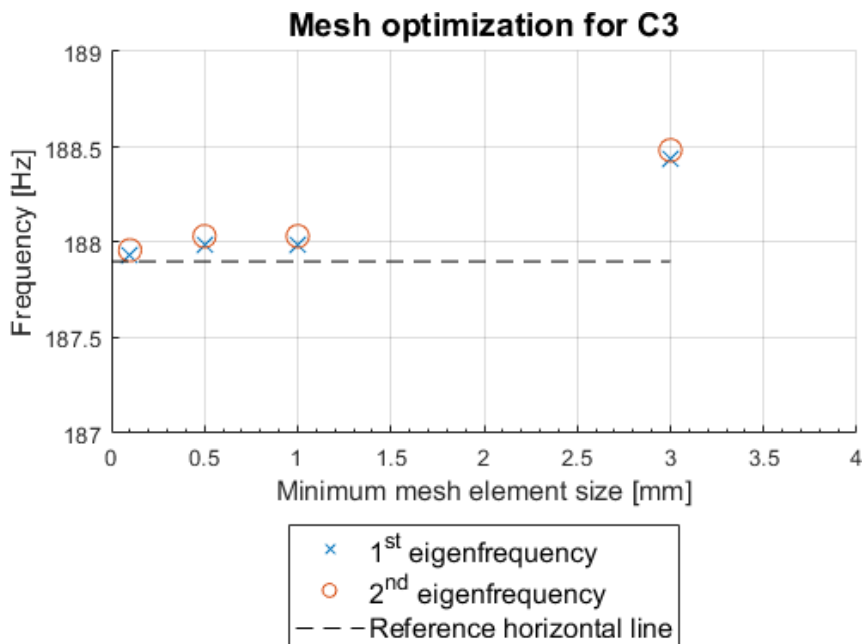


Figure 6.12: C3 - Mesh optimization

The first two modes of vibration ($f_1 = 187.94$ and $f_2 = 187.96$) with the lowest mesh element size are shown in Figure 6.13 and 6.14.

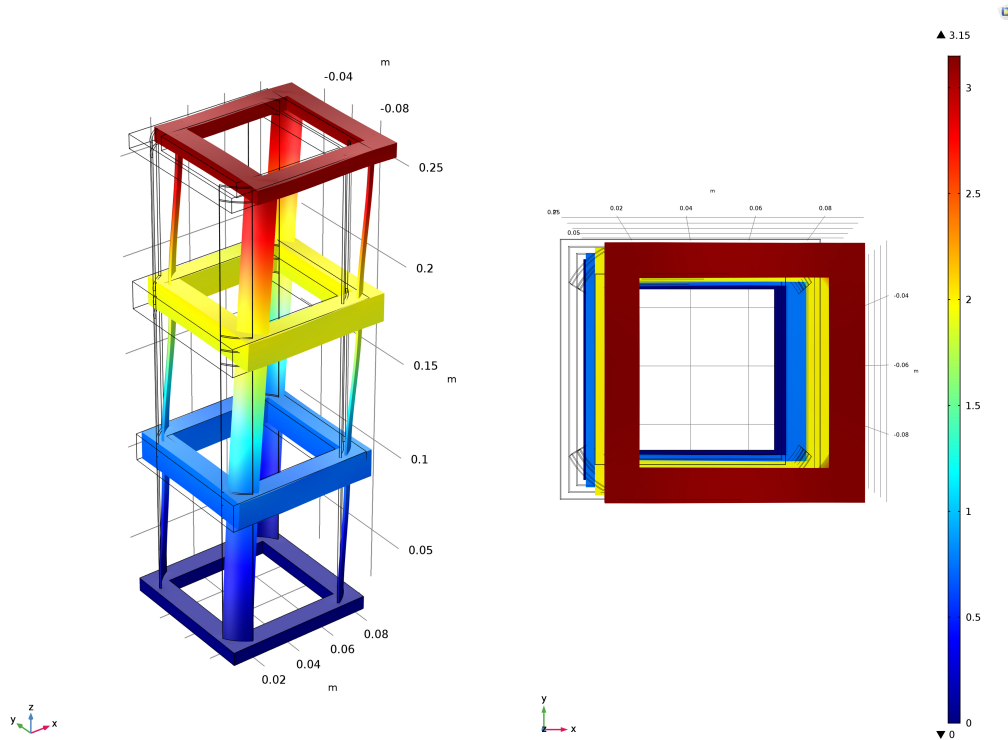


Figure 6.13: C3 - First mode - $f_1 = 187.94$

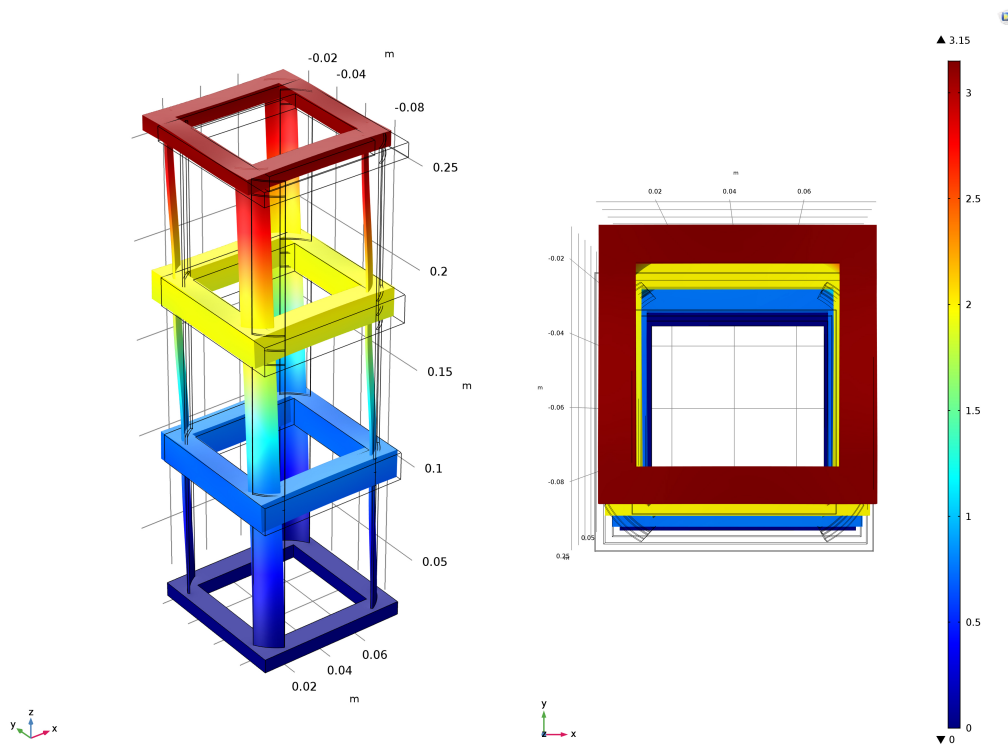


Figure 6.14: C3 - Second mode - $f_2 = 187.96$

As it is possible to see, the first two modes are characterized by bending in either X or Y (radial) directions with minor differences between the absolute values of the frequencies due to structural symmetry.

Eigenfrequencies of H3 design

The prototype H3 was analyzed as (1) a whole and separated as before in (2) counterclockwise and (3) clockwise part. The same analysis will be repeated also experimentally.

In this case, before importing the SolidWorks design in Comsol it was necessary to simplify it. Therefore, the parts made with the elastomeric material (Agilus) (Section 5.3.3) were disregarded, and a whole structure was designed, as it is possible to see in Figure 6.15 that shows only the clockwise part of the H3 prototype.



Figure 6.15: H3 - Simplified model for simulations

After this simplification, the file could be imported in Comsol and the simulations were set as described above for prototype C3, including the mesh optimization steps.

In Figure 6.16 and Figure 6.17 it is possible to see the simulation of the first two modes for the clockwise part of the structure; also in this case the modes are in couple (same radial symmetry of the structure) and show similar eigenfrequencies.

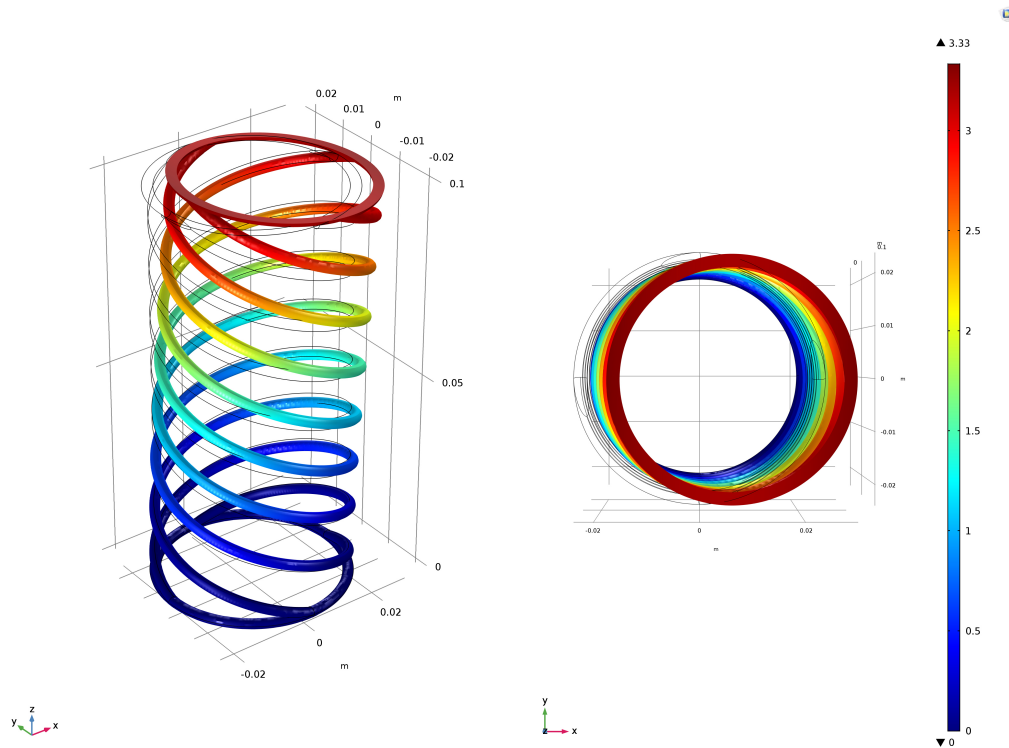


Figure 6.16: H3 Clockwise - First mode - $f_1 = 15.39$

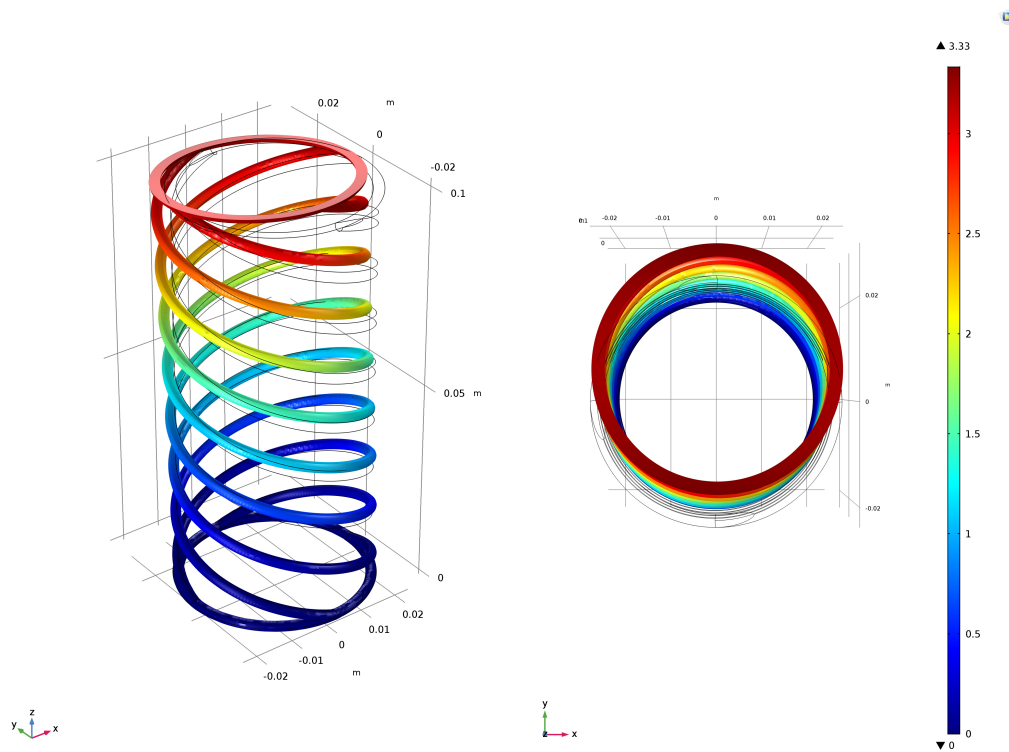


Figure 6.17: H3 Clockwise - Second mode - $f_2 = 15.39$

Also the counterclockwise structure was analysed, and the first two modes are show in Figure 6.18 and Figure 6.19.

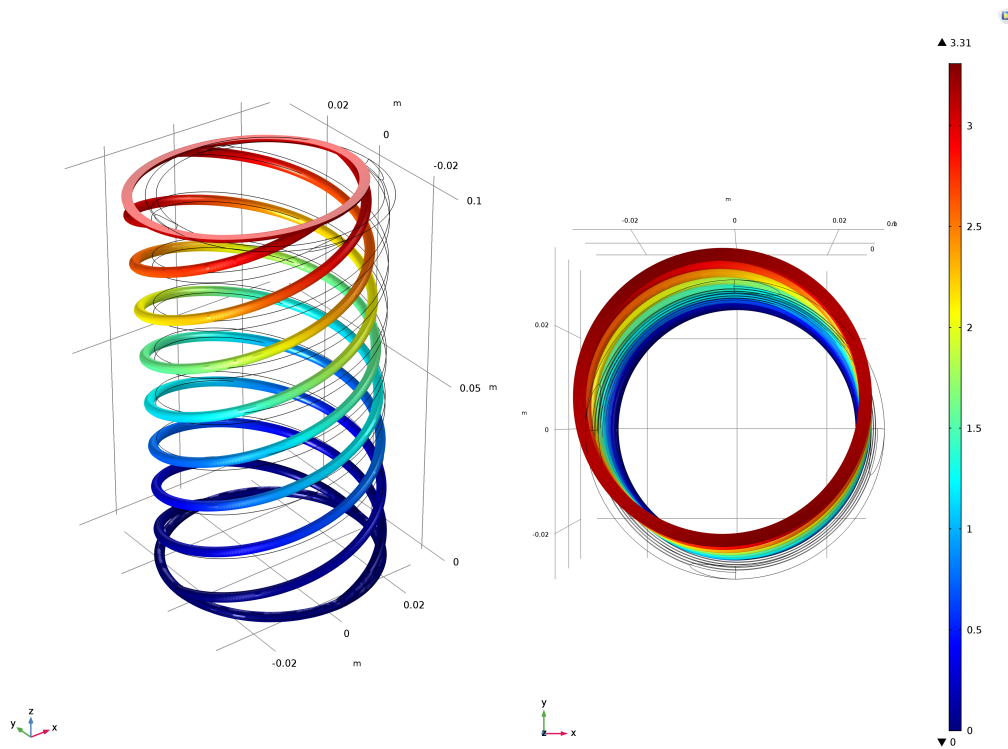


Figure 6.18: H3 Clockwise - First mode - $f_1 = 12.30$

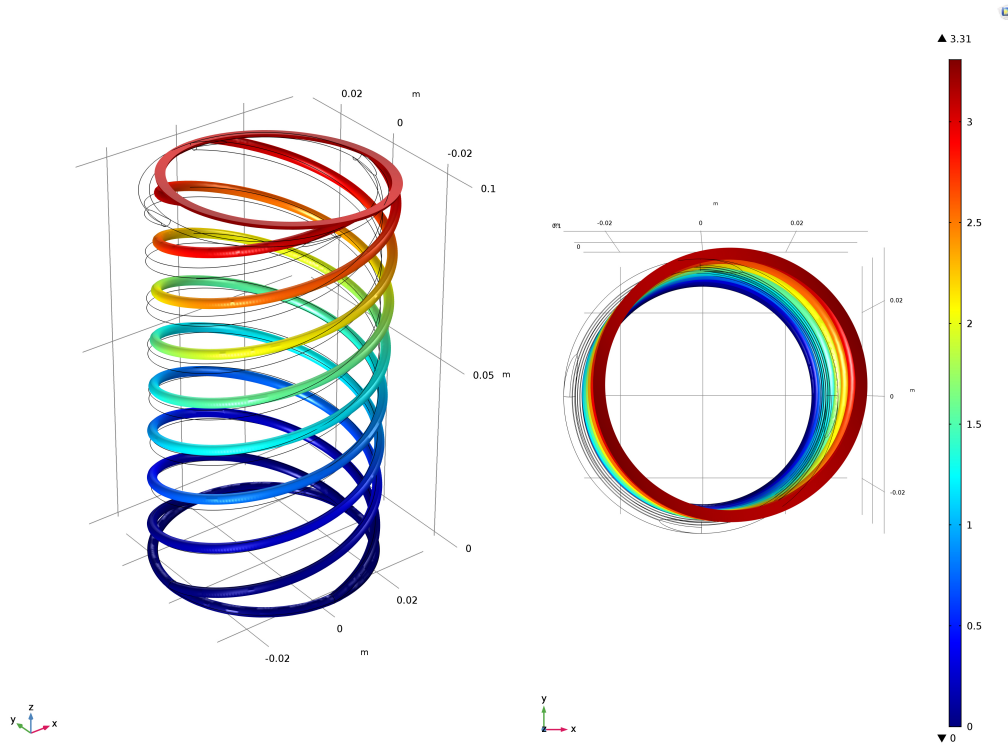


Figure 6.19: H3 Clockwise - Second mode - $f_2 = 12.30$

Finally, the simulation of the prototype H3 as a whole was performed; in this case, the target was to numerically prove the higher stiffness of the assembled prototype with respect to the two parts separated. In the following Figures 6.20 and 6.21, it is possible to see the first two modes.

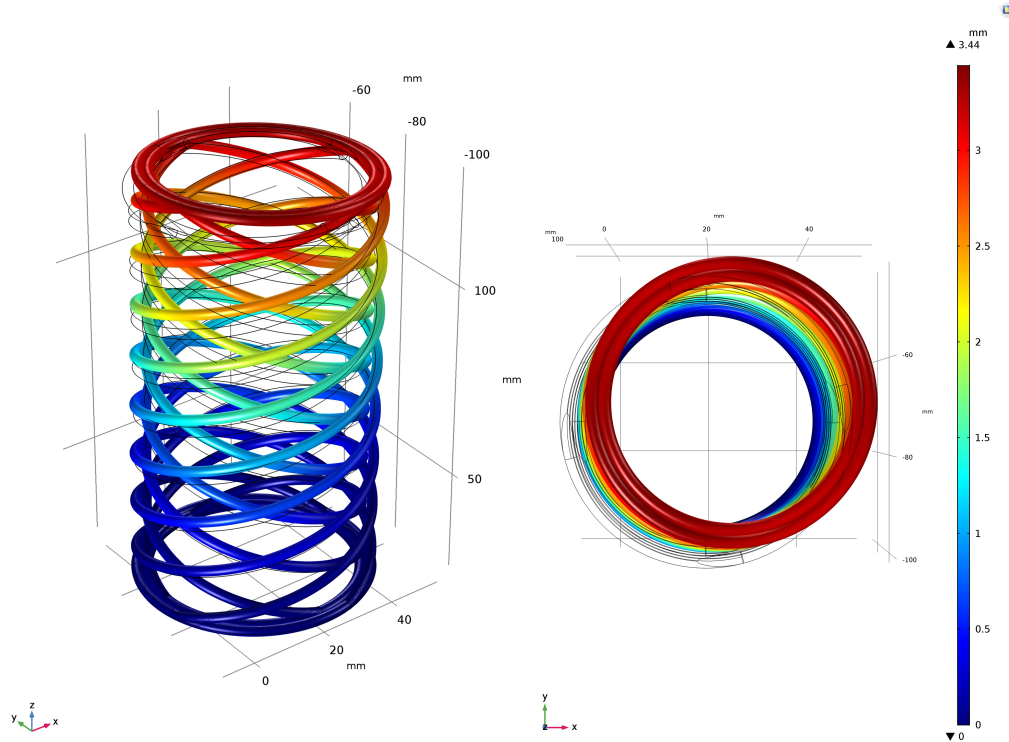


Figure 6.20: H3 - First mode - $f_1 = 16.03$

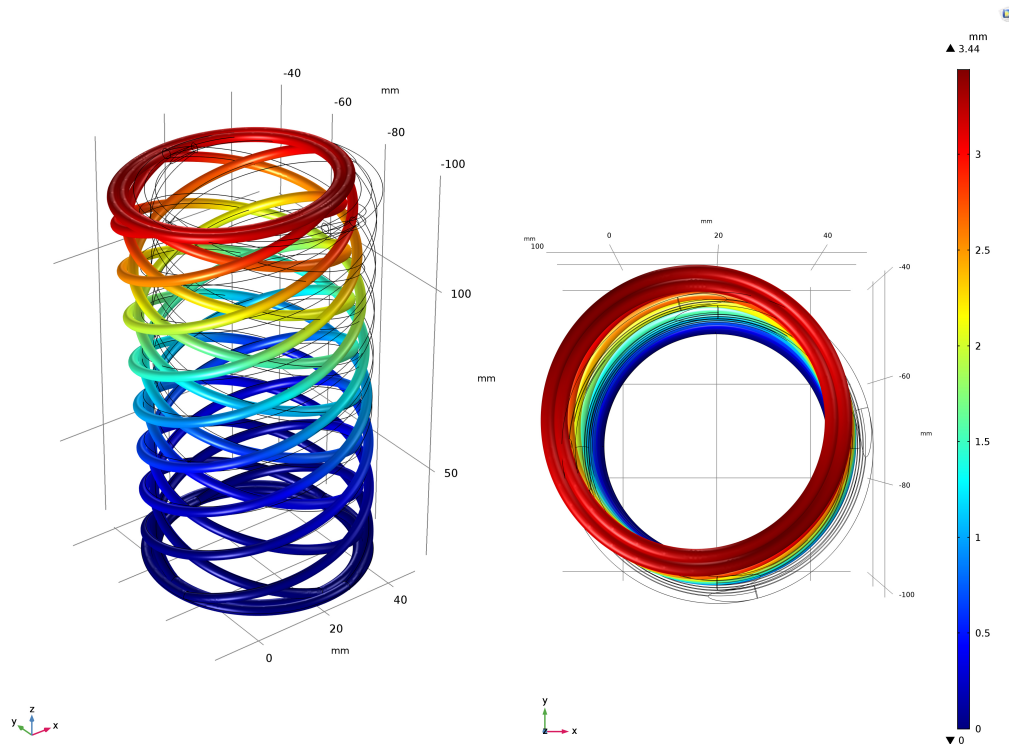


Figure 6.21: H3 - Second mode - $f_2 = 16.04$

In conclusion, the first two eigenfrequencies of all the structures were correctly simulated using Comsol. A summary is reported in Table 6.3, and it is clear that the C3 is the most stiff one, mainly thanks to the use of carbon steel. Nevertheless, the stiffness is expected to decrease in the real case: for example, in this simplified model the contact between steel and plastic has been assumed totally rigid, while in the prototype some glue has been used. It is quite interesting that the first two eigenfrequencies of the H3 assembled prototype are actually higher than the correspondent ones of its component.

Table 6.3: Summary of simulated eigenfrequencies

Structure	1 st	2 nd
C3	187.94	187.96
H3 Clockwise	15.39	15.39
H3 Counterclockwise	12.30	12.30
H3	16.03	16.04

The aim of this simulation was to obtain a frequency reference value to compare with the experimental testing; to be sure that the models gave acceptable results, a mesh optimization was performed on all models, with the same procedure introduced for prototype C3. The modes represented in this section are all referring to the structure bending; it is observed that the finer is the mesh, the more equal are the eigenfrequencies values of the first two modes (Figures 6.22, 6.23 and 6.24).

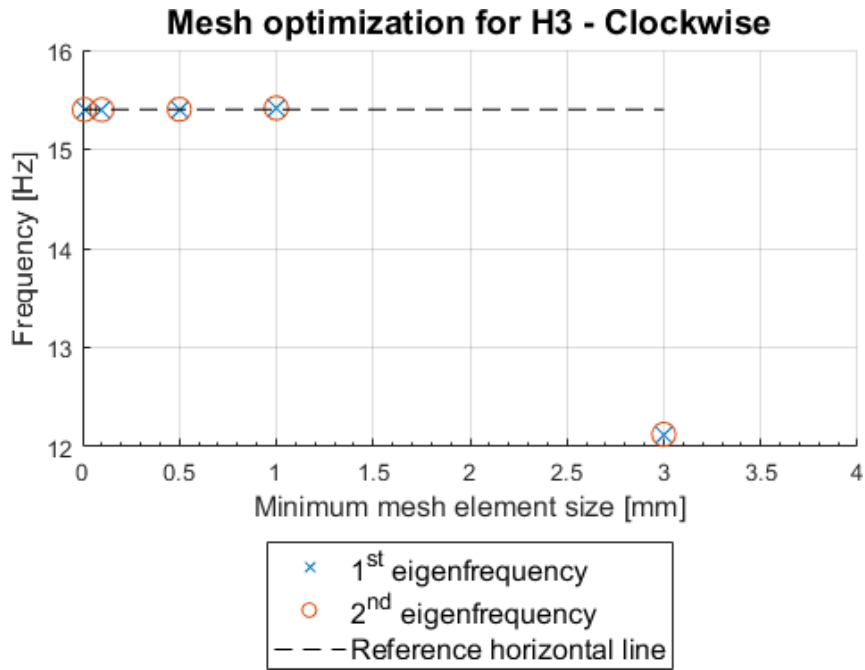


Figure 6.22: H3 Clockwise - Mesh optimization

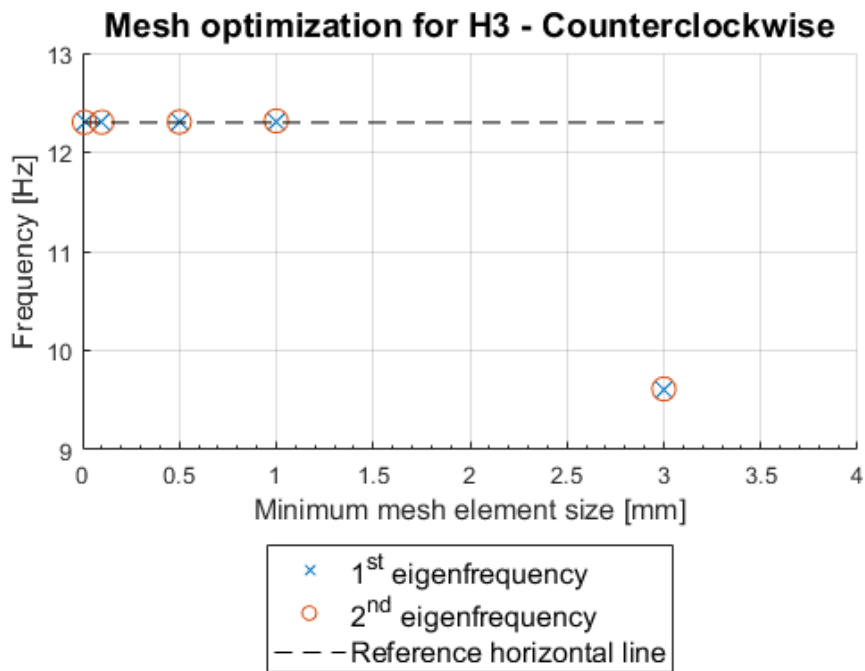


Figure 6.23: H3 Counterclockwise - Mesh optimization

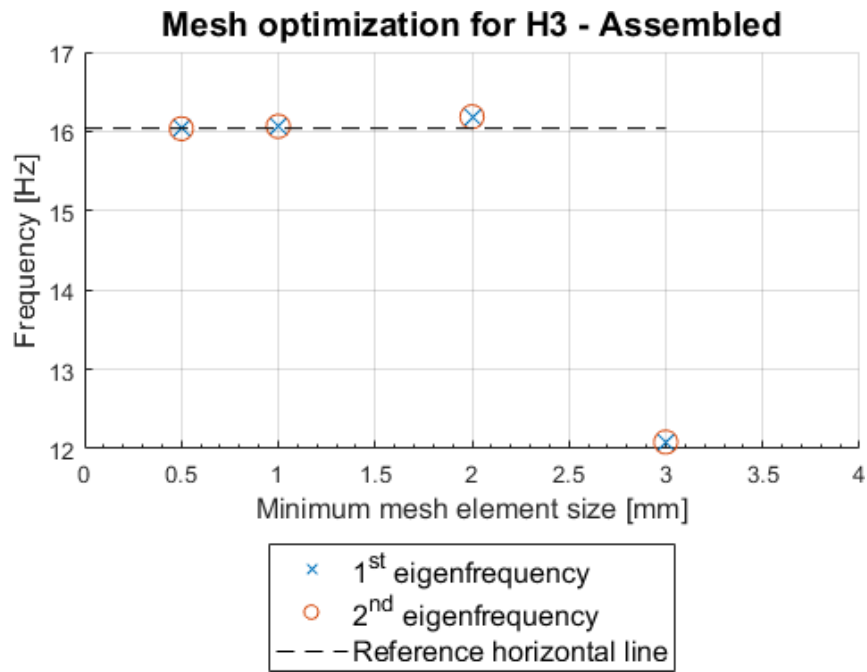


Figure 6.24: H3 - Mesh optimization

6.2.2 Experimental vibration test

The validation of the simulation introduced in the previous section has been carried out experimentally. The evaluation of the resonant frequency of the structure, it is enough to excite it with an impulse (hammer) and let it vibrate, recording the sequence with a high-speed camera (Sony RX200 II).

The setup of the test is shown in Figure 6.25, and since the camera is capturing frames at a very high speed, two lamps were added to the setup in order to give enough light during the shooting.



Figure 6.25: Vibration test setup

The prototype was fixed thanks to the bench vice (Figure 6.26); the camera was positioned behind the lamps in order to be right in front of the action. Since the antenna structure will be fixed to the CubeSat and will not be able to move, the vice was the best way to simulate it and allowed to assume infinite stiffness of the fixture. The vice part in contact with the ABS base has already a good grip on the base, therefore no other operations were needed from this side.

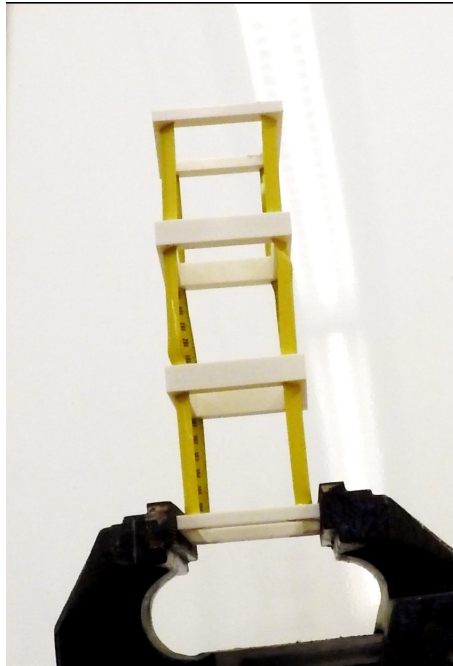


Figure 6.26: C3 - Constraint in vibration test setup

At this point, the camera started shooting and in the meantime a rubber-coated hammer was used to excite the structure, as seen in Figure 6.27.



Figure 6.27: C3 - Prototype hit by hammer

The high-speed camera captured 1000 frames per second (FPS); to analyze the data, the video was run and paused in correspondence of the beginning of the ex-

citement. At this point, the number of frames for a single cycle (an oscillation from left to right or viceversa) were counted and registered.

To find the natural frequency, it was only necessary to divide the frames captured by the camera (1000) by the number of counted frames.

$$\text{Natural frequency} = \frac{\text{Camera frames per second}}{\text{Number of frames per oscillation}} \quad (6.2)$$

The experiment was repeated five times, and the natural frequencies were calculated with the above described formula; the results are presented in Table 6.4. The last row represents the average natural frequency that was considered as means of comparison with the simulation model.

Table 6.4: C3 - Experimental results of vibration testing

	Number of frames per oscillation	Natural frequency [Hz]
First measurement	10	100.0
Second measurement	11	91.0
Third measurement	10	100.0
Fourth measurement	10	100.0
Fifth measurement	11	91.0
Average result		96.4 ± 4.4

In the H3 testing since the base is circular and the prototype is small and lightweight, it was sufficient to fix it with tape on the wooden bench.

Since this structure is less stiff than the C3 one, a GoPro Hero5 action camera with the settings on 240 frames per second was used to record the number of oscillations.

In fact, the oscillations were much slower, and it was easy to count the number of frames per oscillations.

In this case, the two helical structures were individually tested and eventually as a whole; this was done to understand if the results were compliant with the simulations on Comsol and to see how two similar structures would behave in the same test.

The first structure to be tested was the clockwise structure; as already anticipated, the encastre condition is made with some tape and is shown in Figure 6.28.



Figure 6.28: H3 Clockwise - Constraint in vibration test setup



Figure 6.29: H3 Clockwise - Prototype hit by hammer

As before, the video taken was analysed and the number of frames per oscillation was calculated.

The results are presented in Table 6.5, and the last row presents the average natural frequency for the structure.

Table 6.5: H3 Clockwise - Experimental results of vibration testing

	Number of frames per oscillation	Natural frequency [Hz]
First measurement	16	15.0
Second measurement	15	16.0
Third measurement	17	14.1
Fourth measurement	15	16.0
Fifth measurement	16	15.0
Average result		15.2 ± 0.7

The counterclockwise antenna was analysed, following the same scheme as for the clockwise one. In Figure 6.30, it is possible to see the tape fixtures simulating the encastre condition and the hammer laterally exciting the structure for the bending mode. Again, a GoPro Hero5 camera was used to record the high-speed video.



Figure 6.30: H3 Counterclockwise - Prototype hit by hammer

As before, in the video it is possible to see that the tape was enough to keep the structure perfectly adherent to the bench during the oscillations. In Table 6.6 the results are represented and the last row is showing the average frequency.

Table 6.6: H3 Counterclockwise - Experimental results of vibration testing

	Number of frames per oscillation	Natural frequency [Hz]
First measurement	20	12.0
Second measurement	18	13.3
Third measurement	19	12.6
Fourth measurement	20	12.0
Fifth measurement	20	12.0
Average result		12.4 ± 0.5

The results of both counterclockwise and clockwise structures are presented; as it is possible to notice, the clockwise one shows a slightly higher frequency with respect to the other. Anyways, the results lay in the same order of magnitude and it will be confronted with the Comsol simulations in the next section.

At this point following the same procedure, the test was performed on the assembled structures (H3 prototype) to understand if the increase in stiffness was significant.

The H3 prototype was therefore taped on the bench and excited with the same hammer as before; the two helices were fixed such that the connections were in the same angular position. The impact on the antenna is shown in Figure 6.31.



Figure 6.31: H3 - Prototype hit by hammer

In Table 6.7, it is possible to see the results reached by the prototype H3 as a whole.

Table 6.7: H3 - Experimental results of vibration testing

	Number of frames per oscillation	Natural frequency [Hz]
First measurement	10	24.0
Second measurement	10	24.0
Third measurement	9	26.7
Fourth measurement	11	21.8
Fifth measurement	10	24.0
Average result		24.1 ± 1.6

As a first comment, we can say that the H3 prototype has a higher stiffness with respect to the two single parts. This result was expected, and the discussion about it will continue in the following section with the comparison with the Comsol models.

6.2.3 Result comparison

In Table 6.8, the results from both the experimental testing and the simulations are presented.

Table 6.8: Simulated vs. experimental results of vibration testing

	Experimental frequency [Hz]	Simulated frequency [Hz]	Difference %
C3	96.4	187.94	+95
H3 - C	15.2	15.39	-1
H3 - CC	12.4	12.30	+1
H3 - Complete	24.1	16.03	-34

For prototypes H3 clockwise and counterclockwise the difference between the experimental and simulated results is within 1%; the assembled H3 has a slightly higher experimental eigenfrequency, but it is definitely acceptable considering the approximations made in the model in Comsol and the problems related to the frame reading in the experimental test. Finally, the prototype C3 is the most critical one: the discrepancy between the calculated and measured eigenfrequency is probably due to a higher metallic mass used in the Solidworks model and to the lack of the damping action of the glue experimentally used to fix the measuring tape into the plastic frame, which in the Comsol model has been assumed as rigid contact.

6.3 Final remarks

In this chapter, the programming of the shape memory prototype H3 has been carried out. After some preliminar calculation to determine the folding angle, a hot water bath was used to fold the structure into its undeployed state and subsequently a cold water bath was used to supercool it. The recovery ratio has been successfully calculated for both the single (clockwise and counterclockwise) structures and for the assembly, and in all cases is above 90 %, more than enough considering that a single deployment would be needed in reality. Secondly, mechanical vibration testing has been performed both numerically (Comsol) and experimentally (high-speed imaging): the results showed that a precise estimation of the first natural frequencies was possible through FEM for H3 Clockwise and Counterclockwise, but the error exceeded 30 % for the assembled H3 and was completely off (more than 90 %) for prototype C3, possibly related to simplified assumptions, material coupling and profound difference to reality (usage of glue, distortions etc.). In conclusion, it is possible to say that the manufactured structure using 3D printing can be successfully programmed with an almost perfect recovery ratio, and the vibration testing allowed to ascertain the respect of the requirements given by NASA for the CubeSat project. Finally, the validation of the numerical modeled was carried out experimentally, and fully succeeded only when a single material and structure was used.

Chapter 7

Conclusions and outlook

7.1 Conclusions

The scope of this thesis was the development of a passive mechanism for the deployment of a CubeSat antenna. The different antenna structures commercially (e.g. the one shown in Figure 7.1) and scientifically known for CubeSats have been analyzed, followed by a materials study in which the most relevant applications for both metals and polymers in space have been reviewed. Finally, different 3D printing technologies have been explained in details, with particular focus on polymeric feedstock such as the ones that were afterwards employed in the experimental work. A peculiar type of 3D printing is the so-called “4D printing”, in which 3D printed structures are programmed to change their shape upon reaction to an external stimulus. This is the chosen path for the experimental work, in order to spare the complexity and the cost of bringing to orbit an active actuation mechanism such as an electric motor.



Figure 7.1: HCT quadrifilar helical antenna [27]

Considering the harsh conditions that are present in outer space, a material study based on the data from CES EduPack has been carried out. In particular, following the directions from NASA, the main treats to space structures (and the related material characteristics) have been explored: ultraviolet radiation, vacuum, aggressive reactants such as atomic oxygen, thermal cycling with extreme temperature, impact with debris are only some of the few dangers identified in more than 50 years of space exploration, and their consequences are visible e.g. in Figure 7.2. The main scope of Chapter 3 is to provide a preliminar survey for selecting possible material candidates and classes for the final antenna structure. Ground experiments are proven to be still far away from simulating the real space conditions, and for this reason the best predictions on material durability come from results obtained on the ISS and presented in the MAPTIS database. In particular, metals are expected to perform quite well but manufacturing procedures are still missing for the realization of 4D-printed structures: for this reason, the material class of thermoplastic polymers was chosen, and in particular the ones available for the Polyjet process by Stratasys possibly with the use of coatings to obtain/enhance the necessary properties (conductivity, resistance to impacts etc.).

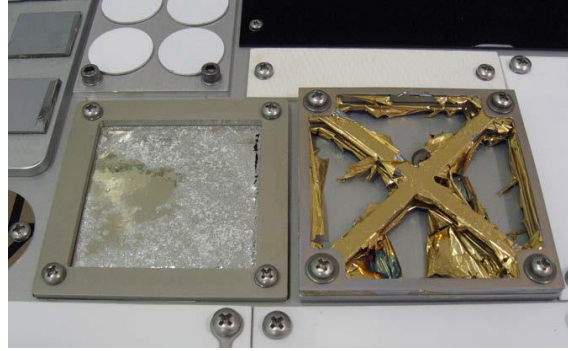


Figure 7.2: Coatings' failure related to thermal cycling and AO erosion [4]

In Chapter 4, an analysis of the available antenna models was presented in order to focus on the most promising design. The folding mechanisms are shown e.g. in Table 7.1. In particular, the critical properties for an antenna, such as radiation pattern, coverage, gain, polarization and directivity, were presented and explained. Moreover, the project requirements for the ETH CubeSat were there discussed, and this allows to restrict the choice to basically one single design type: the helix quadrifilar antenna.

Table 7.1: Folding mechanisms for different antennas [48]

	Hinge	Tape spring	Helical pantograph	Z-folded shells	Miura-Ori shells	Coilable conductors	Hinged ribs	Wrapped mesh
Dipole	X	X						
Helix			X	X	X	X		
CLS				X	X			
Horn				X	X			
Patch								
Reflector							X	X

Antenna design and details on manufacturing are discussed in Chapter 5: starting from a simple empirical equation, some sets of design parameters were numerically extrapolated for different receiving frequencies inside the UHF range using a Matlab script. Afterwards, several prototypes were manufactured thanks to a combination

of 3D printing and manual assembly. At the end, the final prototypes were called C3 (cube modular structure) and H3 (double spring structure, shown in Figure 7.3). The former was actually assembled and employs the measuring tape deployment mechanism while the latter was fully 3D printed using a Connex3 from Stratasys.



Figure 7.3: Rendering of prototype H3

The produced design was then programmed (only H3, shown in Figure 7.4) and tested for eigenfrequencies in Chapter 6: a FEM model was realized for all the prototypes, and the experimentally measured natural frequencies were in good agreement with the simulated ones, at least for the simplest designs.



Figure 7.4: H3 - Assembled prototype comparison

7.2 Outlook

Regarding future developments, both the prototypes analysed show big margins for improvement. First of all, the limitation in the 4D printing process did not allow the manufacturing of the prototype C3 as a whole. In fact, if a multimaterial printer capable of printing polymers and metals together would be implemented, this prototype could be manufactured without any need for a manual assembly, and the metallic parts could be covered in a plastic coating made of a shape memory polymer which could act as a damper and be actuated as the prototype H3.

For prototype H3 the situation is different: in fact, in order to have a working antenna, there is the need of making a filament pass inside the hollow branches. In this case, the conductor would be also fully protected from the space environment. This approach is currently studied in the research group by a telecommunications engineer, who will also validate the electromagnetic field radiated from the antenna. In the meantime, an optimization of the 3D printing process is needed to obtain hollow branches with an inner hole diameter of about 1 mm in diameter.

It is clear that the designed structure can fulfill all the requirements for this application, and the main limitation seems to be related to the materials palette available for the Connex3 printer. A switch towards Selective Laser Sintering or other powder bed fusion technology seems to be the most reasonable way to achieve the required set of properties, especially due to the availability of certified space materials such as the already-mentioned Windform [9]. Another alternative could be to apply powder coating with suitable polymers such as PEEK, that would provide enough durability to the external part of the antenna shielding it from the many dangers of outer space.

Bibliography

- [1] California Polytechnic State University and Stanford University's Space Systems Development Lab. CubeSat, 1999. URL <http://www.cubesat.org/>. Accessed on 31/03/2019.
- [2] W. A. Imbriale, S. S. Gao, and L. Boccia, editors. *Space Antenna Handbook*. John Wiley and Sons, 2012. ISBN 9781119993193. doi: 10.1002/9781119945147.
- [3] S. Tibbits. 4D Printing. *Architectural Design*, 84(1):116–121, 2014. ISSN 00038504. doi: 10.1002/ad.1710.
- [4] M. M. Finckenor and K. K. de Groh. *Space Environmental Effects*. 2010.
- [5] J. M. L. Torralba and A. R. Aranda. Low cost TVAC Chamber for aerospace tests. *Proceedings of 2018 Technologies Applied to Electronics Teaching, TAAE 2018*, pages 0–4, 2018. doi: 10.1109/TAAE.2018.8476133.
- [6] J. A. Dever. Low Earth Orbital Atomic and Ultraviolet Radiation Effects on Polymers. *NASA Technical Memorandum*, 103711(February 1991):16, 1991.
- [7] X. Wang, S. Kustov, and J. Van Humbeeck. A Short Review on the Microstructure, Transformation Behavior and Functional Properties of NiTi Shape Memory Alloys Fabricated by Selective Laser Melting. *Materials*, 2018. ISSN 19961944. doi: 10.3390/ma11091683.
- [8] Z. X. Khoo, Y. Liu, J. An, C. K. Chua, Y. F. Shen, and C. N. Kuo. A review of selective laser melted NiTi shape memory alloy, 2018. ISSN 19961944.
- [9] CRP Technology. Windform XT 2.0. Technical report, CRP Technology.

- [10] M. N. Sweeting. UoSAT-1: A review of orbital operations and results. *Journal of the Institution of Electronic and Radio Engineers*, 57(5):S184–S194, 1987. ISSN 0267-1689. doi: 10.1049/jiere.1987.0081.
- [11] J. Puig-Suari, C. Turner, and W. Ahlgren. Development of the standard CubeSat deployer and a CubeSat class\PicoSatellite. *2001 IEEE Aerospace Conference Proceedings (Cat. No.01TH8542)*, 1:347–353, 2001. ISSN 1095323X. doi: 10.1109/AERO.2001.931726.
- [12] Wikipedia. Dipole antenna, . URL <https://en.wikipedia.org/wiki/Dipole{-}antenna>. Accessed on 2018-09-17.
- [13] H. Heidt, J. Puig-Suari, A. S. Moore, S. Nakasuka, and R. J. Twiggs. CubeSat: A new Generation of Picosatellite for Education and Industry Low-Cost Space Experimentation. *AIAA/USU Conference on Small Satellites*, pages 1–19, 2000. doi: SSC00-V-5.
- [14] M. T. Islam, M. Cho, M. Samsuzzaman, and S. Kibria. Compact Antenna for Small Satellite Applications. *IEEE Antennas and Propagation Magazine*, 57(2):30–36, 2015.
- [15] A. Nascetti, E. Pittella, P. Teofilatto, and S. Pisa. High-gain S-band patch antenna system for earth-observation CubeSat satellites. *IEEE Antennas and Wireless Propagation Letters*, 14:434–437, 2015. ISSN 15361225. doi: 10.1109/LAWP.2014.2366791.
- [16] Wikipedia. Radio Spectrum, . URL <https://en.wikipedia.org/wiki/Radio{-}spectrum>. Accessed on 2018-09-17.
- [17] G. Olson, S. Pellegrino, J. Banik, and J. Costantine. UHF Deployable helical antennas for cubesats. In *IEEE Transactions on Antennas and Propagation*, volume 64, pages 1–14, Reston, Virginia, apr 2016. American Institute of Aeronautics and Astronautics. ISBN 978-1-62410-223-3.

- [18] M. Sakovsky, S. Pellegrino, and H.M.Y.C. Mallikarachchi. Folding and Deployment of Closed Cross-Section Dual-Matrix Composite Booms. *3rd AIAA Spacecraft Structures Conference*, pages 1–18, 2016. doi: 10.2514/6.2016-0970.
- [19] G. Olson, S. Pellegrino, and J. Costantine. Structural Architectures for a Deployable Wideband UHF Antenna. *American Institute of Aeronautics and Astronautics*, 50(April):1–10, 2012. ISSN 02734508. doi: 10.2514/6.2013-1671.
- [20] M. W. Thomson. ASTROMESH™ Deployable reflectors for KU- and KA-Band and commercial satellites. *American Institute of Aeronautics and Astronautics*, 2002.
- [21] ESA. SMAP (Soil Moisture Active/Passive) Mission. URL <https://earth.esa.int/web/eoportal/satellite-missions/s/smap{#}vWc5A12ceHerb>. Accessed on 2018-09-18.
- [22] J. Block, A. Bäger, J. Behrens, T. Delovski, L. C. Hauer, M. Schütze, R. Schütze, and T. Spröwitz. A self-deploying and self-stabilizing helical antenna for small satellites. *Acta Astronautica*, 86:88–94, 2013. ISSN 00945765. doi: 10.1016/j.actaastro.2011.10.012.
- [23] D. Ochoa, K. Hummer, and M. Ciffone. Deployable Helical Antenna for Nano-Satellites. *28th Annual AIAA/USU Conference on Small Satellites*, pages 1–7, 2014.
- [24] W Su, S A Nauroze, B Ryan, and M M Tentzeris. Novel 3D printed liquid-metal-alloy microfluidics-based zigzag and helical antennas for origami reconfigurable antenna 'trees'. *2017 IEEE MTT-S International Microwave Symposium, IMS 2017*, pages 1579–1582, 2017. ISSN 0149645X. doi: 10.1109/MWSYM.2017.8058933.
- [25] S. Foletti. Mechanical behavior of materials B. *Politecnico di Milano, Lecture Notes, A.Y. 2017/2018*.
- [26] W. J. Bumbler and F. E. Wang. A Summary of Recent Research on the Nitinol*

- Alloys and Their Potential Application in Ocean Engineering. *Ocean Engng*, 1: 105–120, 1968. ISSN 00298018. doi: 10.1016/0029-8018(68)90019-X.
- [27] G. O’Neill. Deployable Small Satellite Antenna: Quadrifilar Helical Antenna. *2016 International Workshop on Antenna Technology, iWAT 2016*, pages 116–118, 2016. doi: 10.1109/IWAT.2016.7434818.
- [28] M. K. Pitchan, S. Bhowmik, M. Balachandran, and M. Abraham. Process optimization of functionalized MWCNT/polyetherimide nanocomposites for aerospace application. *Materials and Design*, 127(April):193–203, 2017. ISSN 18734197. doi: 10.1016/j.matdes.2017.04.081.
- [29] M. Behl and A. Lendlein. Shape-memory polymers. *Materials Today*, 10(4): 20–28, 2007. ISSN 13697021. doi: 10.1016/S1369-7021(07)70047-0.
- [30] A. Lendlein and S. Kelch. Shape-memory polymers. *Angewandte Chemie International Edition*, 41(12):2034–2057, 2002. ISSN 13697021. doi: 10.1016/S1369-7021(07)70047-0.
- [31] P. T. Mather, X. Luo, and I. A. Rousseau. Shape Memory Polymer Research. *Annual Review of Materials Research*, 39(1):445–471, 2009. ISSN 1531-7331. doi: 10.1146/annurev-matsci-082908-145419.
- [32] R. M. Schueler. Self-deploying trusses containing shape-memory polymers. *NASA Tech Briefs*, pages 20–21, 2008.
- [33] American Society for Testing and Materials. ISO/ASTM 52900:2015 - Additive Manufacturing, 2015.
- [34] N. A. Sukindar, M. K. A. Ariffin, B. T. Hang Tuah Baharudin, C. N. A. Jaafar, and M. I. S. Ismail. Analyzing the effect of nozzle diameter in fused deposition modeling for extruding polylactic acid using open source 3D printing. *Jurnal Teknologi*, 2016. ISSN 01279696. doi: 10.11113/jt.v78.6265.
- [35] Prusa. Overhangs. URL <https://www.prusaprinters.org/how-to-create-custom-overhang-supports-in-meshmixer/>. Accessed on 2019-10-03.

- [36] Stratasys. uPrint SE Plus, . URL <https://www.stratasys.com/it/stampanti-3d/idea-series/uprint-se-plus>. Accessed on 2018-10-10.
- [37] Stratasys. Connex3 Object500, . URL <https://www.stratasys.com/3d-printers/objet-350-500-connex3>. Accessed on 2018-10-10.
- [38] G. F. Hu, A. R. Damanpack, M. Bodaghi, and W. H. Liao. Increasing dimension of structures by 4D printing shape memory polymers via fused deposition modeling. *Smart Materials and Structures*, 26(12), 2017. ISSN 1361665X. doi: 10.1088/1361-665X/aa95ec.
- [39] International Organization for Standardization. E595 - 15 Standard Test Method for Total Mass Loss and Collected Volatile Condensable Materials from Outgassing in a Vacuum Environment (E595-07), 2014.
- [40] International Organization for Standardization. ECSS-Q-70-71A2004 Space product assurance- Data for selection of space materials and processes, 2004.
- [41] E. Murad. The shuttle glow phenomenon. *Annual Review of Physical Chemistry*, 2002. ISSN 0066-426X. doi: 10.1146/annurev.physchem.49.1.73.
- [42] American Society for Testing and Materials. ASTM E2089 - 15 Standard Practices for Ground Laboratory Atomic Oxygen Interaction Evaluation of Materials for Space Application, 2015.
- [43] B. A. Banks, J. A. Backus, M. V. Manno, D. L. Waters, K. C. Cameron, and K. K. de Groh. Atomic Oxygen Erosion Yield Predictive Tool for Spacecraft Polymers in Low Earth Orbit. *11th International Symposium on Materials in the Space Environment*, 2009. ISSN 0022-4650. doi: 10.2514/1.48849.
- [44] International Organization for Standardization. ECSS-Q-ST-70-04C Space Product Assurance - Thermal testing for the evaluation of space materials, processes, mechanical parts and assemblies., 1996.
- [45] NASA. MAPTIS - Materials And Processes Technical Information System. URL <https://maptis.nasa.gov/>. Accessed on 31/03/2019.

- [46] J. D. Kraus and R. J. Marhefka. *Antennas For All Applications*. McGraw - Hill, 2002. ISSN 0196-6553. doi: 10.1002/ejoc.201200111.
- [47] N. Blaunstein and C. G. Christodoulou. *Radio Propagation and Adaptive Antennas for Wireless Communication Networks: Terrestrial, Atmospheric, and Ionospheric: Second Edition*. 2014. ISBN 9781118816707. doi: 10.1002/9781118816707.
- [48] M. Sakovsky, S. Pellegrino, and J. Costantine. Rapid Design of Deployable Antennas for CubeSats. *IEEE Antennas & Propagation Magazine*, (april):50–58, 2017. ISSN 10459243. doi: 10.1109/MAP.2017.2655531.
- [49] T. T. Le, H. H. Tran, and T. K. Nguyen. Compact broadband circularly polarized slot-patch antenna array. *International Journal of RF and Microwave Computer-Aided Engineering*, (April):1–7, 2019. ISSN 1099047X. doi: 10.1002/mmce.21468. URL <https://doi.org/10.1002/mmce.21468>.
- [50] C. E. Balanis. *Antenna Theory: Analysis and Design*, 3rd Edition - Constantine A. Balanis, 2005. ISSN 00135127.
- [51] F. Angeletti, P. Gasbarri, M. Sabatini, and G. Palmerini. Learning-based Control Scheme to Deploy Modular Space Structures. 2018.
- [52] K. A. Steffen and S. Pellegrino. Deployment dynamics of tape springs. *The Royal Society*, pages 1003–1048, 1998.
- [53] F. Dewalque, J. P. Collette, and O. Brüls. Mechanical behaviour of tape springs used in the deployment of reflectors around a solar panel. *Acta Astronautica*, 123:271–282, 2016. ISSN 00945765. doi: 10.1016/j.actaastro.2016.03.029.

Acknowledgements

First of all, I would like to thank Professor Stefano Mariani, who enthusiastically accepted to be my internal supervisor for this master thesis. He has been very supportive for all the time that was requested to develop this work, always available for advice and guidance.

Secondly, I would like to express my gratitude to the head of the Engineering Design and Computing Laboratory of ETH Zurich, Professor Kristina Shea, for having hosted me and given the opportunity of exploring 4D printing applied to space structures.

Last but not least, I would like to mention all the people that I met at EDAC: everybody was very well prepared and always ready to help in all situations. The students with whom I shared this research experience helped me during the worst days, and there was always time for a coffee and an encouraging word.

It was an experience I will never forget.